DUBLIN CITY UNIVERSITY

SCHOOL OF PHYSICIAL SCIENCES

Spectroscopic characterisation of novel materials for semiconductor device applications

Ian Reid B.Eng

Doctor of Philosophy

May 2007

Supervised by Prof. G. Hughes

Dedication and Acknowledgements

First and foremost, I would like to thank my supervisor Greg Hughes for introducing me to physics. His enthusiasm for physics is unmatched and he is an inspiration for us all. I would also like to thank Kevin Smith and Elizabeth Shannon for the scholarship to Boston University; it was a great experience and opportunity for me.

From DCU I would like to thank Oisin McDonald for putting me in hospital (my knee will never be the same again!). Also Stephen, Clare, Rob and Barry and the rest of the surface science group who were there along the way. Yufeng Zhang and Alex Demasi for the work carried out together at the beamline and also to the rest of the novel materials group in BU for making me feel at home. Also my friends from outside of college (a.k.a. "the lads"). I would like to thank my girlfriend Madeleine for her love, understanding and support throughout the last few years.

Finally, I would also like to thank my parents for their support (financial and otherwise) through out all my years of education, I wont forget the many hours my mother sat beside me making sure my homework was done… thanks.

I would like to acknowledge the support of Science Foundation Ireland under an SFI Investigator Grant (grant title "PlasMAC") and also financial support from the Higher Education Authority under the NDP.

"Something's are way too scientific, but this isn't"

Declaration

I hereby certify that this material, which I now submit for assessment on the programme of study leading to the award of doctor of Philosophy is entirely my own work and has not been taken from the work of others save and to the extent that such work has been cited and acknowledged within the text of my work.

Signed: Jan Reid (Candidate)

ID No.: 99035766

Date: 27/07/2007

Abstract

The thesis uses surface science techniques to characterise the chemical composition and electronic properties of a range of carbon containing materials which have application in advanced semiconductor fabrication. The initial focus was on investigating the properties of carbon-doped oxide (CDO) which is a low dielectric constant material and a leading candidate to replace silicon dioxide (SiO_2) as an interlayer dielectric (ILD) in microprocessor fabrication. The work then progresses to determine the optimum experimental conditions required to etch thin films of this material, while retaining the chemical composition, in an industrial fluorocarbon-based plasma etching (FBPE) system. This study was preceded by an investigation of how the chemical composition of a thin fluorocarbon films which forms on a surface in the plasma etcher depends on the $C_4F_8/Ar/O_2$ gas feed ratios and the power levels used in the processing. These studies were benchmarked by undertaking baseline studies of the plasma processing of conventional SiO_2 inter layer dielectric material. The chemical composition of the fluorocarbon films and the CDO layers were analysed using X-ray photoelectron spectroscopy (XPS). Synchrotron radiation based x-ray absorption spectroscopy (XAS) and x-ray emission spectroscopy (XES) as well as resonant soft X-ray emission spectroscopy (RSXE) have been used to provide information on the valence band and conduction band state of both the CDO layers and the fluorocarbon films. The final part of the thesis consists of the measurement of the electronic structure of thin films of the organic semiconductor tetraphenylporphyrin (TPP) and metal TPP. The carbon and nitrogen partial density of states for both the valence and conduction band electronic structure has been determined, as well as core level spectra. Good agreement was found between the experimental measurements of the valence and conduction bands, and the results of density functional theory calculations.

Publications Resulting From This Work:

- **Electronic structure characterisation of Ultra Low-*k* (ULK) Carbon Doped Oxide (CDO) using soft X-ray emission spectroscopy.**

I. Reid, Y. Zhang, A. DeMasi, G. Hughes and K. E. Smith. Thin Sol. Films (2007) (*accepted*)

- **Investigation of varying C_4F_8/O_2 gas ratios on the plasma etching of carbon doped ultra low-*k* dielectric layers.**

I. Reid and G. Hughes. Semi. Sci. Tech. 22 (2007) 636-640

- **Suppression of carbon depletion from carbon-doped low-*k* dielectric layers during fluorocarbon based plasma etching**

I. Reid, V. Krastev, G. Hughes Micro. Eng. 83, 11-12, (2006) 2458-2461

- **Influence of plasma parameters on the chemical composition of steady-state fluorocarbon films deposited on carbon-doped low-*k* dielectric layers during etching**

I. Reid and G. Hughes. Semi. Sci. Tech.. 21 (2006) 1354–1357

- **Influence of $C_4F_8/Ar/O_2$ plasma etching on SiO_2 surface chemistry**

V. Krastev, I. Reid, C. Galassi, G. Hughes, E. McGlynn. J. Mat. Sci.: Mat. Elec. 16 (2005) 541– 547

Table of Contents

Table of Figures

Chapter 1: Background Introduction

1.1 Introduction

This chapter is a brief introduction to the main topics covered in the thesis. The role of low-*k* dielectric materials in device fabrication is introduced and the importance of fluorocarbon etching is outlined. The organic semiconductor materials which will be characterized in the final part of the thesis are also briefly described.

The thesis begins with an investigation of the chemical composition of a low dielectric constant material which is a potential candidate for integration into semiconductor device fabrication. This material which is a variation of the currently used SiO_2 is called carbon doped oxide (CDO). It has the potential to reduce the dielectric constant of the inter-dielectric layer used as electrical insulation between the metal lines which interconnect all the transistors on a microprocessor.

All the materials investigated in the project were processed in prototype commercial etchers which are designed to give a much higher level of control over the plasma etch parameters than currently available in conventional plasma systems. Following processing the samples were transferred in air to the surface characterisation system and hence were exposed to atmospheric conditions. As one of the aims of the project was to develop an understanding of the actual surface composition of the materials as they would be handled in device processing, the exposure to ambient conditions was an integral part of the experiment.

1.2 Dielectric materials

Shown in figure 1.1 is a schematic drawing of a microprocessor with a hierarchical wiring approach for multilevel interconnects. Advanced microprocessors may consist of 10 or more levels of metallisation. Dielectric layers used in device fabrication can be divided into three groups. The first group play an active role as dielectric barrier films in device operation mainly for storing charge. These dielectrics have a high dielectric constant. The second group

are films that are needed during device fabrication as etch stop layers or for the process of chemical mechanical planarisation (CMP). Most of theses layers do not have any specific role in device functioning after the completion of this processing step. The third group of dielectric films used in microelectronic devices consist of insulating layers. These are used to isolate two adjacent transistors which is carried out by trench isolation and when isolation of the device from the ambient in needed. They are also used for isolation between metal lines in the same level and for the isolation between two metal levels. This last type of dielectric material is studied in the thesis.

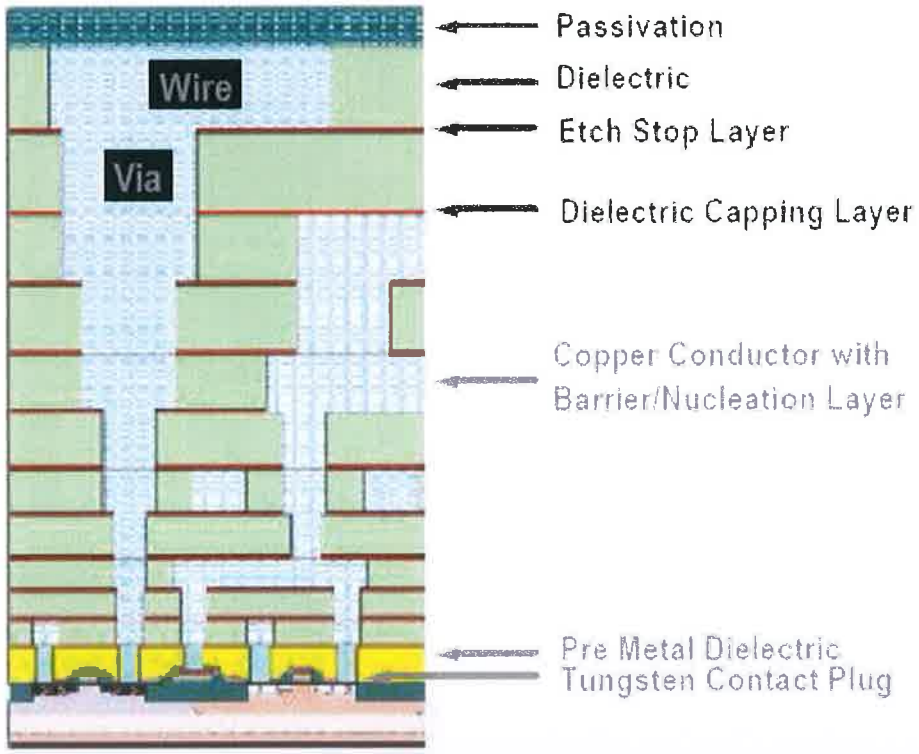

Figure 1.1: Schematic drawing of a microprocessor with a hierarchical wiring approach for multilevel interconnects [1,2]

In ultra–large-scale-integration (ULSI) technology, a major performance limiting factor is the resistance-capacitance (RC) delay associated with the parasitic capacitance of the insulating

interlayer dielectric (ILD) and with the resistance of the metal interconnects [3]. Integration of ultra low-dielectric constant materials can be applied as an effective way to address this challenge. Prototype SiO_2 based ultra low-dielectric constant materials which have a high porosity have the advantage of compatibility with conventional Si processing technology [4]. The ILD layer must also be integrated into existing chip production lines, which means that potential candidates should possess the same basic properties as silicon dioxide films, which include good adhesion to under lying layers and a low degree of moisture absorption. High thermal stability is also required so that the films do not breakdown during high- temperature processing steps.

Feature size refers to the width of the channel of the transistor. In the semiconductor industry there are milestones in terms of the gate length and these targets are referred to as generation nodes. Figure 1.2 shows a graph of the decrease in feature size and the corresponding chip cycle time. The decrease in feature size results in a large increase in the RC delay time, which for devices smaller than 0.25μm controls the overall on-chip cycle time [5]. Therefore in order to increase the device speed, the lower resistivity Cu is replacing Al, and the current low-*k* materials (with $\kappa = 3$) will be replaced by ultra low-*k* materials (ULK) (with $\kappa < 2.3$).

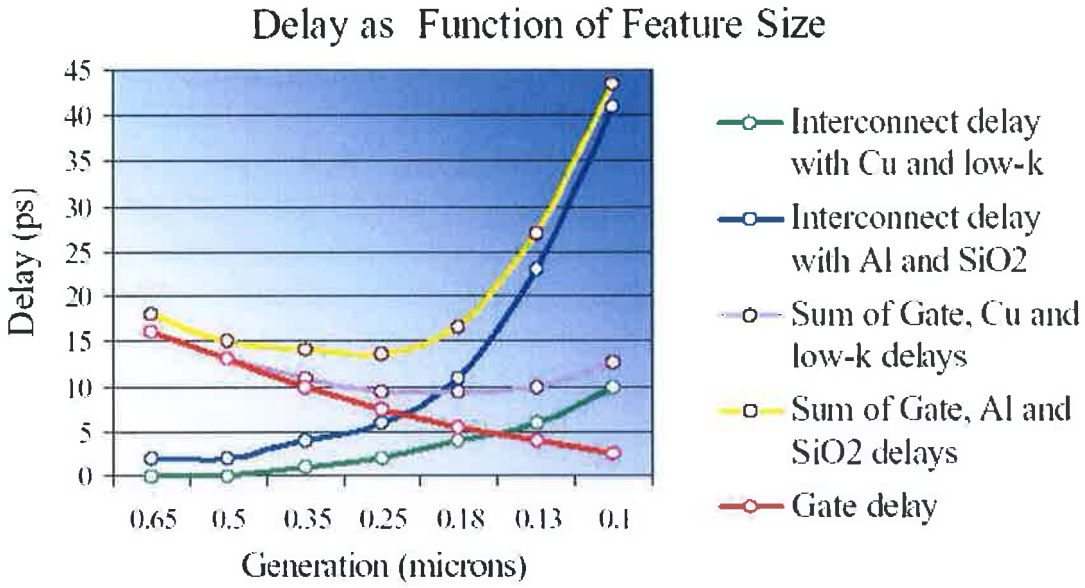

Figure 1.2: RC delays with generation node [6]

A simple model of the interconnects equivalent circuit is given in figure 1.3, where P is the metal pitch, W is the line width, S the line spacing, T is the metal thickness and the dielectric thickness above and below the interconnect is equal.

The RC delay is given by [2]:

$$RC = 2\rho\,\kappa\,\varepsilon_0\,(4L^2/P^2 + L^2/T^2) \qquad (1.1)$$

Where ρ is the metal resistivity, κ is the relative dielectric constant of the ILD, ε_0 is the permittivity of a vacuum, L is the total length of the metal line, [2]

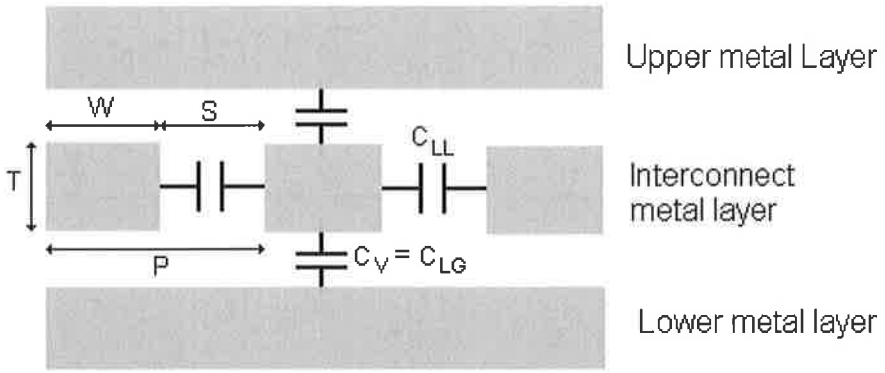

Figure 1.3: Model of the RC delay [2]

An added reason for the need of a low-*k* dielectric material is due to the power dissipation which is given by:

$$P = (1/2) f_d \, CV^2 f \qquad (1.2)$$

Where C is the total on capacitance, V is the supply power, f is the operational frequency, and f_d the fraction of gates that switch during a clock period. Reducing κ will in turn reduce C, thus leading to a decrease in power dissipation which will make circuits faster and more portable [2].

1.3 Plasma based etching

In this section the nature and properties of plasmas that are technologically interesting are outlined.

It is often stated that there exist three states of matter; solid liquid and gas. The existence of these states is an obvious fact of everyday life. Plasma, the fourth state of matter, is less accessible, since it does not occur in the terrestrial environment, except briefly in phenomena such as lightning. Nevertheless, plasma is important in the universe: most of the

matter which exists is in the plasma state. For example, the sun essentially consists entirely of plasma, and the interplanetary space including the earth's outer atmosphere is filled with a tenuous plasma. Thus the study of plasma is scientifically important. However, this thesis is concerned with technological applications of plasma, and these are created in laboratories, rather than by natural events. The study of laboratory plasmas began in earnest with work by Faraday, and has been more or less continuous ever since. It is only relatively recently that the promise of plasma technology in the context of the modern industries has become clear.

Plasma-based surface processing is a relatively new technique in manufacturing very large scale integrated circuits [3]. Introduced in the 1970's mainly for stripping resists, it has over the last 15 years rapidly developed in the microelectronic industry and particularly found useful in the fabrication of silicon integrated circuits. Plasma based technologies are increasingly been utilized in many other material processing industries. Nowadays, many of the deposition and etching process steps involved in several technologies of integrated circuit fabrication are based on the chemistry and physics of plasmas instead of chemical processes as was the case 20 years ago [4]. Among the several plasma etching methods, radio frequency (RF) plasma-based etching is one of the most important processing technologies used in the manufacture of highly integrated electronic circuits.

In manufacturing microprocessors, an important step is etching, in which material is removed from predefined areas on the surface of the silicon wafer. Typically, one wants to form deep trenches in the surface of the wafer, such as the features shown in figure 1.1, and the width of these trenches corresponds to the feature size of the microprocessor, which is now 100 nm or less. The manufacture of a typical modern microprocessor entails approximately three hundred process steps involving twenty structural layers. The economic and technical advantage of plasma processing are such that 37% of process steps are now plasma based, and this is expected to rise to more than 50% as the next generation of the

technology is introduced [1]. A further 24% of process steps use plasmas indirectly, as ion sources or light sources.

Plasma processing in the semiconductor device manufacturing industry presents some of the most challenging technical problems found in any industry, while at the same time offering the largest economic rewards. For example, a raw silicon wafer costs only a few tens of euros to produce, whereas a finished array of microprocessors on the same wafer may be worth tens to hundreds of thousands of euros. This added value warrants large investment to pursue process improvements. The international semiconductor roadmap [1] emphasizes the need to prepare for processing of larger area wafers, for the introduction of new materials and corresponding processes, for tighter control of process parameters, and for control of contaminates. The central thrust of the first part of this thesis is to address issues relating to the plasma-based etching of low-*k* dielectric materials.

1.4 Organic Semiconductors

Organic semiconductors have been the subject of intense study due to their potential scientific importance. At present the focus of the research into 'organic molecular electronics' falls roughly into two categories. The first category is research that is being carried out on a macroscopic scale and involves the fabrication and optimisation of simple molecular based devices. Organic Field Effect Transistors [7] (OFETs) have thus far been fabricated with room temperature mobilities in the range of 1.5cm^2/Vs indicating the potential that organic semiconductors could have for the future production of low cost electronic devices. Similarly, the optimisation of Organic Light Emitting Diodes [8,9,10,11] (OLEDs) through the use of doping has allowed for greater control of the luminescence of these devices along with improved device stability. The second category of research involves the investigation of the properties of thin molecular films on a microscopic and more fundamental level. Studies of

devices have shown for example, that grain boundaries and defects can have a large role to play in determining the electronic properties of these devices [12]. For device optimisation, it is imperative that a greater understanding of the properties of molecular films is obtained. In order to achieve this, studies at a more fundamental level are required into the chemical and electronic structure of thin organic films.

One group of molecules that has attracted attention in recent studies is transition metal tetraphenylporphyrins (MTPP). They have been investigated for their use in structures such as chemical sensors [13], organic semiconductors [14], and opto-electronic device fabrication [15]. Accurate determination of the electronic structure of thin film organic semiconductors is a prerequisite to developing a comprehensive understanding of these electronic materials. The structural and optical properties of TPP have been extensively studied using visible light absorption spectroscopy, Fourier transform infrared spectroscopy and scanning tunneling microscopy [16,17,18,19]. Chemical composition XPS studies on TPP and CuTPP have been carried out by *Niwa et al* [25]. However, to date, detailed x-ray spectroscopic studies of the electronic structure of TPP are lacking and consequently there is little experimental information of element specific densities of states or the electronic structure near E_F.

1.5 Thesis Organisation

Chapter 2 covers the basic material properties of low-*k* dielectrics and the theoretical background of the experimental techniques used in the thesis. Chapter 3 outlines the experimental aspects of the spectroscopic techniques that are used in the study and the equipment used.

Chapter 4 presents the experimental results on the characterisation of carbon doped oxide (CDO) and the fluorocarbon thin films which form on the surface during etching. To date, detailed spectroscopic studies of the chemical and electronic structure of these materials

are lacking. Section 4.2 investigates the electronic structure of CDO layers to assist in developing a comprehensive understanding of the electrical properties of these materials. Section 4.3 examines the chemical composition of fluorocarbon films, which are deposited in the form of polymeric films on surfaces during plasma etching. Fluorocarbon films are very important to the semiconductor industry due to the wide range of applications.

Chapter 5 deals with the fluorocarbon-based plasma etching (FBPE), which is widely used in the dry etching of ILD layers [1, 2, 3, 20]. Two different ILD's were compared, the standard SiO_2 and ultra low-k (ULK) CDO. The process of optimising the FBPE has been found to be challenging due to the complexity of the fluorocarbon plasma etch mechanism. Section 5.2 aims to use surface analysis techniques to determine how the chemical composition of the SiO_2 surface is altered in a commercial reactor as a function of changes in the chemical composition of the etching plasma. Section 5.3 investigates the chemical composition of the fluorocarbon layers deposited for a range of plasma operational parameters on an ULK dielectric material and the effect this has on the etch rate of the dielectric layer. Correlations were established between the chemical composition and thickness of the fluorocarbon film and the etch rate of the CDO layer.

Chapter 6 investigates the effect of the fluorocarbon films deposited on the surface of CDO material during etching. Several studies have shown that the oxygen containing plasma etches used to remove photoresist can result in the depletion of carbon for up to 100 nm into the CDO films resulting in an increase of the k value [21, 22]. The absence of oxygen from a fluorocarbon plasma leads to the deposition of a thick fluorocarbon film. Section 6.2 aims to determine the plasma operating conditions which result in the presence of a fluorocarbon layer on the surface of the CDO during etching but doesn't impact on the etch rate, as thick fluorocarbon films have been shown to inhibit the etching process [23]. Section 6.3 looks at gas feed ratios and the applied plasma powers on the formation of the fluorocarbon layer on

the CDO surface. This study was carried out using typical plasma etching parameters that would be used in device processing. An issue being addressed in this study is what effect the addition of this oxygen has on the possible depletion of carbon from the substrate. All the etched samples were analysed using x-ray photoelectron spectroscopy (XPS) and the thickness of the low-*k* films were measured by spectroscopic ellipsometry (SE).

Chapter 7 looks at organic semiconductors which are the subject of intense study due to the challenge they pose to our understanding of the physical properties of complex solids and due to technological interest in developing carbon-based electronic devices [24]. The element specific valence and conduction band electronic structure were measured using x-ray emission spectroscopy (XES) and x-ray absorption spectroscopy (XAS), respectively, while the element specific core level electronic structure was measured using a commercial x-ray photoelectron spectroscopy (XPS). Section 7.2 and 7.3 report the results of a study of the electronic structure of free base tetraphenylporphyrin (TPP) and metal tetraphenylporphyrins (Cu, Co, Zn and NiTPP), respectively. Density functional theory (DFT) calculations on CuTPP were compared with the partial density of states (PDOS) spectra. These studies used a variety of synchrotron-radiation-based soft x-ray spectroscopies. The TPP samples studied were in the form of thin films grown in-situ via ultra-high vacuum organic molecular beam deposition.

Finally, Chapter 8 reviews the results, and looks at some possible future directions for this research.

1.6 Additional research undertaken but not included in thesis

Performing surface analysis techniques often involves carrying out collaborative work for various research groups within the university. This led to a number of experiments that the

results of which are not presented in this thesis. My contribution is recognized by the co-authorship in the resulting publications (CuCl [26], TiN [27], ZnO [28])

1.7 References

1. The International Technology Roadmap for Semiconductors, (2001) edition. International SEMATECH, Austin TX. Available at: http://public.itrs.net
2. S. P. Muraska, M. Eizenberg, A. K. Sinha, Chapter 2, "Interlayer dielectrics for semiconductor technologies", Elsevier Academic Press, (2003)
3. M. A. Lieberman, A. L. Lichtenberg, "Principles of plasma discharges and materials processing", John Wiley and Sons, (1994).
4. S. M. Rossnagel, J. J. Cuomo, W. D. Westwood, "Handbook of plasma processing technology: fundamentals, etching, deposition and surface interactions", Noyes Publications, (1989).
5. H. Conrads, M. Schmidt, Plasma Sources Sci. T., 9 (2000) 441.
6. The International Technology Roadmap for Semiconductors, (1998) edition. International SEMATECH, Austin TX.
7. N. Karl, Synth. Met. 133-134 (2003) 649.
8. C.W. Tang, S.A. Van-Slyke, C.H. Chen, J. Appl. Phys. 65 (1989) 3610.
9. J. Kido, K. Hongawa, K. Okyama, K. Nagai, Appl. Phys. Lett. 64 (1994) 815.
10. A. Yamamori, C. Adachi, T. Koyama, Y. Taniguchi, Appl. Phys. Lett. 72 (1998) 2147.
11. H. Fujii, T. Sano, Y. Hamada, K. Shibata, Macromol. Symp. 125 (1997) 77.
12. T. W. Kelley and C. D. Frisbie, J. Phys. Chem. B 105 (2001) 4538.
13. R. Paolesse, C. Di Natale, V. Dall'Orto, A. Macagnano, A. Angelaccio, N. Motta, A. Sgarlata, J. Hurst, I. Rezzano, M. Mascini, A. D'Amico, Thin Solid Films 353 (1999) 245.

14. N. Kobayashi, W. A. Nevin, S. Mizunuma, H. Awaji, M. Yamaguchi., Chem. Phys. Lett. 205 (1993) 5154.

15. R. W. Wagner, J. S. Lindsey . J. Am. Chem. Soc. 116 (1994) 9759.

16. D. E. Barlow, L. Scudiero, and K. W. Hipps, Langmuir 20 (2004) 4413.

17. Lian-Cai Xu, Zun-Yun Li, Wei Tan, Tian-Jing He, Fan-Chen Liu, Dong-Ming Chen Spectrochimica Acta Part A 62 (2005) 850.

18. M.M. El-Nahass, H.M. Zeyada, M.S. Aziz , M.M. Makhlouf, Spectrochimica Acta Part A 62 (2005) 11.

19. L. Scudiero, D. E. Barlow, and K. W. Hipps, J. Phys. Chem. B, 104, (2000) 11899.

20. G. S. Oehrlein, H. L. Williams, J. Appl. Phys. 62 (1987) 662.

21. Y.H. Wang, R. Kumar, X. Zhou, J.S. Pan, J.W. Chai, Thin Solid Films 473 (2005) 132.

22. D. Shamiryan, K. Weidner, W.W. Gray, M.R. Baklanov, S. Vanhaelemeersch, K. Maex, Microelectron. Eng. 64 (2002) 361.

23. T.E.F.M. Standaert, C.Hedlund, E.A.Joseph, G.S.Oehrlein and T.J.Dalton J. Vac. Sci. Technol. A 22 (2004) 53.

24. S.R. Forrest, J. Quant. Elec. 6 (2000) 1072; Chem. Rev. 97 (1997) 1793.

25. Y. Niwa, H. Kobayashi and T. Tsuchya. J. Chem. Phys. 60 (1974) 799

26. G. Natarajana, S. Daniels, D. C. Cameron, L. O'Reilly, A. Mitra, P. J. McNally, O. F. Lucas, R. T. Rajendra Kumar, I. Reid, A. L. Bradley. J. Appl. Phys. 100 (2006) 033520

27. M. Rahman, I. Reid, P. Duggan, D.P. Dowling, G. Hughes, M.S.J. Hashmi. Surface & Coatings Technology, 201 (2007) 4865

28. J. R. Ducle're, R. O'Haire, A. Meaney, K. Johnston, I. Reid, G. Tobin, J. P. Mosnier, M. Guilloux-Viry, E. McGlynn, M.O. Henry. J. Mat. Sci.: Mat. Elec. 16 (2005) 421.

Chapter 2: Theoretical Background

2.1 Introduction

This chapter provides a summary of the theoretical aspects of the materials used in the study and the scientific theory behind the techniques used within this thesis. It also provides a technical insight into the dielectric layers used and the plasma processes involved.

2.2 Dielectric materials

There are a large number of ULK candidate materials and deposition methods being currently researched by various companies as illustrated in Table 2.1. The ASMI (Aurora) material is the ultra low-*k* being researched in this project.

Table 2.1 Ultra low-*k* dielectrics for various companies

Company (Name or trade-mark)	Dielectric Constant	Deposition method
IBM (SiOCH)	2.05	PECVD
Novellus (Coral)	<2.4	
Trikon (Orion)	2.2	
ASMI (Aurora)	2.4	
Applied Materials (Black Diamond III)	<2.4	
DSI	2.2	CVD
JSR (LKD 5109)	2.3	Spin-on
Honeywell (Nanoglass E)	2.2	
Dowchemical (p-SILK)	2.1	
Dow Corning (XLK)	2.2	
Rohm & Haas (Zirkon)	2.2	

The dielectric constant of a material is comprised of three polarisabilities as described in equation 2.1 and schematically illustrated in figure 2.1.

$$\kappa_{total} = \kappa = \alpha_{electronic} + \alpha_{ionic} + \alpha_{dipolar} \quad (2.1)$$

$\alpha_{electronic}$ can be obtained by ellipsometry by squaring the refractive index. The extinction coefficient for the dielectric material under investigation is zero as the film is transparent. α_{ionic} can be measured by Fourier transform infrared spectroscopy (FTIR) and be obtained from the Kramers- Kronig relation analysis [1]. Thus it is possible to determine $\alpha_{dipolar}$ by subtracting these two polarisations ($\alpha_{electronic} + \alpha_{ionic}$) from the total dielectric constant (κ_{total}) which can be obtained by a high frequency capacitance measurement typically at 10^6 Hz known as the static dielectric constant. Therefore, it is possible to determine the component that is the most influential in contributing to the dielectric constant and why the dielectric constant changes with various plasma treatments due to the incorporation of foreign species.

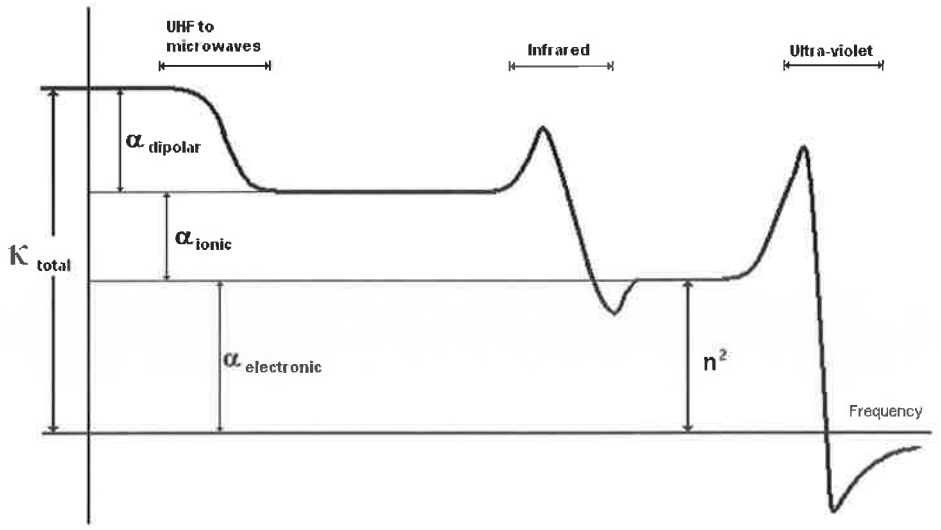

Figure 2.1: Frequency dependence of the several contributions to the polarisability [2]

The total polarisation is given by the Clausius-Mosotti equation [3]

$$\alpha = \frac{3}{4\pi N}\left(\frac{\kappa - 1}{\kappa - 2}\right) \tag{2.2}$$

Where N is the number of molecules per unit volume and κ is the dielectric constant.

Equation 2.2 leads to the definition of the dielectric constant in terms of polarisability:

$$\kappa = \frac{3}{1-(4\pi N\alpha/3)} - 2 \tag{2.3}$$

The higher the molar volume, the lower N will be, which in turn lowers α. Therefore, the higher the molar volume the lower the κ value will be.

The basic equation for capacitance of a parallel plate capacitor is given by:

$$C = \varepsilon\frac{A}{t} = \kappa\varepsilon_0\frac{A}{t} \tag{2.4}$$

ε_0 is the dielectric permittivity in a vacuum, A is the area of the plate and t is the separation. It is clear from equation 2.4 that with a smaller κ value, C will be reduced.

The primary method of reducing the dielectric constant below 4 (SiO_2) is to introduce a porous structure where the air gap has a dielectric constant of 1. Figure 2.2 shows various pore structures. In order to interpret characterisation results and correlate pore size with physical models, it is important to make assumptions about the pore geometry. The complex nature of the porous structure of the various low-*k* materials is such that a theoretical description usually includes simplified assumptions. No single experimental method provides the absolute value of parameters such as porosity, surface area, and pore size. Each experimental method gives a characteristic value which depends on the principles involved and the nature of the analytical tool utilized [4].

Porosity is defined as the fraction p of the total volume of the film comprised by pores: $p = V_p/V$, where V_p is pore volume and V is total volume of the film. Pores are defined to be ''open'' if they are accessible by the analytical technique. Pores with a size smaller than the probe diameter are inaccessible and therefore by definition ''closed.'' Note, however, that different analytical methods will provide different thresholds of open and closed pores [5].

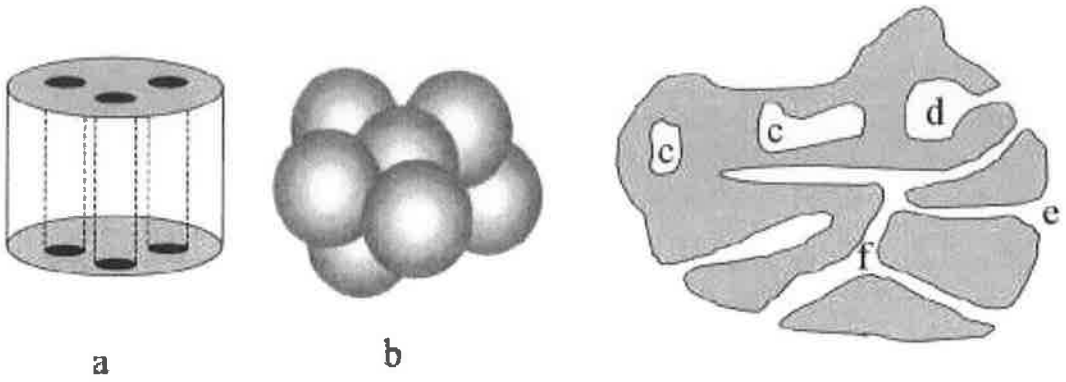

Figure 2.2: Various pore structures (a) cylindrical pores; (b) voids between packed spheres and schematic boundary structure showing (c) closed (latent) pores; (d) ink bottle; (e) funnel; and (f) open pores [5].

Increasing the porosity of a material is one way to reduce its k value. Dielectric materials which have a relatively low-k value based on low polarisability of the material before the incorporation of pores make it possible to achieve even lower k values as a function of increased porosity as indicated in Figure 2.3. For example a mesoporous hydrogen silsesquioxane (HSQ) based material with about 50% total porosity is reported to have a k value of about 1.9 [6] while the k value for a methyl silsesquioxane (MSQ) -based dielectric with about 45% total porosity lies at around 2.0 [7]. There are disadvantages associated with increasing the porosity to a high level such as mechanical issues, thermal expansion and process interactions can be problematic.

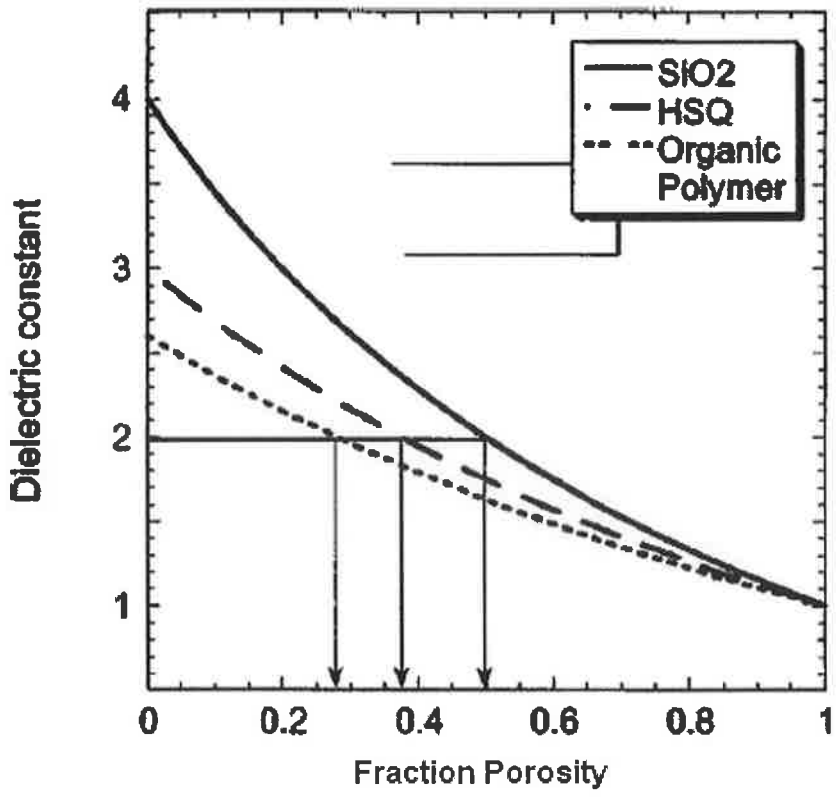

Figure 2.3: Dielectric constant vs. porosity [5].

2.3 Fluorocarbon based plasma etching

2.3.1: General overview on theory and concepts about plasma

A plasma is a partially ionised gas in which free electrons collide with neutral and ionized atoms/molecules. Ionized species are created and destroyed through collisions when an electron can be dissociated from neutral species or recombine with ionized species. Depending on the energy of the particles, collisions can result in the generation of various species, such as negative ions, excited molecules, neutral atoms and ions. A general feature of plasmas is overall electrical neutrality: any charge imbalance would result in electric fields that would tend to move the charges in such a way as to rapidly eliminate the imbalance.

2.3.2: Plasma characteristics and generation

To form and maintain a plasma state requires an energy source to produce the required ionisation. The rate of ionisation in steady state must balance the losses of ions and electrons from the plasma volume by recombination and diffusion in the chamber. A widely used method for generating and sustaining a plasma is by using an electrical breakdown of a neutral gas in the presence of an external electric field [9]. In fact, any volume of a neutral gas always contains a few electrons and ions. These free charge carriers can be accelerated by an electric field and new charged particles may be created when these charges collide with atoms and molecules in the gas or with the surfaces of the electrodes generating the electric field. This situation leads to an avalanche of charged particles that is eventually balanced by charge carrier losses, so that a steady-state plasma develops. The types of plasmas involved in the microelectronic industry are initiated and sustained by electric fields which are produced by either direct current (DC) or alternating current (AC) power supplies. There can be several types of discharges, such as DC discharges, AC discharges, and pulsed discharges depending on the temporal behaviour of the electric field. The typical AC frequencies of excitation are 100kHz, at the low end of the spectrum, 13.56 MHz in the radio frequency (RF) portion of the spectrum, and 2.45 GHz in the microwave region. Such plasmas are also referred to as *electric discharge*, *gaseous discharge* or *glow discharges*, respectively. In the collisions between electrons and ions, the electrons retain most of energy because of their small mass and transfer this energy mainly in inelastic collisions. Thus the electrons and ions may have significantly different temperatures, which give the plasma unique physical and chemical properties.

2.3.3: RF discharges and etching

The main type of discharge used for technical and industrial applications are radio-frequency (RF) discharges, in which a high-frequency electric field is present. This is the case in our

experiments in which a capacitively coupled RF plasma tool was used. Capacitively coupled RF plasmas are the most common plasmas used in dry etching [10], and they are characterized by the presence of a capacitor between the electrode and the power generator and a matching network to adapt the impedance of the power generator to that of the discharge [9]. A conventional reactive ion etching (RIE) system is shown in figure 2.4. The material to be etched is placed on the RF-driven electrode inside a vacuum chamber. An RF power source is applied to the electrode or in some cases it might be applied to the reactor walls.

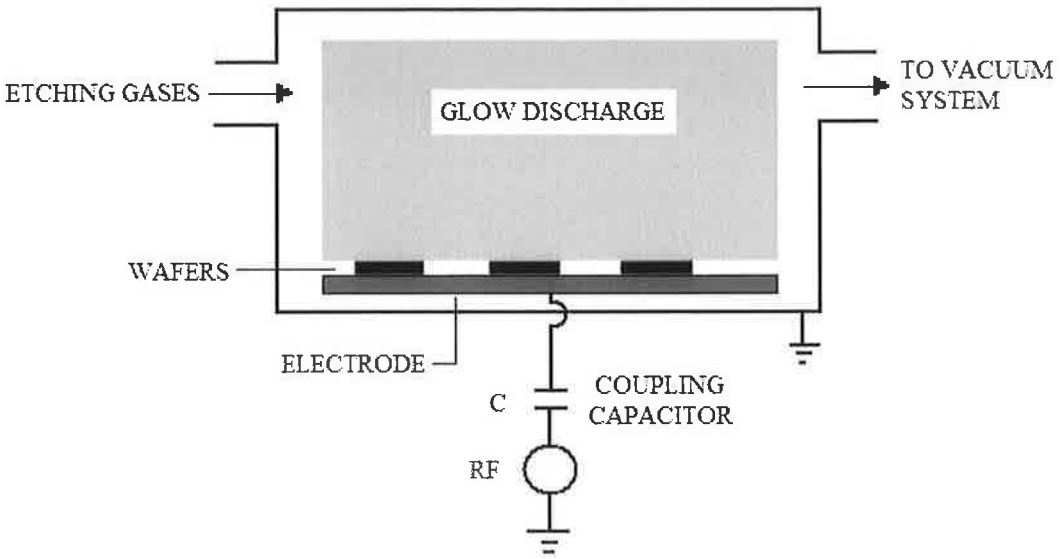

Figure 2.4: Schematic representation of simple capacitively coupled RF plasma etch reactor [9]

Inside the chamber, the mobile plasma electrons respond to the instantaneous electric field produced by the RF driving voltage (figure 2.5), oscillate back and forth within the positive space charge of the ions. The electrons also have far higher thermal velocities than the ions due to their smaller mass. On the contrary the ions, because of their mass, respond only to time-averaged electric fields and have smaller thermal velocities. The electrons tend to thermally diffuse to the capacitively-isolated electrode faster and hence charge it negatively. This creates a sheath layer close to the electrode with an electric field directed towards the

electrode which equalises the ion and electron current to the electrode in steady state. Hence, ions flowing out of the bulk plasma near the centre of the discharge can be accelerated by the sheath field to high energies as they impinge on the substrate, leading to energetic-ion enhanced processes and reactions at the surface which is the etch process.

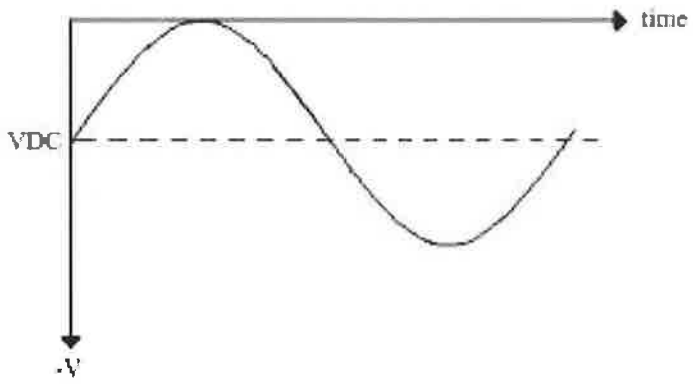

Figure 2.5: DC and AC voltage of the powered electrode: the DC voltage superimposed to the RF driving voltage is a direct consequence of the capacitor coupling the AC power source and the electrode.

The reactions occur with the unmasked areas of the wafer and lead to the formation of volatile products, which enter the gas phase. Thus reactive ion etching (RIE), which is a dry etching technique, is substantially characterized by the fact that it combines physical sputtering with the chemical activity of reactive species.

A schematic summary of the processes taking place in the system during reactive ion etching are the followings [11]:

- Active species generation: electron-impact dissociation/ionisation in a glow discharge (with a suitable feed gas, e.g. C_4F_8 in the case of silicon and silicon dioxide) is used to generate the gas phase etching environment which consists of radicals, positive and negative ions, electrons, and neutrals.

- Formation of a DC bias for ion acceleration. The material to be etched is placed on the high-frequency-driven (13.56 MHz) capacitatively coupled electrode. Since the electron mobility is much greater than the ion mobility, after ignition of the plasma the electrode acquires a negative charge (the corresponding voltage is called self-bias voltage). Therefore, the electrode and material placed on the electrode will be exposed to energetic, positive ion bombardment.
- Transport of plasma-generated reactive intermediates from the bulk of the plasma to the surface of the material being etched: this occurs by diffusion and influences the etch rate.
- Adsorption step: reactive radicals (e.g. F atoms) adsorb on the surface of the material (e.g. Si) to be etched. This step can be strongly enhanced by concurrent ion bombardment which serves to produce "active sites" since it aids in the removal of the surface layers which otherwise may passivate the surface.
- Reaction step: a reaction between the adsorbed species and the material to be etched must take place. In the case of fluorine-based etching of silicon, chemical reactions between the fluorine atoms and the surface produces volatile species (like SiF_4 or SiF, SiF_2, SiF_3).
- Desorption of volatile reaction product: desorption of the reaction product into the gas phase is one of the most critical steps in the overall etching reaction. This removal can be greatly accelerated by ion bombardment via sputtering.
- Pump out of volatile reaction product: the desorbed species must diffuse from the etching surface into the bulk of the plasma and then be pumped out. Otherwise plasma induced dissociation of product molecules will occur and redeposition can take place.

Although many of the physical and chemical processes underlying plasma etching are not completely understood yet, this technique meets some of the major technological requirements for processing, such as etch directionality (anisotropy) and selectivity [10].

Under certain conditions, the plasma deposits a passivating polymer on the surface it interacts with. Since the feed gases suitable for etching on SiO_2 contain fluorocarbon compounds, the polymer is normally formed by C and H/or F atoms provided, resulting in a $C_xF_yH_z$ polymer. The formation of the polymer does not only occur on the wafer, but on all the reactor surfaces (which can result in negative consequences such as redeposition of particulates that locally prohibit etching, resulting in a rough surface or incomplete removal of the etched layer). The polymer is removed by sputtering in regions where the ions bombard the surface and the chemical etching can continue. Whereas in the regions where the ions do not strike the surface (i.e. vertical sidewalls) the polymer is not removed and the chemical etching is impeded.

In most real scenarios both etching and deposition mechanisms can take place and the detailed values of the process parameters will determine which mechanism dominates. However, since the bombardment only occurs on horizontal surfaces the etching is only enhanced or enabled on such surfaces, resulting in an anisotropic etching as shown in figure 2.6.

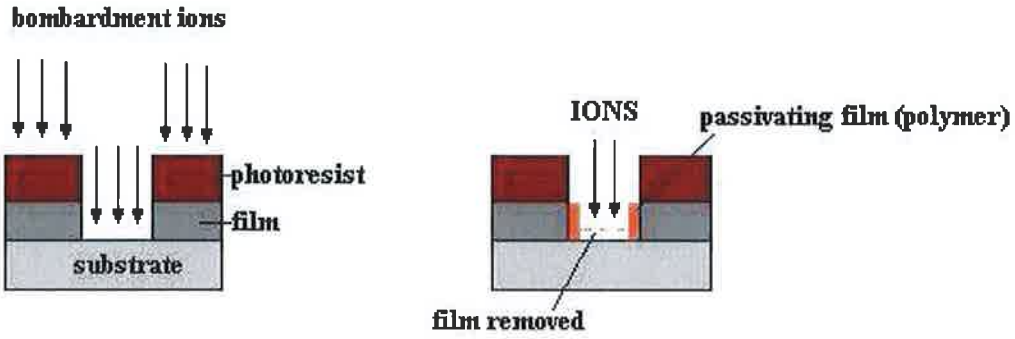

a) b)

Figure 2.6: Example of a substrate with metal film and photoresist to show the role of ion bombardment: ions leaving the discharge bombard the bottom of the trench but leave the sidewalls unaffected, leading to anisotropic etching. (a) Either the ion bombardment increases the reaction rate at the surface, or (b) it exposes the surface to etchants removing passivating films that cover the surface.

In general, as mentioned above, the actual etching is primarily a chemical etching, not a physical sputtering one. A chemical reaction takes place between the solid atom (from the film to be etched) and gas atoms to form a molecule, which is removed from the substrate. Since a DC bias is always present, as already seen there's always some sputtering but it plays such a negligible role in directly etching the film material that it can be mainly neglected. When the gases enter the reactor in the form of molecules, the molecules aren't reactive enough in most cases to react chemically with the surface. The ionisation in the discharge dissociates the molecules into chemically reactive atoms (radicals).

2.4 X-ray Photoelectron Spectroscopy (XPS)

Historically the dominant technique used to directly measure the chemical composition of materials has been X-ray photoelectron spectroscopy (XPS). It was predominantly developed in the 1950s and 1960s as an analytical tool. It was discovered that precise measurement of the electronic binding energies could offer information about the elemental structure of the sample in addition to information concerning the chemical environments of the elements nearby.

Surface analysis by XPS is accomplished by irradiating a sample with monoenergetic soft x-rays and analyzing the energy of the detected electrons. Mg K_α (1253.6 eV) or Al K_α (1486.7 eV) x-rays are the most commonly used excitation sources. These photons have limited penetrating power in a solid on the order of about 1-10 microns. They interact with atoms in the surface region, causing electrons to be emitted by the photoelectric effect. The basic physics behind the process can be described by the Einstein equation [12], which states:

$$E_B = hv - \mathrm{KE} \tag{2.5}$$

where E_B is the binding energy of the electron in the atom, hv is the incident photon energy and KE is the kinetic energy of the emitted electron. It is therefore evident that the quantity E_B can be easily obtained from the known value for hv, and the measured value of KE. The E_B of an emitted photoelectron is the energy difference between the *(n-1)*- electron final state and the n-electron initial state, which can be summarised by the following:

$$E_B = E_f(n-1) - E_i(n) \tag{2.6}$$

An approximation of the E_B can be obtained from Koopmans' Theorem [13] by assuming no rearrangement of the other electrons in the atom or material occurred during the photoelectron emission process. The result is that the E_B of the electron is simply equal to the negative orbital energy, $-\varepsilon_k$, summarised as:

$$E_B \approx -\varepsilon_k \tag{2.7}$$

This typically yields values that are within 10-30 eV of the experimentally obtained values for E_B. However, this simple approximation does not account for all the contributions to the E_B of the electron. In particular, the main omissions in this equation are a result of the assumption that the other electrons in the atom do not react to the emission of the photoelectron.

During emission of the photoelectron other electrons will respond to the creation of a core hole which results in the other electrons in the atom rearranging in order to minimise the energy of the ionised atom. This rearrangement of the electrons is called the relaxation energy. This final state effect, represented by $E_r(k)$ in equation 2.8, occurs both in the newly ionised atom and in the surrounding atoms. Further corrections to equation 2.7 occur due to electron correlation ($\delta\varepsilon_{corr}$) and relativistic ($\delta\varepsilon_{rel}$) effects. The addition of these amendments results in a more complete description of E_B:

$$E_B = -\varepsilon_k - E_r(k) - \delta\varepsilon_{corr} - \delta\varepsilon_{rel} \tag{2.8}$$

Typically the correlation and relativistic effects are small in magnitude however, and are frequently neglected in the calculation of the binding energy. Figure 2.7 shows the photoelectron emission process whereby photons with sufficient energy $h\nu$ are absorbed by a system causing core electrons to be ejected from the sample. It can be seen from the diagram

that Einstein's equation 2.5 does not take into account the work function of the sample Φ_s. The workfunction of a sample is the minimum energy that an emitted photoelectron must possess before it will be able to leave the sample. The equation for the E_B now becomes:

$$E_B = h\upsilon - \mathrm{KE} - \Phi_S \tag{2.9}$$

For a sample that is grounded to the spectrometer, the measured *KE* of the electron is reduced by Φ_{sp}- Φ_s. Knowledge of the incoming photon ($h\nu$) energy and the work function of the spectrometer (Φ_{sp}) and measurement of the kinetic energy via an electron analyzer makes it possible to calculate the binding energy according to:

$$E_B = h\upsilon - \mathrm{KE} - \Phi_{sp} \tag{2.10}$$

It is clear that in order to accurately calculate the E_B of a sample core level using equation 2.10, it is necessary to first know Φ_{sp}, the workfunction of the spectrometer.

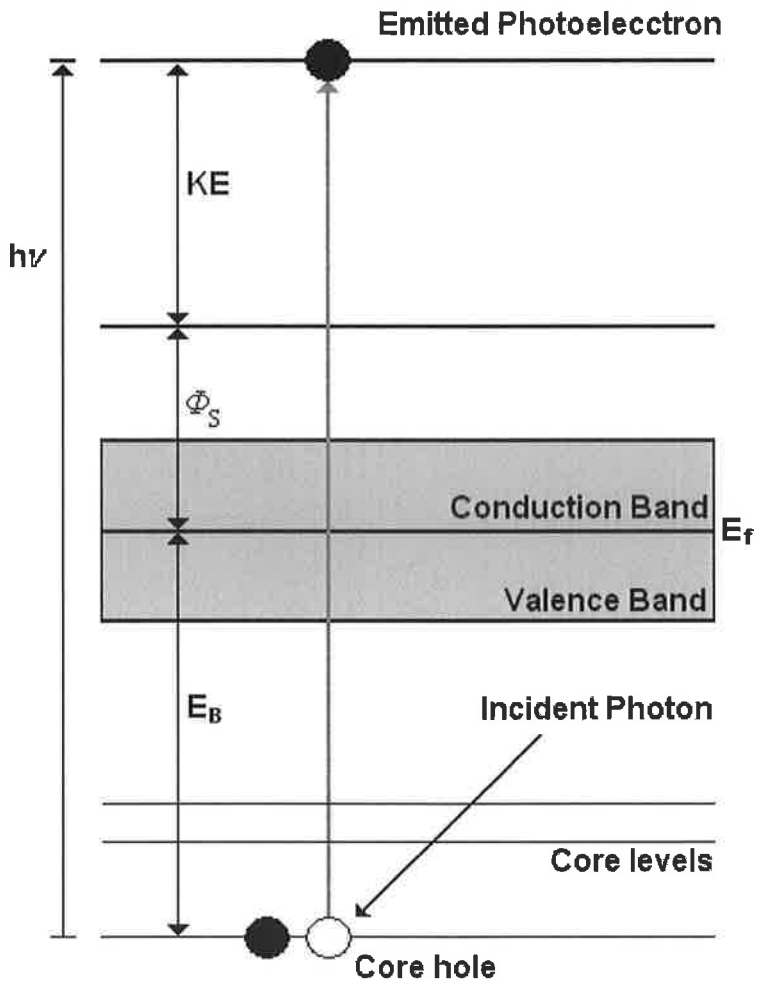

Figure 2.7: An example of a photoelectron emission process, where an incident photon transfers all its energy to a core level electron.

2.4.1 Surface sensitivity and the universal curve

For each and every element, there will be a unique set of energy levels which means that the XPS spectrum contains information on the chemical composition of a sample. The intensity of the peaks is directly related to the concentration of the element within the sample. Figure 2.8 shows a comparison of the photon penetration depth and electron escape depth at the surface of a sample. Depending on the energy of the incoming photon, it may penetrate up to 500 Å into a material before interacting with an electron. The spectra are made up of electrons that

have been elastically scattered within the sample and also from electrons that have been inelastically scattered. The inelastic mean free path (IMFP) (λ) is defined as the average distance that an electron with a given energy travels between successive inelastic collisions. Figure 2.9 show the IMFP as a function of electron kinetic energy. In the range of approximately 10 – 1000 eV, the IMFP is 1 nm or less. The sampling depth is defined as 3λ from which 95% of the detected photoelectrons originate. So while the penetration depth of x-rays can be in the μm range, the depth into the solid from which photoelectrons are detected without suffering a collision is less than 10 nm. This is what gives the technique its surface sensitivity. The electrons that reach the analyzer having suffered energy loss in an inelastic collision will contribute to the background signal which increases on the low kinetic energy side of the peak. The electrons that have been elastically scattered give rise to the sharp intense XPS peaks.

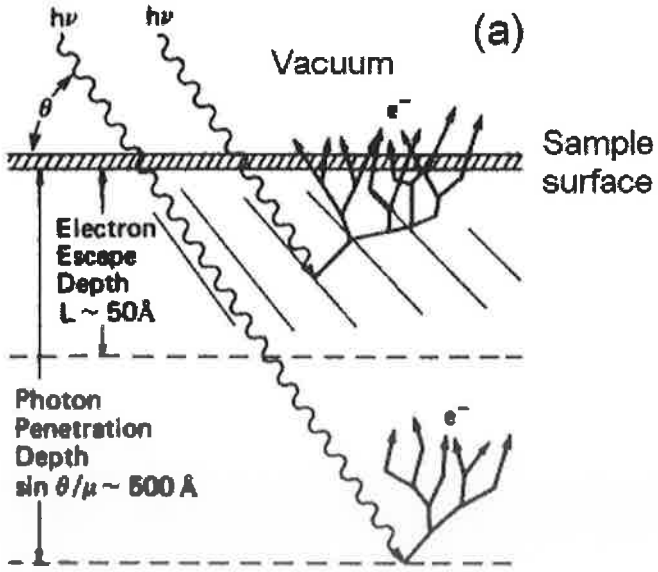

Figure 2.8: A comparison of the photon penetration depth and electron escape depth at the surface of a sample [14]

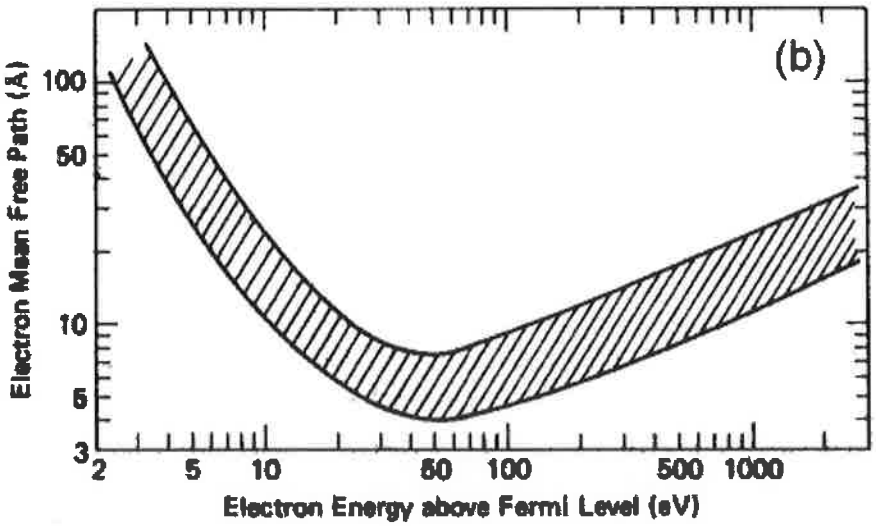

Figure 2.9: Universal mean free path versus electron kinetic energy above the Fermi level [14].

2.4.2 Analysis of spectra

Since binding energies of core electrons are characteristic for elements, XPS allows for a determination of the atomic compositions of a sample. In many cases, chemical shifts can be used to draw direct conclusions on the local coordination in a system and the electronic change upon adsorption.

The peak width is due to the core hole lifetime and the instrument broadening due to the resolution of the spectrometer. The core hole lifetime contribution can be calculated from the Heisenberg's uncertainty relationship [12] and is Lorentzian in nature:

$$\Gamma = h/\tau \tag{2.11}$$

Where Γ is the intrinsic width of the peak in eV, h is Planck's constant in eV-seconds and τ is the core hole lifetime in seconds. The lifetime of the core hole is dictated by how fast another electron can fill the hole, the value of τ, the core hole life time, will be shorter for inner shell electrons compared to that of outer shell electrons. This is due to a high probability of outer electrons falling to fill the inner core holes. Thus the deeper the core hole the shorter the core hole lifetime will be and the larger the intrinsic peak width. It is evident from equation 2.11 that there is a reciprocal relationship between the lifetime of the core hole created, and the width of the observed XPS peak. In practice the overall shape of an XPS peak is a combination of the intrinsic Lorentzian lineshape of the core level and a Gaussian component, which takes instrumental broadening of the Lorentzian component into account. The main contributions to the Gaussian component are due to the energy spread of the incident radiation and the resolution of the analyzer [12]. In the case of conventional XPS studies (using a Mg or Al lab source), the energy spread of the incident x-rays result in instrumental broadening dominating the line shape and the peaks become essentially Gaussian in nature. Studies using synchrotron radiation light sources coupled with high resolution monocrometers have far less instrument broadening reducing the Gaussian component because of the typically narrower bandwidth of the excitation energy.

Atoms at the surface of a sample are unique in the way that they are bonded to their neighbours and they differ from atoms in the bulk of the sample. This is due to the next atomic layer being missing and its absence results in a change in chemical environment compared to atoms in the bulk of the material. It is evident that atoms at the very surface have partially filled bonds. What often occurs is that the surface atoms will rearrange and form bonds with other surface atoms in order to reduce their energy. As already mentioned, XPS is a highly surface sensitive technique which gives it the ability to detect atoms in different chemical environments by energy shifts in the spectral components. When viewing the core

level spectra of atomically clean surfaces it is often possible to see two component peaks, one which is due to the bulk atoms, and one which is attributed to the surface atoms [15, 16].

2.4.3 Peak Shifts

Correctly determining the core level peak shifts is necessary for maximisation of the potential uses of XPS as an analytical tool. As mentioned already, surface reconstructions often result in the introduction of a new core level component in the XPS spectra. However, there are many other effects that create new core level components, which must also be considered for correct analysis of data.

2.4.3.1 Initial state effects

Equation 2.6 illustrates that both the initial and final states effects contribute to the observed E_B. The initial state is basically the ground state of the atom prior to the emission of a photoelectron. It can be seen that a change in the atom's initial state energy $E_i(n)$ will result in a change in the E_B of the core level. The initial state of an atom is changed by the formation of chemical bonds with other atoms. For most samples it is found that the final state effects such as relaxation have similar magnitudes irrespective of the initial state energy. In these cases it can be shown that the change in the E_B of the core level is equal to the change in magnitude of the orbital energy ε_k yielding the formula:

$$\Delta E_B = -\Delta \varepsilon_k \tag{2.12}$$

In general, the creation of a bond that results in a negative charge transfer from the atom under study to its bonding partner will result in an increase in the E_B of the atom relative to its unbonded state, while negative charge transfer from the bonding partner to the investigated atom will result in a decrease in the E_B relative to its unbonded state.

2.4.3.2 Final state effects

Within an atom involved in the XPS process, the principal final state effect is known as relaxation effects. This was mentioned briefly earlier; the creation of a core hole in an atom by the emission of a photoelectron will result in a rearrangement of the remaining electrons in order to minimize the energy of the ionized atom. This results in a decrease of the E_B of the measured photoelectron. Additional extra-atomic relaxation is also experienced in numerous cases as the surrounding atoms contribute to the minimisation of the energy of the ionised atom, however this is usually neglected. The type of extra-atomic relaxation depends largely on the material being analyzed. For conducting samples, valence band electrons move from one atom to the next in order to screen the core hole. For ionically bonded materials electrons are not free to move from one atom to the next. The electrons in these materials can be polarized by the presence of a core hole. The extra atomic relaxation is smaller for ionic bonded materials than metallic samples.

While relaxation or screening effects are the final state effects that are observed to dominate on both the atomic and inter-atomic scales, additional atomic level final state effects are also often observed in XPS. The two main further causes are multiplet splitting and shakeup satellites. Multiplet splitting results from the interaction of the core hole with unpaired electrons in its outer orbitals. Shakeup satellites develop from the outgoing photoelectron losing part of its kinetic energy to excite a valence electron into an unoccupied state. These effects result in the loss of kinetic energy of the outgoing electron, which is observed as an increase in the E_B of the investigated core level.

2.5 Synchrotron Radiation (SR) Techniques

Due to the development of high brightness synchrotron sources and advances in instrument construction over the past 20 years, the technique of X-ray absorption has become a very large

field of research in itself. X-ray emission has been in existence for much longer [17]. Early studies used rotating anode sources and very long integration times. Early 80s studies used bending magnets [18]. With the construction of undulator insertion devices, then x-ray emission became routinely practicable. X-ray emission spectroscopy has only been developed in the last 15 years [25] due to the high intensity light generated by undulator beam lines. When united with x-ray absorption spectroscopy, which taken together is more generally know as resonant inelastic x-ray scattering [19], both can offer an enormous insight into the electronic structure of complex materials such as those studied in this thesis

2.5.1 X-ray Absorption Spectroscopy (XAS)

X-ray absorption spectroscopy (XAS) measures the spectrum of transition probabilities between a core level and unoccupied states of the conduction band of a material [14]. Figure 2.10 illustrates a schematic diagram of the electronic structure of a solid and the x-ray absorption process. X-ray absorption spectroscopy is responsive only to the density of electronic states and does not measure any elements of the band structure of a material. XAS is divided into two regimes: Near Edge X-ray Absorption Fine Structure (NEXAFS) for bound states and low energy resonances in the continuum, and Extended X-ray Absorption Fine Structure (EXAFS) when the outgoing electron is well above the ionisation continuum. NEXAFS uses the absorption of synchrotron radiation as a means of studying the orientation of molecules on surfaces. The absorption process occurs in two steps, firstly by exciting electrons from a core level into an unoccupied molecular state above the Fermi level. Core hole annihilation occurs, which involves the filling of the created core hole by a valence electron, the surplus energy is released via the emission of either (a) an Auger electron or (b) a fluorescent photon.

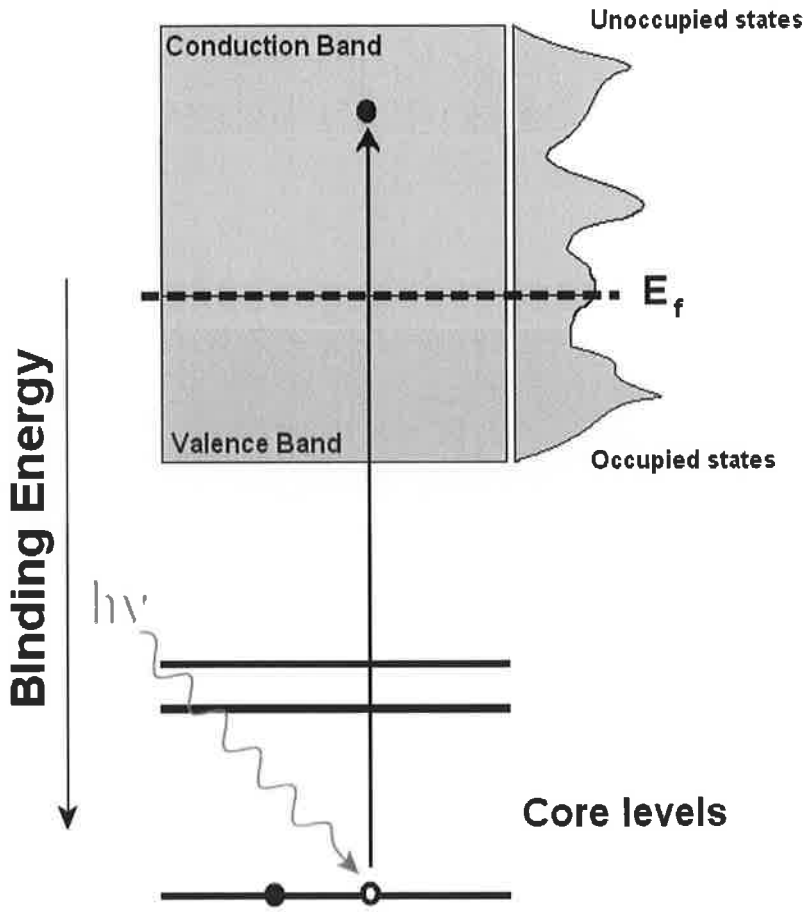

Figure 2.10: A schematic diagram of the electronic structure of a solid and the x-ray absorption process. The process involves an x-ray photon exciting a core level electron into an unoccupied state above the Fermi level [14].

The probability of the x-ray absorption process taking place can be calculated using Fermi's 'golden rule'. The transition probability per unit time P_{if} from the initial state $|i\rangle$, to a final state $|f\rangle$, driven by a harmonic time-dependent perturbation $V(t) = V_0 e^{-i\omega t}$

$$P_{if} = \frac{2\pi}{\hbar}\left|\left\langle f\left|V_0\right|i\right\rangle\right|^2 \zeta_f(E) \qquad (2.13)$$

where ($\zeta_f(E)$ is the energy density of final states. The spectra presented in this thesis all involve a *K*-shell core-level electron as the initial state, and a final state with a free electron in the potential of the ionized atom. The dipole approximation introduces restrictions about which transitions are allowed for the atomic / molecular electrons. The wavelength, λ, of soft x-ray photons is of the order of several Å. The spatial extent, |x|, of *K*-shell atomic orbitals can be estimated by $|x| \approx 2a_0/Z$, where $a_0 = 0.53$ Å is the Bohr radius, and Z is the atomic number. For the carbon *1s* shell this equates to $|x| \approx 0.18$ Å. As $|x| \ll \lambda/2\pi$ the dipole field of the photon dominates the interaction and the dipole approximation can be used. This leads to the dipole selection rule for XAS:

$$\Delta l = \pm 1 \tag{2.14}$$

Where l is the azimuthal quantum number. Therefore, if a transition involves a *K*-shell, for example a C *1s* electron, then only transitions to p shell unoccupied states are allowed, and thus it is the partial density of states (PDOS) of a material that XAS measures. The excited state generated by the x-ray absorption process can decay by means of two main methods as mentioned earlier. For light elements more often than not, the main mechanism is due to Auger decay, or the related Coster- Kronig process. These decay channels excite a large numbers of low energy electrons from the surface of the sample. The number of electrons produced is directly related to the number of x-rays absorbed, which directly gives a means by which the x-ray absorption transition probability may be measured experimentally. This is called the total electron yield (TEY) or sample drain current method. The second method involves the radiative decay of a valence electron into the core hole. If the flux of x-ray photons emitted by the sample is measured, then this gives us another means to indirectly examine the underlying x-ray absorption process. This is called the partial fluorescent yield

(PFY) method [14]. The data shown in this thesis is all carried out by the TEY method. The spectral features that are observed using XAS are, in many cases, not solely due to the unoccupied states of the material as will now be discussed. Schematic spectra, and the corresponding potential diagrams, for an atom and a diatomic molecule are shown in Figure 2.11.

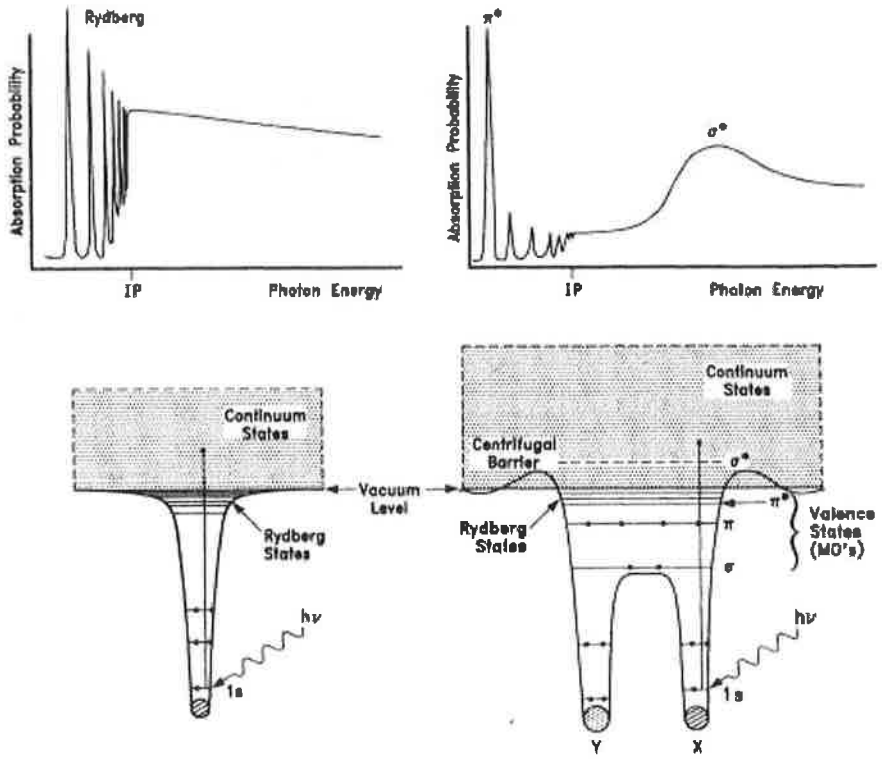

Figure 2.11: Schematic potentials (bottom) and *K*-shell x-ray absorption spectra (top) for an atom and a diatomic molecule [14].

In the case of a single atom, the Coulomb interaction between the core-hole state and the excited electron gives rise to a series of Rydberg orbital states in the potential well of the atom. Excitations into these states produces discrete peaks in XAS spectra at energies slightly lower than the true ionisation potential (IP) of the atom. For a diatomic molecule shown in figure 2.11 numerous factors change. First of all, the core level states of each atom of the

molecule are in fact isolated in their own potential wells, that is they are strongly localized near the atomic cores. This indicates that if the atoms of the molecule are different, then local, atomically specific, electronic structure information can be acquired by exciting only one type of atom. Secondly, the electron states associated with bonding in the molecule are within a common potential well. Also contained by this well are the unoccupied or anti-bonding states (π^*) and finally molecular Rydberg states. In larger molecular structures the distinction between XAS features from unoccupied states, and Rydberg states, is less defined and a certain quantity of incorporation occurs. Furthermore, a core-hole excitonic state can exist due to the interaction between the core-hole charge and the lowest unoccupied molecular orbital (LUMO) state. This is usually seen as a strong discrete feature several eV below the IP of the atom. The feature marked σ^* in the diatomic spectrum of Figure 2.11, is due to the existence of a σ symmetry unoccupied state in the continuum of states. The presence of this state enhances x-ray absorption over that produced by the continuum alone. The measurement of this pre-ionisation detail in the XAS spectra of solids is called near edge x-ray absorption fine structure (NEXAFS) spectroscopy.

2.5.2 X-ray Emission Spectroscopy (XES)

Soft x-ray emission spectroscopy involves the measurement of the spectrum of x-rays emitted by the radiative decay of valence electrons into core-hole states [20, 21]. The core-hole can be created either by electron bombardment, or through the x-ray absorption process described in section 2.4.1. The data presented in this thesis were all measured with excitation by soft x-ray absorption.

Soft x-ray emission is an optical process and therefore the dipole selection rule $\Delta l = \pm 1$ applies. The energies used are in the range of 150 eV to 1000 eV. When incident photon energy is greater than the ionisation potential of the atom, the core electron is kicked out of

the system and the non-resonant soft x-ray emission spectrum is observed. This can also be commonly referred to as above threshold or also as "normal" emission or normal fluorescence [26]. A schematic representation of this non-resonant process is illustrated in Figure 2.12. Therefore, in the non-resonant case, the spectrum of x-rays that is measured reproduces the partial density of occupied states of the valence band.

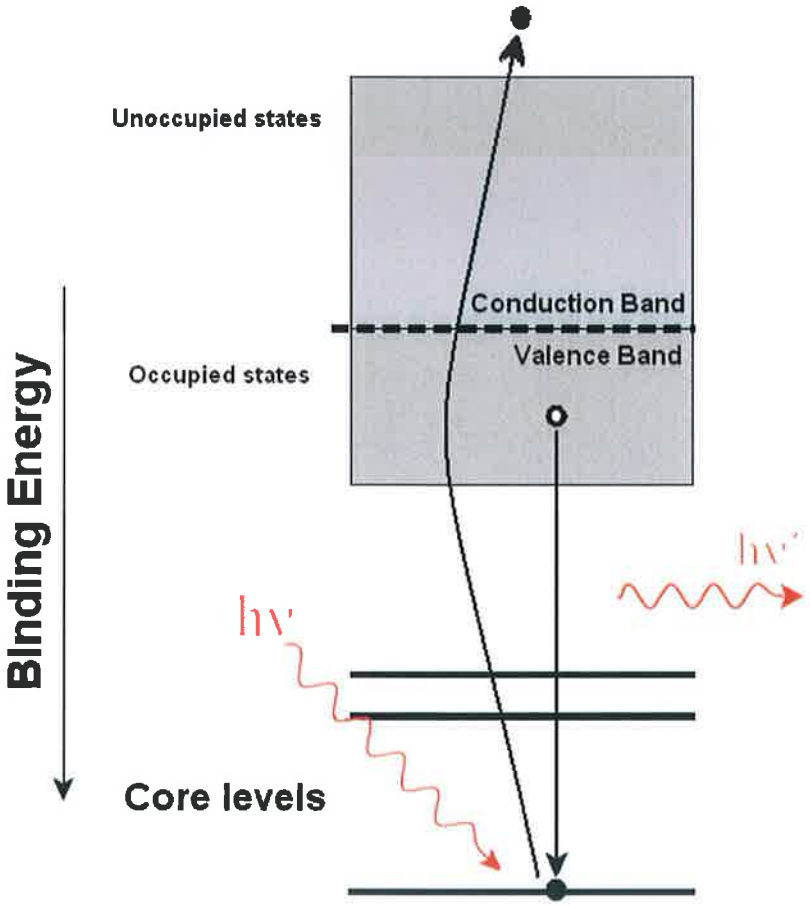

Figure 2.12: A schematic diagram of the non-resonant x-ray emission process. An x-ray photon removes a core level electron from the system and a valence electron fills the core-hole via a radiative transition [25].

If, on the other hand, the core electron is excited into an unoccupied, but bound, state near the Fermi level, then this electron strongly affects the emission process, and it is best modeled as a scattering event [22, 23, 24]. The cross-section for this second order process is described, in the dipole approximation, by the Kramers-Heisenberg formula:

$$\frac{d\sigma}{d\Omega} \propto \left| \sum_m \frac{\langle f|p.A|m\rangle\langle m|p.A|i\rangle}{E_m - h\nu - i\Gamma_m/2} \right|^2 .\delta\left(E_f + h\nu' - E_i - h\nu\right) \qquad (2.15)$$

where $h\upsilon$ and $h\upsilon'$ are the incident and emitted photon energies, $|i\rangle$ is the initial core state, $|m\rangle$ is the intermediate electron plus core-hole state, E_m and Γ_m the energy and width of the intermediate state, $|f\rangle$ is the final state after the radiative decay, and $p.A$ is the dipole operator. In crystalline materials this can lead to a conservation of crystal momentum in addition to energy and angular momentum, see Figure 2.13a,b. This allows information on the band structure of a material to be obtained via x-ray emission spectroscopy. This is only true for "soft" x-ray emission, as soft x-ray photon carries very little crystal momentum in inverse Angstroms due to its long wavelength (a few Angstroms), and thus you get near vertical transitions on a bandstructure diagram but only for such "soft" x-ray emission.

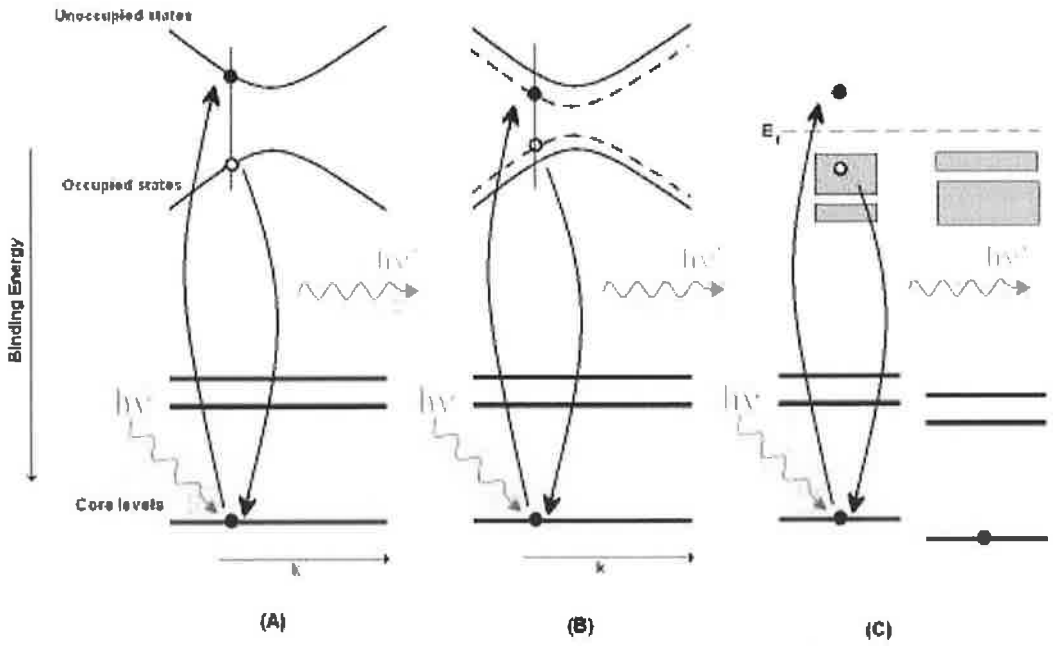

Figure 2.13: Energy schematics of the resonant x-ray emission process. [25]

If the core electron is resonantly excited into an unoccupied band near the Fermi level, then crystal momentum, as well as energy and angular momentum, are conserved and the emission spectrum contains information on the band structure of the crystal. In a non-interacting, or frozen orbital approximation the process proceeds as in (a). The interaction between the core-hole state and the valence and conduction states modifies the band structure, resulting in excitonic bands in the band gap (b). In a molecular picture, the binding energy of the core level is modified by its chemical environment (c). This allows an atom in a particular chemical environment to be selectively exited via resonant excitation of its core electron into an unoccupied state. Interaction between the core-hole and the valence band leads to excitonic states in this case also.

If a molecule includes multiple atoms of the same element but with differing chemical environments, then the energies of their core-levels may have different oxidation states such

that transitions between these chemically shifted core levels and unoccupied states maybe excited independently, see Figure 2.13c This gives both chemically and symmetry specific information in the resulting x-ray emission spectrum, and is called resonant x-ray emission spectroscopy (RXES). The binding energies of the chemically shifted core levels can be measured separately using XPS as mentioned previously. When the spectroscopic techniques of XPS, NEXAFS and RXES are combined, it becomes possible to measure the detailed, elemental, chemical, and symmetry specific electronic structure of molecular solids.

2.5.3 Beam Damage

High resolution XES measurements require a small photon spot (circa 40 μm) with a high photon flux (10^{13} ph/s) on the sample, and long collection times (60 - 90 min). It has been shown previously that these conditions lead to significant beam damage in organic systems [26], and the problem has been solved by continuously translating the films in front of the beam (at 40 μm/s) as the spectra are being recorded [27]. This technique has a dramatic effect on the measured XES spectra from organic thin films. Unless otherwise stated all the XES spectra have been translated.

2.6 Secondary Ion Mass Spectroscopy (SIMS)

SIMS is the mass spectrometry of ionised particles which are emitted when the surface is bombarded by energetic primary particles which may be electrons, ions, photons or fast atoms. The emitted or secondary particles will be electrons, neutral atoms or molecules or atomic and ion clusters. The vast majority of species emitted are neutral but it is the secondary ions which are detected and analysed by mass spectrometry, as schematically illustrated in Figure 2.14.

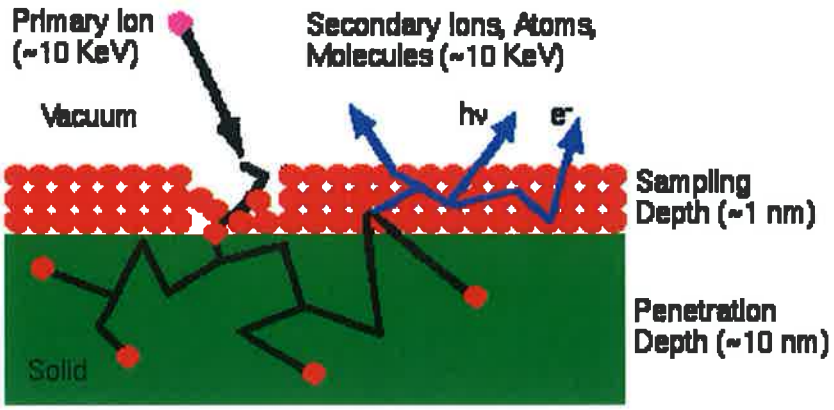

Figure 2.14: SIMS the collision cascade model

The collision cascade model has the best success at quantitatively explaining how the primary beam interacts with the sample atoms. In this model, a fast primary ion passes energy to target atoms in a series of binary collisions. Energetic target atoms (called recoil atoms) collide with more target atoms. Target atoms that recoil back through the sample surface constitute sputtered material. Atoms from the sample's outer surface can be driven in about 10 nm, thus producing surface mixing. The term knock-on also applies to surface mixing. Sputtering leads to surface roughness in the sputter craters. Lattice imperfections, either already present or introduced by surface mixing, can be nucleation centers for roughness that takes the form of ribbons, furrows, ridges, cones, and agglomerations of cones. Polycrystalline materials form rough crater bottoms because of differential sputter rates that depend on crystal orientation [28].

The SIMS ionisation efficiency is called ion yield and is defined as the fraction of sputtered atoms that become ionized. Ion yields vary over many orders of magnitude for the various elements. The most obvious influences on ion yield are ionisation potential for positive ions and electron affinity for negative ions.

The correlations of ionisation potential with secondary ion yields are not perfect. Variations depend both on the sample matrix and on the element itself. For example, the presence of oxygen in the sample enhances positive ion yields for most elements, but fluorine exhibits anomalously high negative ion yields in nearly all samples. Some elements, such as helium and neon fall outside the trend. Other factors affect the secondary ionisation efficiencies in SIMS measurements for example oxygen bombardment increases the yield of positive ions and cesium bombardment increases the yield of negative ions. The increases can range up to four orders of magnitude.

To convert the bombarding time into vertical depth into the sample, a profilometer was used to measure the sputter crater depth. A profilometer determines depth by dragging a stylus across the edge of a crater and noting the vertical deflections.

Accuracy in the depth measurement is determined by the uniformity of the etch. Some SIMS instruments provide uniform sputter rates by sweeping a focused primary beam in a raster pattern over an area. Apertures in the mass spectrometer select secondary ions from the bottom of the crater, but not the edges. Alternatively, the data processing system ignores all secondary ions produced when the primary sputter beam is at the edges of its raster pattern. Mass interferences occur whenever another ion has the same nominal mass as the analyte ion. Such interferences are called isobaric. During the analysis of iron in silicon for example, 28 Si^{+} interferes because it has the same mass (m/z 56) as 56 Fe^{2+}. Oxides are common interferences since oxygen-metal bonds are particularly stable. Thus, 40 CaO^{+} (mass 56) can also interfere with 56 Fe^{+} measurements.

The SIMS primary ion beam, secondary ions, and secondary electrons produce a net charge at the sample surface. If the sample material conducts, this charge can be compensated by a current flow from the grounded sample. However, when an insulating sample is bombarded by

a positive ion beam the surface potential rises due to the implantation of positive charge and the emission of secondary electrons. Sample charging acts to diffuse the primary beam and diverts it from the area being analysed, making it impossible to acquire a stable spectrum. Sample charging also changes the energy distribution of the secondary ions, which affects their transmission and detection by the mass spectrometer. There are two main ways to manage sample charging, and they are often used in combination.

Irradiate the sample surface with a beam of relatively low energy electrons from an electron flood gun which compensates the sample for lost negative charge. The second solution is to use fast atoms as a primary beam in place of ions. Fast atom bombardment (FAB) using a neutral argon atom beam was used in this study of the insulating dielectric layers.

2.7 Spectroscopic Ellipsometry (SE)

Ellipsometry is a measurement technique that uses polarised light to characterise thin films, surfaces and material microstructure. It has a high sensitivity due to the measurement of the relative phase changes in a beam of reflected polarised light, which is more accurate than gathering information from a reflectance measurement. Due to this reason ellipsometric results are highly accurate and most of all repeatable. The measurement values are expressed as psi (Ψ) and delta (Δ). [29]

The p-direction is defined as lying in the plane of incidence. The plane of incidence contains the incident and reflected beams and the vector normal to the sample surface. The *s*-direction lies perpendicular to the *p*-direction such that the *p*-direction, *s*-direction, and the direction of propagation (in that order) define a right-handed Cartesian co-ordinate system. The *p*- and *s*-directions are shown in figure 2.15.

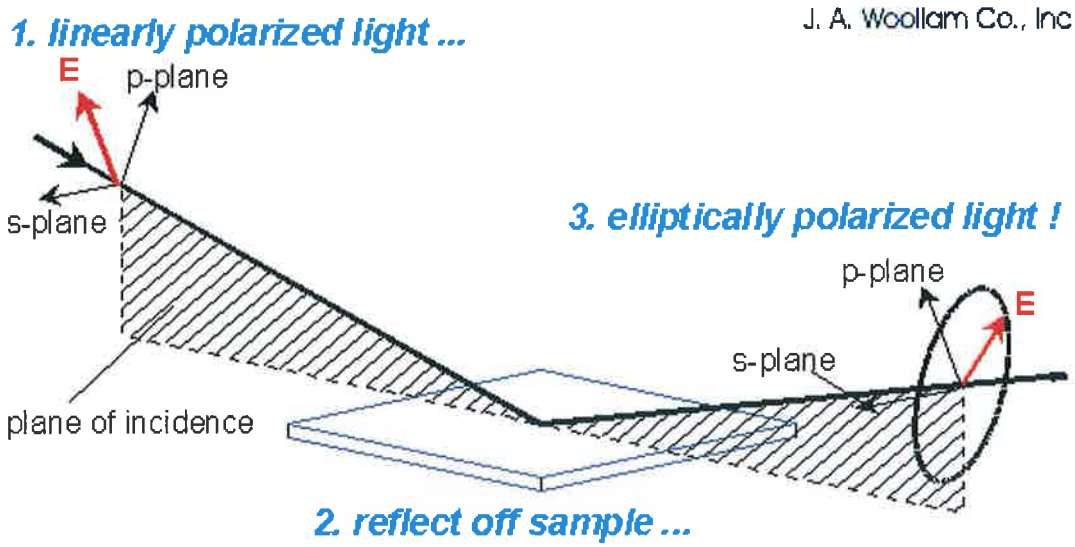

Figure 2.15: Geometry of an ellipsometric experiment, showing the P- and S- directions [29]

The measured values of psi (ψ) and delta (Δ) are related to the ratio of the Fresnel coefficients R_p and R_s for *p*- and *s*- polarized light, respectively.

$$\rho = \frac{R_p}{R_s} = \tan(\psi)e^{i\Delta} \tag{2.16}$$

where ρ is the Ratio of the Fresnel reflection coefficients. Because the ratio is a complex number, it also contain "phase" information (Δ), which makes the measurement very sensitive.

Illustrated in Figure 2.16 are the multiple reflected and transmitted beams in a thin film. The splitting of the beams into the reflected and transmitted beams quickly reduces the amplitude of subsequent reflections which eventually become negligible. The beams are attenuated more quickly in films with high absorption coefficients.

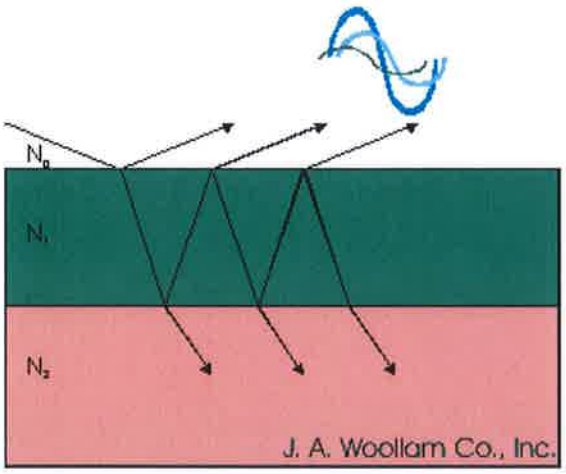

Figure 2.16: Multiple reflected and transmitted beams for a single film on an optically thick substrate [29]

Figure 2.17 shows interference oscillations of delta (Δ) for various thicknesses of silicon dioxide films, the number of which scales directly with the film thickness.

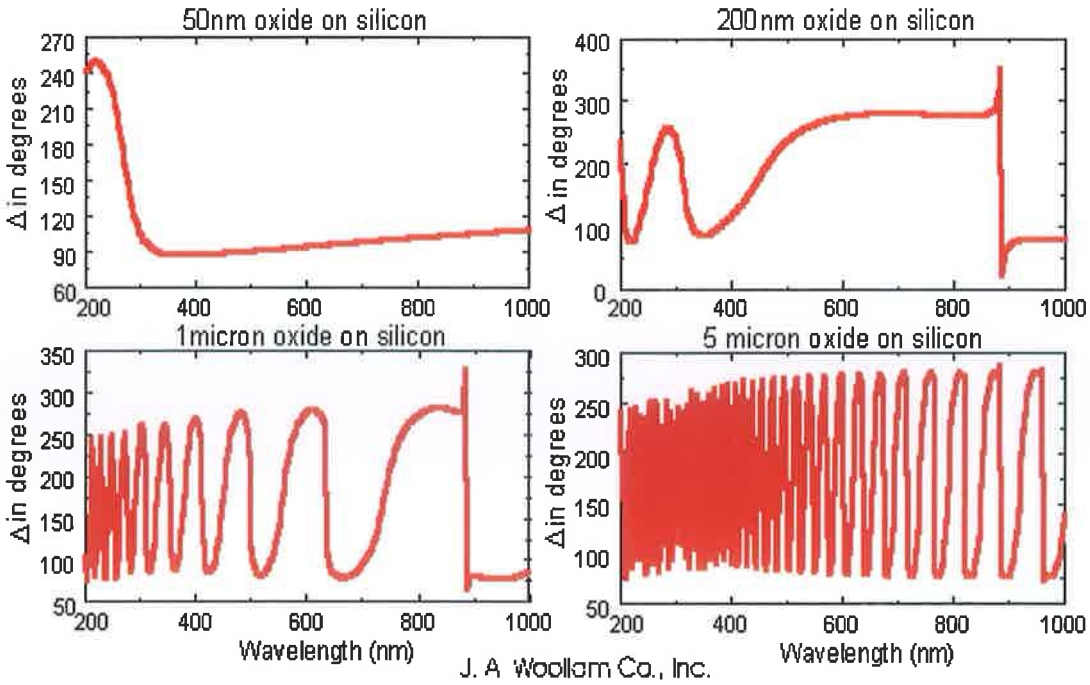

Figure 2.17: Interference oscillations of various oxide thicknesses on silicon [29]

When the ratio of R_p to R_s is known, β, the phase thickness, can be determined and this is then used to calculate the film thickness, d_1, if the refractive index of the film, n_1 is known. The equation for calculating film thickness, at a certain wavelength, λ, is [29]:

$$\beta = 2\pi\left(\frac{d_1}{\lambda}\right)n_1 \cos\theta_1 \tag{2.17}$$

The index of refraction 'n' is the real part of the complex index of refraction

$$\tilde{n} = n + ik \tag{2.18}$$

The index of refraction governs how the phase of the wave changes as it propagates in a material of given index.

There are four main steps in arriving at the goal of gathering useful information about the sample under investigation. Ellipsometry does not directly give this information, instead it gives psi (Ψ) and delta (Δ) values which are fitted to give the sample parameters of thickness, refractive index and extinction coefficient. The block diagram that can be used to show the outline of a procedure that is used to determine the desired values is shown in Figure 2.18 [29].

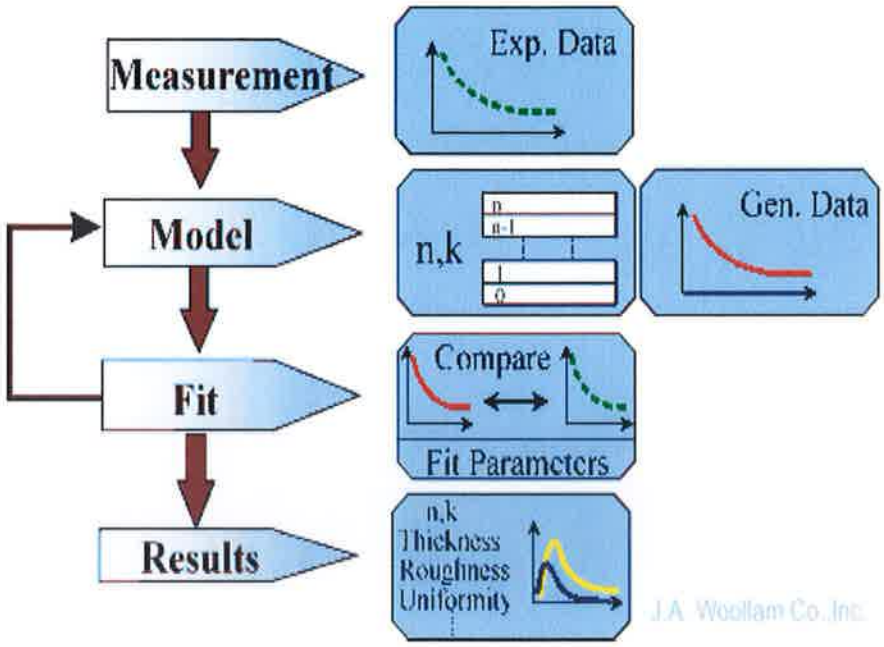

Figure 2.18: Procedure to determine material properties

Measurement: the sample under investigation is measured using the ellipsometer, the values for psi (Ψ) and delta (Δ) are obtained as functions of the wavelength of light. These values have no direct physical significance but using these values can be used to gather the information required.

Development of a model: after the measured values are found, a model is constructed in order to obtain the desired results. To speed up the creation of a model it is useful to have some indication of the sample parameters.

Fitting a model to the measured data: after the model is created a comparison is required to find out how accurate the model is to the optical characteristics of the measured sample. The parameters of the model will then be fine-tuned to match as closely as possible the generated data to the measured data.

Evaluation: After retrieving the best fit-model, the results obtained must be physically reasonable. If this requirement is met then the model should correctly describe the measured

optical data. If there is any discrepancy further model development is carried out before a satisfactory model is generated. [29]

The unknown parameters in the model are adjusted in order to get the best fit between the model and experimental data. The algorithm of doing this fit is to minimise the mean square error (MSE) value which is used to quantify the differences between the experimental and predicted data [30].

$$MSE = \frac{1}{2N - M} \sum_{i=1}^{N} \left[\left(\frac{\psi_i^{\mathrm{mod}} - \psi_i^{\mathrm{exp}}}{\sigma_{\psi,i}^{\mathrm{exp}}} \right)^2 + \left(\frac{\Delta_i^{\mathrm{mod}} - \Delta_i^{\mathrm{exp}}}{\sigma_{\Delta,i}^{\mathrm{exp}}} \right)^2 \right] \qquad (2.19)$$

Where N is the number of measured ψ and Δ pairs, M is the number of fit parameters, σ_{ψ}^{exp} and σ_{Δ}^{exp} are the standard deviations of the experimental data points. From equation (2.19) it can be seen that noisy measurements with corresponding large deviations will not be strongly weighted in the fit.

2.7.1 Models for data evaluation

To extract material properties from the analysis of spectroscopic ellipsometric data it is very important to build a model which describes the optical response of the sample and have enough flexibility to accurately fit the experimental data.

Cauchy dispersion relation

For the parametrisation of the refractive index of transparent materials the Cauchy dispersion relation is:

$$n(\lambda) = A_n + \frac{B_n}{\lambda^2} + \frac{C_n}{\lambda^4} + \ldots \tag{2.20}$$

where A_n, B_n and C_n are constants which can be fit parameters.

Effective medium approximation

For the determination of porosity in the ILD films, which are a mixture of silicon oxide and air voids, effective medium approximation (EMA) models were employed. EMA models are the most appropriate tool to calculate the optical constants of heterogeneous materials which are mixture of constituents of different optical constants [31].

$$\frac{\tilde{\varepsilon} - \tilde{\varepsilon}_A}{\tilde{\varepsilon} + 2\tilde{\varepsilon}_A} = f_B \frac{\tilde{\varepsilon}_B - \tilde{\varepsilon}_A}{\tilde{\varepsilon}_B + \tilde{\varepsilon}_A} + f_C \frac{fd}{df} \tag{2.21}$$

where ε, ε_A, ε_B, ε_C..., are the (complex) dielectric functions of the effective medium, host medium and the inclusions of types B, C, ..., in the host, respectively, and where f_B, f_C, ..., represent volume fractions of material of types B, C, ..., in the total volume. The EMA layer provides a method to mix 2 or 3 sets of optical constants together. The usual interpretation of the EMA theory is that small particles of one material are suspended in a matrix of the host material. In practice, it is just a reasonable way to mix optical constants together.

2.8 References

1. P. S. Ho, J. Leu, W. W. Lee (Eds.) "Low Dielectric Constant Materials for IC Applications", (Springer- Verlag Berlin Heidelberg New York, (2003), chap 5
2. C. Kittel, "Inroduction to solid state physics, 6th edition", (John Wiley & Sons, New York, (1986), chap 13

3. R. G. Lerner and G. L. Triggs, Eds. (1981). Encyclopedia of physics, Addison-Wesley Reading, MA, p.769.
4. J. Rouquerol, D. Avnir, C. W. Fairbridge, D. H. Everett, J. H. Haynes, N.Pernicone, J. D. F. Ramsay, K. S. W. Sing, and K. K. Unger, Pure Appl.Chem. 66 (1994) 1739.
5. K. Maex, M.R. Baklanov, D. Shamiryan, F. Lacopi, S. H. Brongersma, Z. S. Yanovitskaya., J. Appl. Phy. Rev. 93 (2003) 8793
6. R. A. Donaton et. al., Proceedings of International Interconnects TechnologyConference (IITC), (2000), 93.
7. F. Iacopi, C. Zistl, C. Jehoul, Zs. Tokei, Q. T. Le, A. Das, C. Sullivan, G. Prokopowicz, D. Gronbeck, M. Gallagher, J. Calvert, K. Maex., Micro. Eng. 64 (2002) 351.
8. A. Grill, Diamond Relat. Mater. 10 (2001) 234.
9. H. Conrads, M.Schmidt, Plasma Source Sci. Technol. 9 (2000) 441.
10. M.A. Lieberman, A.L. Lichtenberg, "Principles of plasma discharges and materials processing", John Wiley and Sons, (1994).
11. S. M. Rossnagel, J. J. Cuomo, W. D. Westwood, "Handbook of plasma processing technology: fundamentals, etching, deposition, and surface interactions", Noyes Publications, (1989).
12. J. C. Vickerman, Surface Analysis – The Principal Techniques, J. Wiley and Sons, (1997).
13. T. S. Koopman, Physica, 1 (1934) 104.
14. Stöhr, J., "NEXAFS Spectroscopy". (1992), Berlin: Springer.
15. L. Ley, M. Cardona, Topics in Applied Physics Vol 27, Photoemission in Solids I and II, Springer-Verlag (1979).
16. E.W. Plummer, W. Eberhardt, Advances in Chem. Phys. 49 (1982) 533.

17. L. G. Parratt, Rev. Mod. Phys. 31 (1959) 616.

18. E. Tegeler, M. Iwan, E.-E. Koch, J. Elec. Spec. Related Phenom. 22 (1981) 297.

19. A. Kotani, S. Shin, Rev. Mod. Phys, 73 (2001) 203.

20. J. Nordgren, G. Bray, S. Cramm, R. Nyholm, J. E. Rubensson, N. Wassdahl, Synchrotron Radiation. Review of Scientific Instruments, 60 (1989) 1690.

21. J. Nordgren, and N. Wassdahl, J. Elec. Spec. Rel. Phen., 72 (1995) 273.

22. Y. Ma, N. Wassdahl, P. Skytt, J. Guo, J. Nordgren, P. D. Johnson, J-E. Rubensson, T. Boske, W. Eberhardt, and S. D. Kevan, Phys. Rev. Lett., 69 (1992) 2598.

23. J. A. Carlisle, E. L. Shirley, L. J. Terminello, J. J. Jia, T. A. Callcott, D. L. Ederer, R. C. C. Perera, F. J. Himpsel, Phys. Rev. B, 59 (1999) 7433.

24. J. A. Carlisle, S. R. Blankenship, R. N. Smith, Eric L. Shirley, L. J. Terminello, J. J. Jia, T. A. Callcott, D. L. Ederer., Spec. and Rel. Phen., 101 (1999) 839.

25. J. E. Downes, PhD Thesis, Boston University (2004)

26. N. Koch, D. Pop, R.L. Weber, N. Bowering, B. Winter, M. Wick, G.Leising, I.V. Hertel, W. Braun, Thin Solid Films 391 (2001) 81.

27. J.E. Downes, C. McGuinness, P.A. Glans, T. Learmonth, D. Fu, P. Sheridan, and K.E. Smith, Chem. Phys. Lett. 390 (2004) 203.

28. R. G. Wilson, F. A. Stevie, C. W. Magee, "Secondary Ion Mass Spectroscopy", John Wilwy & Sons, (1989)

29. J J. A. Woollam, "Encyclopedia of Electrical and Electronics Engineering", John Wiley and Sons, Inc. New York, NY, (2000).

30. J.A. Woollam, B. Johs, C.M. Herzinger, J.N. Hilfiker, R. Synowicki and C. Bun – SPIE Proceedings, CR72, (1999)

31. D.E. Aspnes and J.B. Theeten, Phys. Rev. B 20 (1979) 3292

Chapter 3: Chemical Characterisation Techniques and Etch Tools

3.1 Introduction

This chapter provides information on the experimental equipment and parameters used within the spectroscopic techniques and the software used. Descriptions of plasma etch mechanisms will also be included.

3.2 X-ray Photoelectron Spectroscopy (XPS)

X-ray photoelectron spectroscopy (XPS) analysis of the samples was carried out in a VG Microtech electron spectrometer at base pressures in the preparation and analysis chambers of $2x10^{-8}$ and $2x10^{-9}$ mbar, respectively. The photoelectrons were excited with an X-ray source using Mg K_α ($h\nu$ =1253.6 eV) and the pass energy of the analyser was 20 eV yielding a resolution of 1.2 eV. The elemental concentrations were calculated by an approach in which the transmission function of the analyser was taken into account [1] and the values of respective cross sections were taken from Scofield [2]. Depth profiling of samples was carried out by in situ sputtering using an argon ion gun which was operated at an energy of 1 keV and a sample current of 20 μA. A XR3E2 twin anode x-ray source from Thermo VG Scientific was used in all XPS measurements. The hemispherical electron energy analyser is schematically shown in figure 3.1. The excited electrons are focused through an electrostatic lens, and then passed through the hemispherical analyser. Only electrons of energy E_0 will pass through the hemispheres undeflected. E_0 is swept through the entire energy range under consideration to acquire a spectrum.

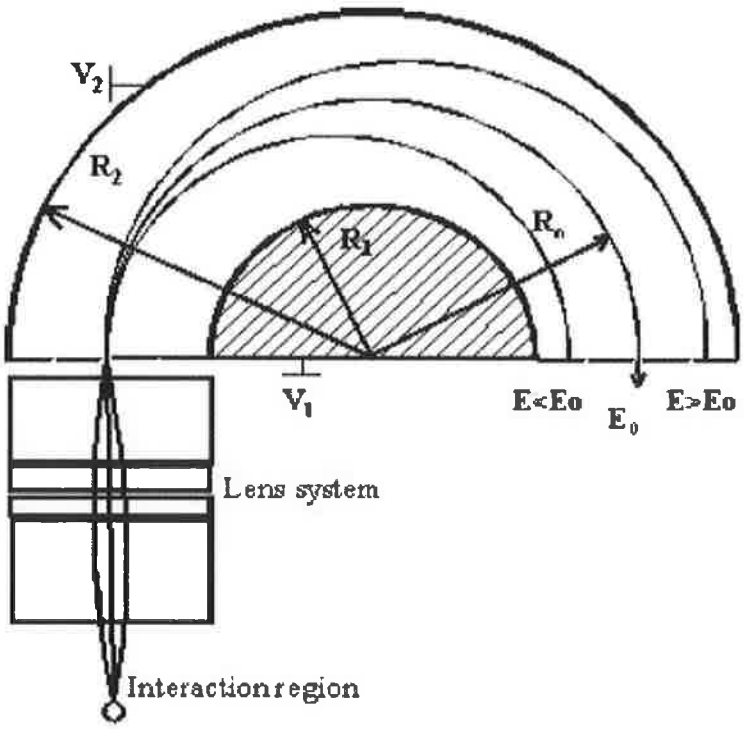

Figure 3.1: A hemispherical analyser. Electrons of energy E<E0 and E>E0 are deflected by the potential applied to the analyser walls [3].

The photoelectron current is amplified by an electron multiplier know as a channeltron. The multiplier amplifies the signal by accelerating the electrons through a potential difference of 3.5 KeV, causing the electrons to collide with the multiplier surface, releasing many more electrons in an electron cascade. The signal is then fed to a computer, which displays the number of counts as a function of electron kinetic energy.

3.2.1 Quantification

The complete XPS spectrum of a material contains peaks that can be associated with the various elements (except H and He) present in the outer 10 nm of that material. The area under these peaks is related to the amount of each element present. So by measuring the peak areas and correcting them for the appropriate instrumental factors, the percentage of each

element detected can be determined. The equation that is commonly used for these calculations is:

$$I_{ij} KT(KE) L_{ij}(\gamma) \sigma_{ij} \int n_i(z) e^{-z/\lambda(KE)\cos\theta} dz \qquad (3.1)$$

Where I_{ij} is the area of peak j from element i, K is an instrument constant, T (KE) is the transmission function of the analyzer, $L_{ij}(\gamma)$ is the angular asymmetry factor for orbital j of element i, σ_{ij} is the photo ionisation cross-section of the peak j from element i, $n_i(z)$ is the concentration of element i at a distance z below the surface, λ (KE) is the elastic mean free path length, and θ is the takeoff angle of the photoelectrons measured with respect to the surface normal.

A fitting program called WinSpec [4] was used to fit the XPS core level spectra for the experiments in the thesis. This program allowed the user to input multiple peaks of different types in addition to a choice of different backgrounds in order to fit the experimental data that may consist of several components. In all core levels examined in this thesis, the lineshapes were fitted with mixed singlet peaks which are a combination of Lorentzian and Gaussian type curves. This fitting procedure is a computational approximation of a Voigt lineshape, as there was no actual convolution of Lorentzian and Gaussian components carried out by the program. The program utilizes multiple iterations to reduce the difference between the XPS spectrum and the calculated fit of the spectrum.

3.2.2 Charging effects

Because the samples under consideration are insulators, they are slow to replace electrons that leave during the photoemission process, leaving the layer positively charged. This charging causes the spectrum to move to higher binding energy. Because of this effect,

all spectral peaks are referenced to the known binding energy of the surface C *1s* peak (285 eV) [5].

As many of the samples contained carbon on the surface which had different oxidation states, the C *1s* peak position was not always used. In this case a gold spot 1 mm in diameter was deposited in the centre of each sample in order to allow compensation for sample charging effects during the experiment. This was achieved by fixing the binding energy of Au $4f_{7/2}$ line at 84.0 eV as an energy reference.

3.3 Synchrotron Radiation (SR) Techniques

Soft X-ray measurements were taken on the X1B beamline at the National Synchrotron Light Source (NSLS) at Brookhaven National Laboratory, New York. In the synchrotron, electrons travel under UHV at high velocity in a circular path, 'steered' by a magnetic field. While moving at velocities near the speed of light, the electrons emit electromagnetic radiation tangential to their direction of travel. This broadband electromagnetic radiation is made available to individual beamlines tangential to the storage ring. A synchrotron is shown schematically in figure 3.2. [6] The vacuum in the chamber is maintained by a rotary-backed turbo-molecular pumps and ion pumps. All samples were loaded simultaneously to avoid having to break the vacuum, and to ensure identical experimental conditions for each sample. The organic semiconductors were grown in-situ in a prep chamber.

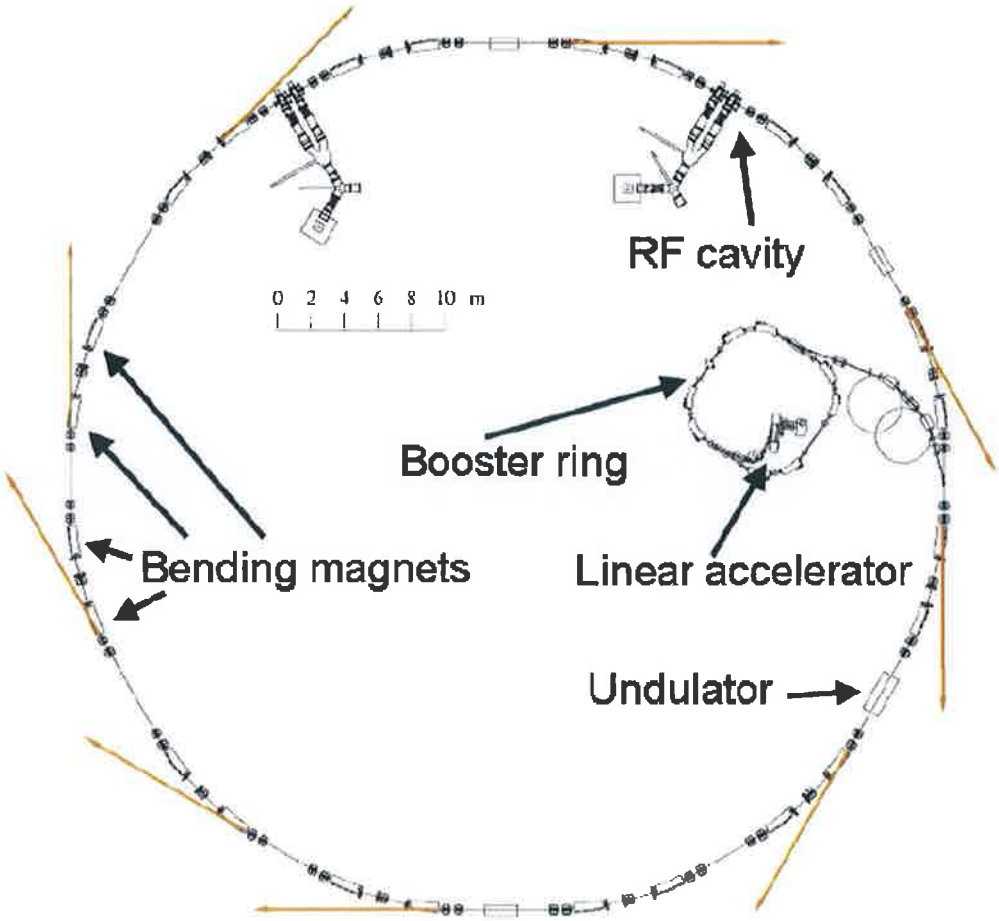

Figure 3.2: Schematic diagram of a synchrotron [6]

The main advantage of using synchrotron light is the broad spectral range of high intensity photon energies available which when coupled with a monochromator, enables very high resolution spectra to be acquired.

3.3.1 Bending magnets

A dipole magnet, in particle accelerators, is a magnet built to create a homogeneous magnetic field over a particular distance. Particle motion in that magnetic field will be circular in a plane perpendicular to the field and collinear to the direction of particle motion and free in the

direction orthogonal to it. Thus, a particle injected into a dipole magnet will travel on a circular or helical trajectory. By adding several dipole sections on the same plane, the bending radial effect of the beam increases.

3.3.2 Undulator

An undulator is an insertion device in a synchrotron storage ring. It consists of a periodic structure of dipole magnets as shown below in figure 3.3. The static magnetic field is alternating along the length of the undulator with a wavelength λ_u. Electrons crossing the periodic magnet structure are enforced to undergo oscillations and radiate. The radiation produced in an undulator is highly intense and concentrated in narrow energy bands in the spectrum. It is also collimated on the orbit plane of the electrons. Undulators can provide a flux several orders of magnitude higher than a simple bending magnet and as such are in high demand at synchrotron radiation facilities.

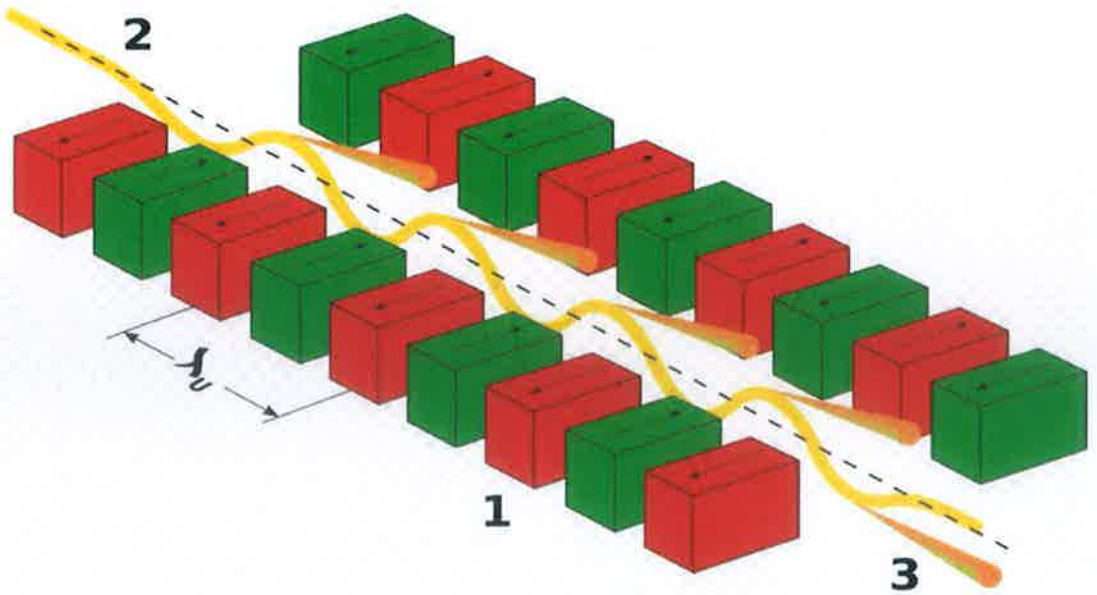

Figure 3.3: The working of the undulator. 1: magnets, 2: electron beam, 3: synchrotron radiation

An output spectra of the soft x-ray undulator at X1B for two different K values, where K is the deflection parameter are shown in Figure 3.4. The spectra illustrates the primary peaks with high intensity, also seen are second and third order peaks at higher energies for $K = 1.98$.

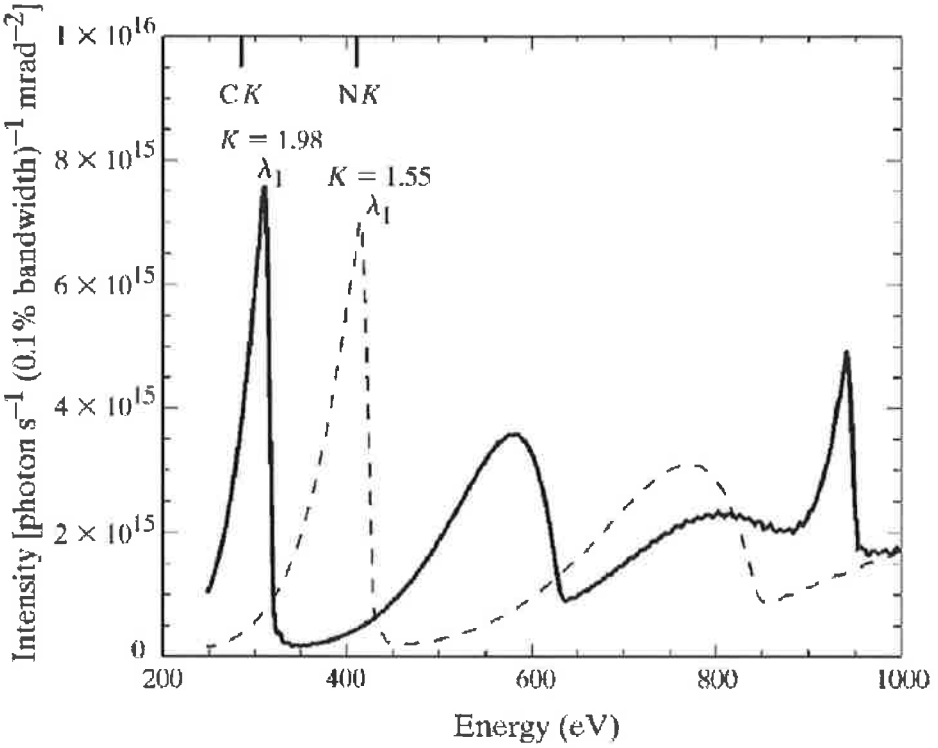

Figure 3.4: The output spectrum of the X1B undulator for two different K values [7].

3.4 X-ray Absorption Spectroscopy (XAS)

3.4.1 Total electron yield NEXAFS spectroscopy

Measurement of the soft x-ray absorption characteristics of materials requires a bright, tunable source of soft x-rays. Prior to the development of synchrotron radiation sources this was more or less impossible, as the intensity of broadband x-ray radiation, verses discrete atomic transitions, from conventional sources was far too weak to yield a usable absorption signal. However, with the advent of synchrotron sources and high resolving power beamline

monochromators, the measurement is now relatively simple to perform. All NEXAFS measurements presented in this thesis were performed using the total electron yield method. Figure 3.5 is a schematic diagram of the arrangement of the components used at the beamline X1B (NSLS).

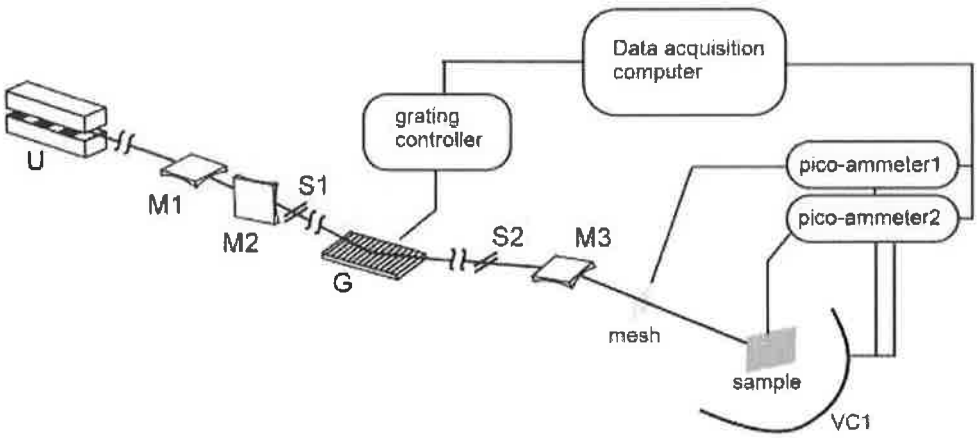

Figure 3.5: The arrangement of the components at X1B used to perform NEXAFS spectroscopic measurements [8].

The X1 undulator (U) provides a high brightness soft x-ray beam in the energy range of 250 - 1600 eV. This is focused onto the entrance slit (S1) by a pair of spherical mirrors (M1, M2). The light is diffracted by one of several interchangeable spherical gratings (G) and the photon energy of interest is selected by the exit slit (S2). The diverging monochromatic beam is focused through a gold mesh onto the sample by an elliptical mirror (M3). The sample and mesh drain currents are measured by pico-ammeters (Keithley 428 current amplifier plus NSLS voltage to frequency converter). For a full description of the optical setup of the monochromator see *Randell et al* [9]. The mesh current serves as a measure of the incident beam intensity and is used to remove any variations in the sample current that are a result of the instrument, rather than the electronic structure of the sample. The vacuum chamber wall (VC) serves as the return portion of the current loop. A computer is used to scan the incident

photon energy while recording the mesh and sample drain currents. A typical carbon *K*-edge NEXAFS spectrum and mesh current trace are presented as Figure 3.6. The mesh current trace contains two characteristic artifacts that are also present in the sample spectrum. These must be factored out to obtain a valid NEXAFS spectrum. The first is indicated by the appearance of two dips in the incident intensity at 284 eV and 291.4 eV [10, 11]. These are produced by contamination of the optical surfaces (mirrors and grating) of the beamline by materials that absorb in the energy range of interest. In this case the position and shape of the features points to graphitic carbon contamination. The second feature visible in the mesh trace is seen as a general decrease in intensity at higher photon energies above 296 eV in the figure 3.6. This is a result of the spectral shape of the undulator fundamental peak, as shown in Figure 3.4. The position of this feature can be adjusted by changing the undulator gap, so as to minimize its impact on the NEXAFS spectrum. The NEXAFS spectrum is normalized by dividing the sample signal by the mesh signal.

XAS spectra were recorded by the sample drain current technique to obtain the total electron yield. The energy resolution is approximately 0.2 eV at the carbon and nitrogen *K*-edges, and 0.3 eV at the oxygen *K*-edge. The excitation bandwidth for the RXES spectra was typically 0.5 eV, as a result the combined instrument resolution broaden the elastically scattered radiation. Each scan took approximately 10 minutes to acquire. Where damage studies have taken place the beam spot was exposed to the sample for the time greater than 1 hour unless otherwise specified. The photon energy would have been well above threshold.

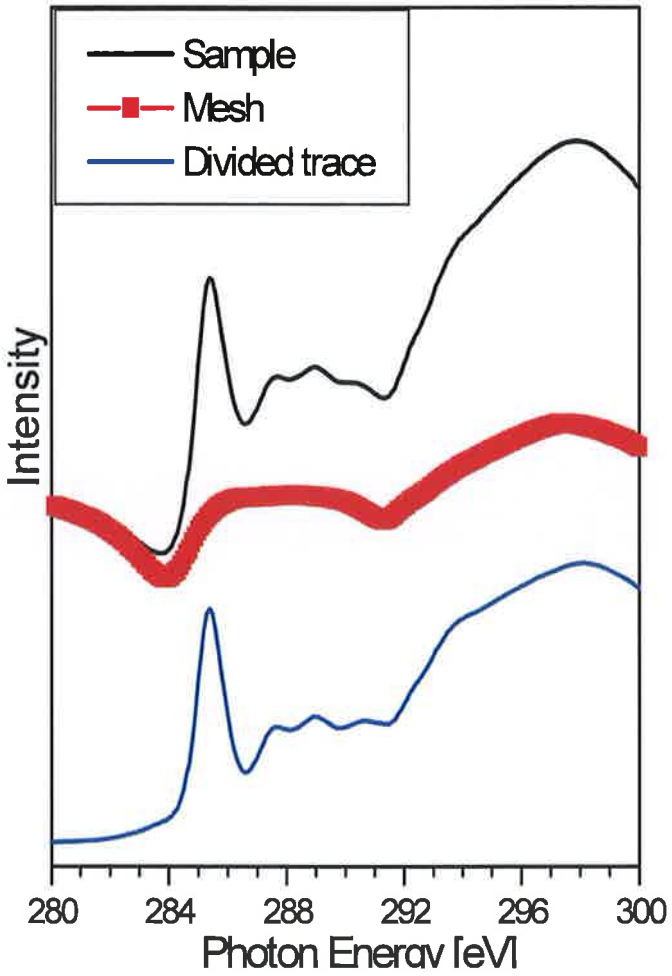

Figure 3.6: A typical C *K*-edge NEXAFS spectrum of TPP and associated mesh trace. The mesh trace is used to remove beamline generated artifacts from the spectrum.

3.5 X-ray Emission Spectroscopy (XES)

3.5.1 The XES300 soft x-ray emission spectrometer

The measurement of the characteristic spectrum of x-rays emitted by the radiative deexcitation of core-hole states has been used for many years as a tool to identify the elemental composition of samples under analysis. This is often referred to as 'energy dispersive analysis, x-ray' or EDAX. Most scanning electron microscope systems in operation today are fitted with a semiconductor calorimeter detector to make possible the measurement of the spectrum of x-rays emitted by a sample under electron bombardment. The resolution of these systems is

low, at best 20 eV, but is adequate to measure the intensity of emission of widely spaced core level transitions.

In order to get chemical or valence band electronic structure information from the spectrum of soft x-rays emitted necessitates at least a 100 fold increase in the resolution of the measurement system. This has been accomplished through the use of a optical spectrometer design, based on the dispersion of the soft x-rays by diffraction gratings [12]. The soft x-ray spectrometer used to make the measurements reported in this thesis was constructed by Gammadata (Sweden), modeled on a design optimized by the Nordgren group at Uppsala University, Sweden. The instrument is based on a Rowland circle configuration, and uses three spherical diffraction gratings to cover the energy range 50 - 1200 eV [13]. At soft x-ray energies, the normal incidence reflectivity of metals is significantly reduced and a grazing angle of incidence must be used to achieve usable grating efficiency.

A diagram of the interior apparatus of the mechanism is presented in Figure 3.7a. The x-rays are emitted by the sample and small fraction pass through the entrance slit of the spectrometer. This slit is roughly 20 mm wide and its apparent height can be varied between 0 and 120 microns through a rotation about the centre of the laterally displaced slit edges. This corresponds to a maximum angular acceptance of 0.5° vertically, and 5° in the horizontal direction. The x-rays that pass through the slit illuminate one of three diffraction gratings. The specific grating that is illuminated is determined by the position of a pair of metal 'grating selection' flags. The specifications of the three gratings installed in the instrument are given in the inset table of Figure 3.7. The x-ray detector is positioned tangentially on the Rowland circle, at the diffraction angle of interest.

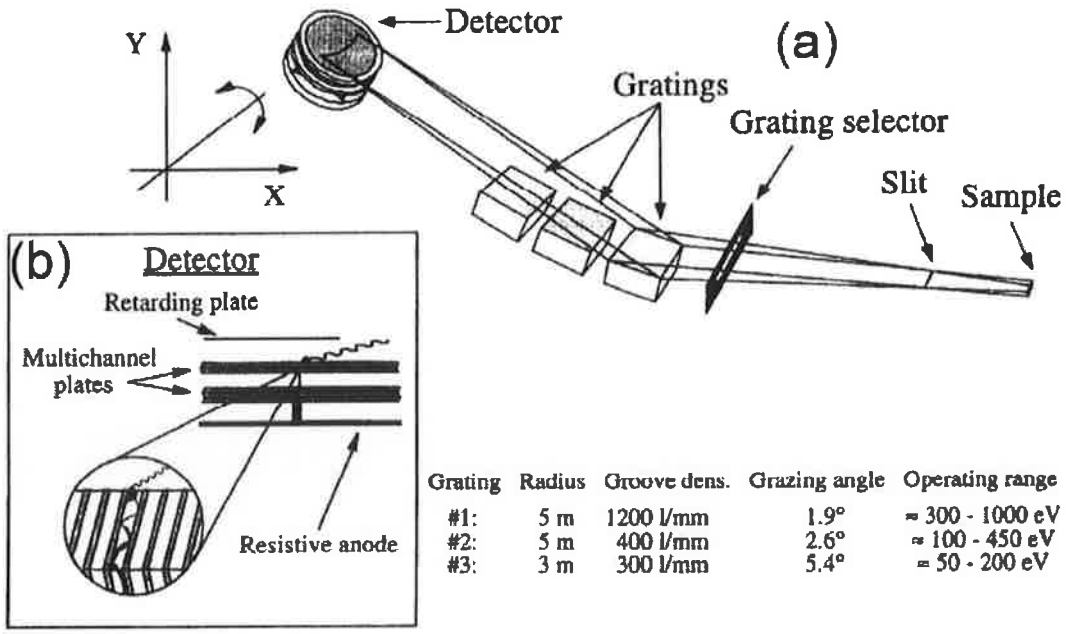

Figure 3.7: (a) A schematic diagram of the internal arrangement of optical components in the XES300 soft x-ray emission spectrometer. (b) Detail of the detector [13].

An expanded diagram of the detector is presented in Figure 3.7b. It consists of five micro-channel plate (MCP) area electron multipliers arranged in a two-plus-three stack. Each soft x-ray photon striking the top surface of the stack produces multiple secondary (low energy) electrons. The emission of these secondary electrons is improved by a thin layer of the salt cesium iodide (CsI) that is formed on the front surface of the MCP stack. Small numbers of these electrons enter the device, are amplified by a factor of roughly 10^8 by the MCP stack and emerge as a burst of electrons exiting the backside surface. Situated behind the rear surface of the MCP stack is a resistive anode encoder. This is used to quantify the position of an electron burst event, and thus the position the soft x-ray hits the detector face. The output is split into 1024 channels in the energy dispersing direction, and 32 `slices` across the detector. An illustrative detector image and spectrum are shown in Figure 3.8, higher energy x-rays are to the right.

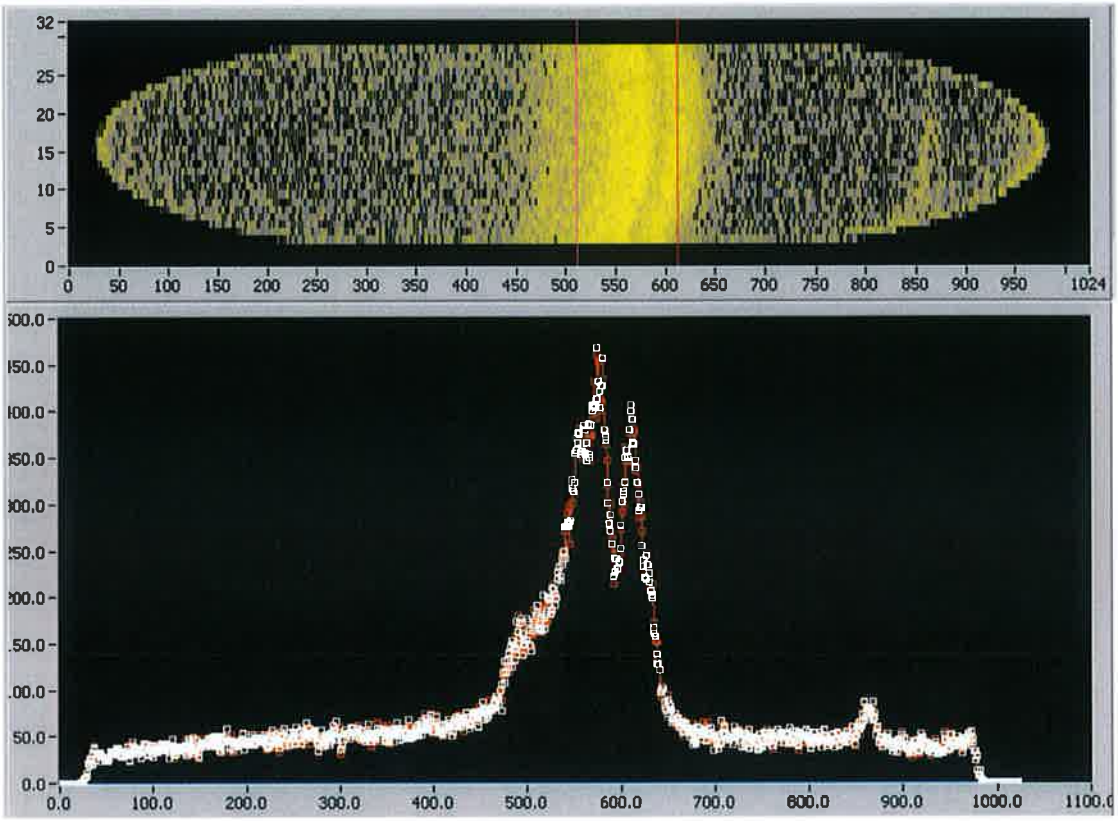

Figure 3.8: A typical image from the MCP detector (top) with 1024 channels in the energy dispersing direction, and 32 'slices' across the detector. The spectrum (bottom) is a result of a vertical summation, after the visible curvature to the spectral features has been corrected.

The curvature of the spectral features, visible in the detector image (top), is a result of the curved focus line of the spherical diffraction grating being imaged on a nominally flat detector. This is compensated for through numerical techniques before the detector image is summed in the vertical ('slice') direction to obtain the full x-ray spectrum.

The energy resolution for XES spectra presented in the thesis was approximately 0.4 eV near the carbon *K*-edge, 0.7 eV near the nitrogen *K*-edge and 0.9 eV near the oxygen *K*-edge. The energy scale of the C *K*-edge spectra was calibrated with 3rd order Ni L_α / L_β metal emission, the N *K*-edge spectra were calibrated via 2nd order Co L_α / L_β emission and the O *K*-edge spectra via 2nd order Zn L_α / L_β emission.

3.6 Secondary Ion Mass Spectroscopy (SIMS)

Secondary ion mass spectroscopy (SIMS) analysis of insulators has a wide range of applications in the analysis of materials used in semiconductor device fabrication. But surface charging of an insulating sample due to the incident charged ion beam can make SIMS analysis impossible. Two methods may be used to prevent surface charging; neutralisation with a low energy electron beam or replacement of the primary ion beam by a fast atom beam. The HAL IFG200 Ion/Fast atom gun from Hiden Analytical is designed for SIMS analysis of insulators. The IFG200 can be used as an ion gun or a fast atom beam (FAB) gun. The incident beam used in this study was a neutral Ar beam generated in a charge neutralisation chamber in order to avoid sample charging. When operated as a FAB gun, neutral argon gas molecules in the charge exchange cell are accelerated by a collision process to generate a high energy atom beam. The remaining ions are deflected away from the exit orifice and do not emerge from the gun.

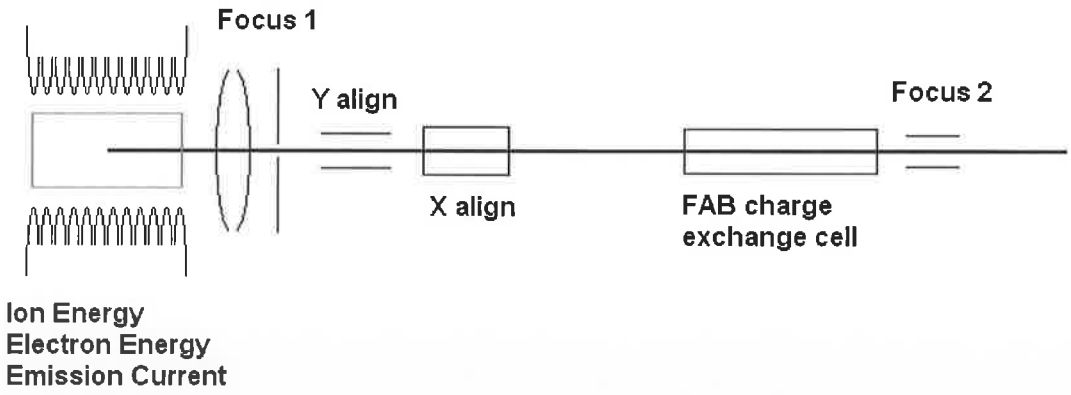

Figure 3.9: IFG200 Schematic diagram [14]

3.7 Plasma Etch Tools

Radio frequency power driven plasma sources have been extensively used within the microelectronics industry, where they are used for etching, deposition, sputtering and other surface treatments. Within these discharges, both the ion energy bombarding the electrodes and the ion flux current onto the electrodes are of extreme importance. High-density plasmas are required for high etch rate and therefore high throughput. The energy of the ions bombarding the electrodes is known to play an important role in thin film etching and sputtering processes. Traditionally, these devices have been operated with a single frequency power source, usually at 13.56 MHz. With a single power source, increasing the power increases the current and voltage simultaneously, resulting in increased plasma density and ion energy, respectively. In recent years, there has been an introduction of plasma systems which are operated at the sum of two frequencies. One of the frequencies is much higher than the second. The high frequency controls plasma density, and the low frequency controls the ion-bombarding energy. The basic idea of this is that the user can now control the plasma density and ion energy independently.

3.7.1 Lam 9100

The Lam9100 is a prototype plasma etch system that allows more control over the plasma parameters than previous etch systems. The 9100 etch tool is schematically shown below in figure 3.10. The transformer coupled plasma (TCP) source is a sinusoidal coil powered with a operating frequency of a 13.56MHz, while the capacitively coupled plasma (CCP) source operates at 4MHz; each of them has typical RF power ranging from 600-1200W (*upper power*) and 200-600W (*lower power*) respectively. Changing the CCP power setting affects the energy with which electrons and ions strike the wafer surface. These energies are of the order of tens of eV.

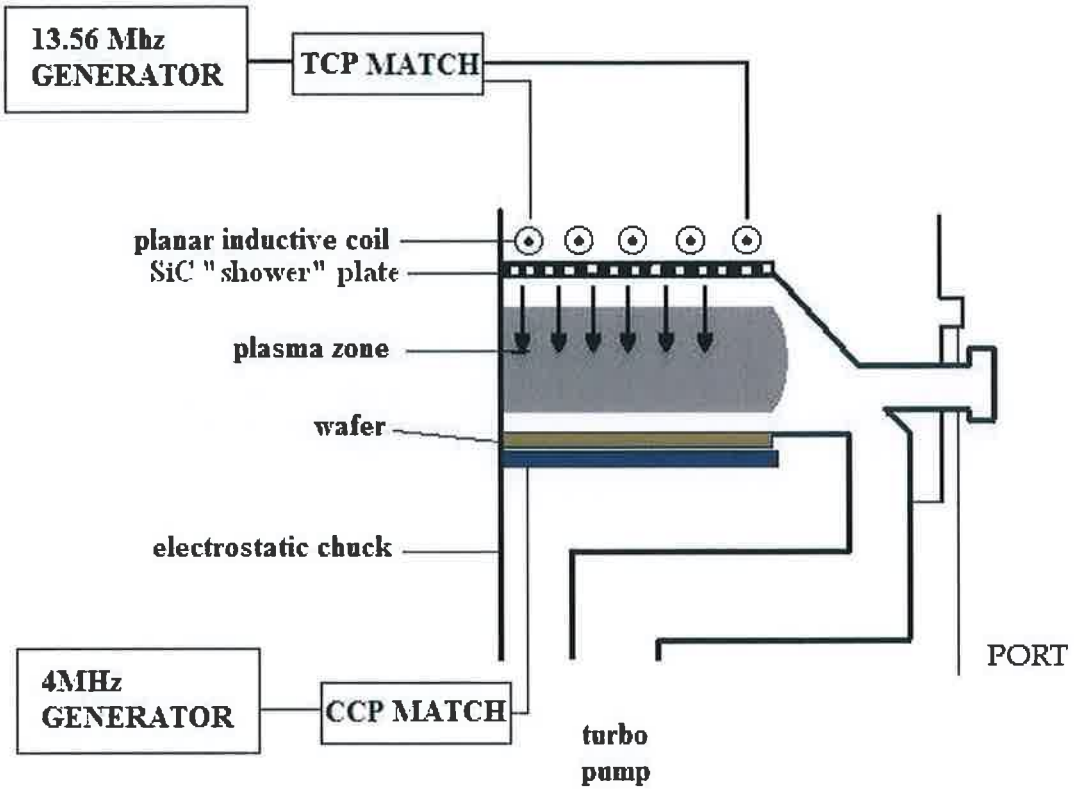

Figure 3.10: Lam9100 dual-frequency plasma-tool

The reason for having a dual frequency reactor is that having only one frequency it wouldn't be possible to control both the density of the ion flux (current) impinging on the wafer surface and the ions energy. At the pressures used in these etchers (ranging from15 mbar up to 45 mbar) it wouldn't be possible to create a dense plasma by other methods. TCP plasma sources give an ionisation fraction 100 times greater than ordinary sources.

3.7.2 Lam Exelan

The Exelan plasma etcher is schematically shown in figure 3.11. The Exelans chamber is designed to use this 'dual frequency confined capacitive coupled plasma' technology (DFC(^{TM})-CCP) to generate the etching plasma. The power is coupled to the gas mixture via a

capacitor with one electrode powered by a radio frequency (RF) voltage of 27.12 MHz (the first harmonic of the fundamental frequency 13.56 MHz) and the other at 2 MHz. The substrate is placed on the wafer plate where ions are accelerated through the sheet and impact the substrate only at an angle perpendicular to the surface thus producing an anisotropic etch i.e. trench walls are normally vertical.

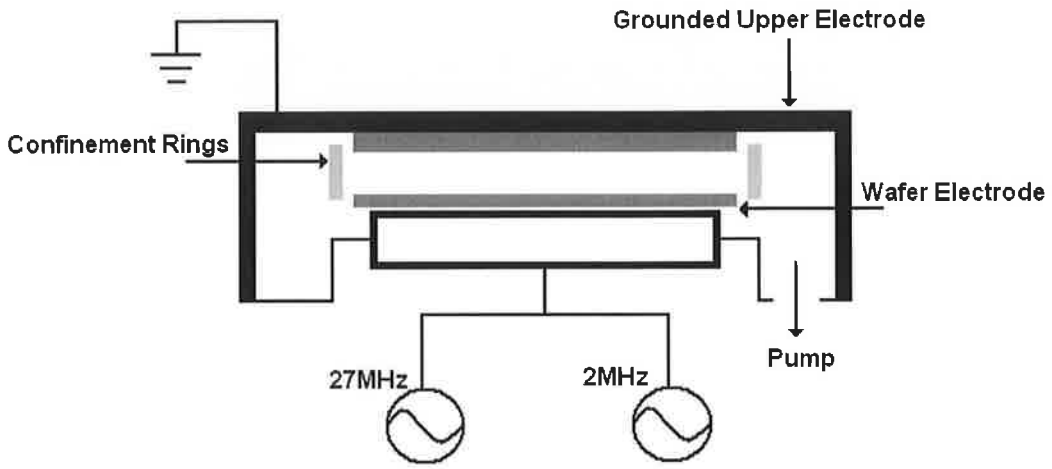

Figure 3.11: Lam Exelan dual-frequency plasma-tool

3.8 Evaporators

Organic Evaporator (Boston Uuniversity)

Thin film organic semiconductor samples were grown *in-situ* in a custom designed ultra high vacuum multi-source organic molecular beam deposition (OMBD) system attached to the main spectrometer chamber. This system allows a substrate to be cleaned and thin films to be deposited by evaporation in background pressures of approximately 2 x 10^{-9} mbar. The samples can then be transferred directly into the measurement system under UHV conditions. In the case of TPP this is particularly important if the intrinsic properties of the material are to

be measured, as it has been shown that thin film samples can be strongly *p*-type doped due to oxygen contamination when grown in poor vacuum conditions [15]. The samples used in this experiment were deposited on *p*-type Si (100) substrates. The substrates were ultrasonically cleaned for 10 minutes in acetone before being introducted into the OMBD system, where they were heated to 900 °C for 10 minutes in a background pressure of 8 x 10^{-9} mbar. The organic sources were out-gassed for 4 hours, at a temperature slightly below their respective evaporation temperatures, until the system pressure returned to 2 x 10^{-9} mbar. Film deposition was monitored using a quartz microbalance. A typical deposition rate of approximately 30 Å/min was used for all the materials, and in each case a total of approximately 2000 Å material was deposited.

Organic Evaporator (Dublin City University)

Thin film organic semiconductor samples were grown *in-situ* in a ultra high vacuum system on the main spectrometer chamber. The layout of the organic evaporator is presented in figure 3.12. The low temperature molecular evaporator manufactured by Kurt J. Lesker consists of a boron nitride liner resistively heated by tungsten wires. A thermocouple in contact with the base of the liner allows for an accurate measure of the temperature and functions as a feedback mechanism for the evaporator controller, allowing for the accurate setting and maintaining of the temperature to an accuracy of $\pm$0.2K, in addition to a controllable temperature ramp rate. The tungsten heating coils are wrapped around the ceramic liner with the inter-coil distance reducing closer to the top of the ceramic. This results in an increased temperature at the top of the ceramic ensuring evaporated organics doesn't redeposit to the ceramic once evaporated from the base of the crucible. A shutter, placed in front of the crucible, is used for more accurate control of the deposition rate of the organic material.

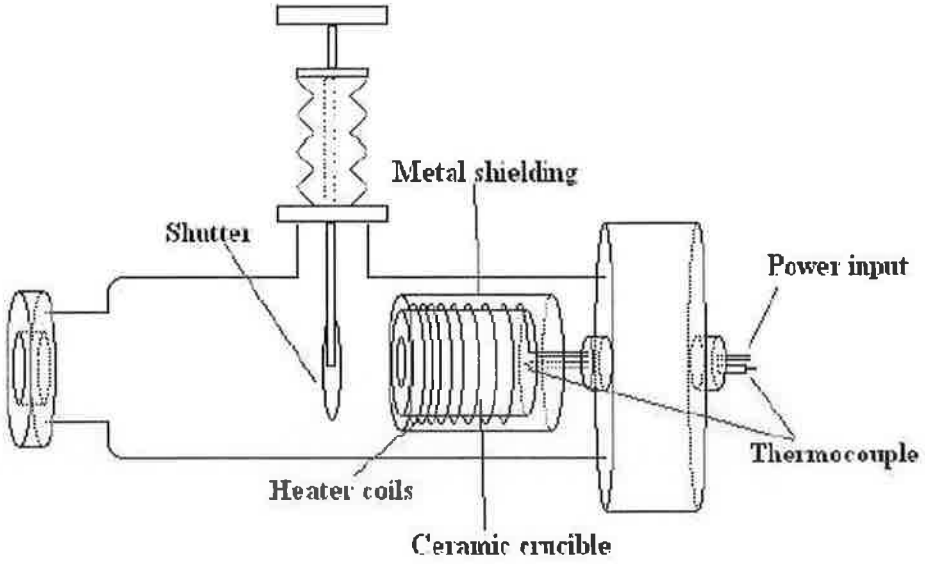

Figure 3.12: Schematic diagram of the organic evaporator used in DCU

3.9 References

1. L.T. Weng, G. Vereecke, M.G. Ganet, P.G. Rouxhet, J.H. Stone- Masui, P. Bertrand, W.E.E. Stone, Surf. Interf. Anal. 20 (1993) 179.
2. J.H. Scofield, J. Electron. Spectrosc. Relat. Phenom. 8 (1976) 129.
3. http://es1.ph.man.ac.uk/research/facilities/HDA.html (2002)
4. Winspec ver 2.08, Laboratoire Interdisciplinaire de Spectroscopie Electronique, Facultes Universitaires Notre-Dame de la Paix, Belgium.
5. S. R. Kaluri, and D. W. Hess, Appl. Phys. Lett. 69 (1996) 1053
6. Proposed design of the Boomerang synchrotron in Melbourne, Australia.
7. B. Winn, H. Ade, C. Buckley, M. Feser, M. Howells, S. Hulbert, C. Jacobsen, K. Kaznacheyev, J. Kirz, A. Osanna, J. Maser, I. McNulty, J. Miao, T. Oversluizen, S. Spector, B. Sullivan, S. Wang, S. Wirick and H. Zhang, J. of Synchrotron Radiation. 7 (2000) 395

8. J. E. Downes, PhD Thesis, Boston University (2004)
9. K. J. Randall, J. Feldhaus, W. Erlebach, A. M. Bradshaw, W. Eberhardt Z. Xu, Y. Ma, and P. D. Johnson, Rev. Sci. Instrum. 63 (1992) 1367
10. J. Stöhr, R. Jaeger, Phys. Rev. B 26 (1982) 4111.
11. S. Lopez, H. M. Dunlop, M. Benmalek, G. Tourillon, M.-S. Wong, and W. D. Sproul, Surf. Interface Anal. 25, 827 (1997)
12. H.A Rowland, Philosophical Magazine, 13 (1882) 469.
13. J. Nordgren, and R. Nyholm, Nuclear Instruments and Methods A, 246 (1986) 242.
14. Hiden Analyical Manual for the IFG200.
15. Q. Zhou, and R.D. Gould, Thin Solid Films, 317 (1998) 432-5.

Chapter 4: Soft x-ray studies of ULK CDO layers and fluorocarbon films.

4.1 Introduction

This chapter introduces two of the main materials investigated in this thesis. The first is an ultra low-*k* (ULK) carbon doped oxide (CDO) material used as the insulator between interconnects of microprocessors. The second is a by-product of fluorocarbon etching which results in thin fluorocarbon film being formed on the surface of etched material.

There is increasing interest in low-*k* materials due to the RC time delay. One way of solving the capacitance problem is to lower the dielectric constant *k* of the material in the interlayer dielectric (ILD) by using ULK materials. CDO is a ULK candidate material as its *k* value is less than 2.5 and it is broadly compatible with current integration processes. In the CDO material, some of the Si-O bonds are replaced by Si-CH_3 bonds. This results in the formation of less polar bonding which should reduce the dielectric constant of the material. However a much more significant contribution to the low k-value that these materials exhibit can be attributed to the formation of a nano-porous structure. These changes to the structure and chemical composition of the ILD material alter the electrical performance and pose significant challenges to the integration of low-*k* materials in device fabrication.

Plasma-polymerized fluorocarbon films (CFx) have been of interest for many years now with many different applications such as low-*k* dielectric layers [1], passivation layers for the prevention of carbon depletion in carbon doped oxides [2,3,4] and for the improvement of hole injection from metal into organic films[5]. Fluorocarbon plasmas are known to result in the deposition of a polymeric film covering the surface during etching of the substrate material. Despite the fact that fluorocarbon films are widely encountered in processing semiconductors, detailed spectroscopic studies of chemical composition and electronic structure of fluorocarbon layers are lacking.

This study aims to determine the electronic structure of CDO layers to assist in developing a comprehensive understanding of the electrical properties of these materials. The

results from a study of the chemical composition and electronic structure of ULK CDO and fluorocarbon layers using a variety of synchrotron radiation soft x-ray spectroscopies will be presented. The techniques used were soft x-ray emission spectroscopy (XES), soft x-ray absorption spectroscopy (XAS), and conventional x-ray photoemission spectroscopy (XPS). The element specific valence and conduction band electronic structure for the carbon and oxygen atoms of the CDO was measured using XES and XAS, respectively. Core level photoemission spectra were measured using XPS for all elements in the materials under investigation. This study also shows the damage induced in the thin film fluorocarbon layers when exposed to intense undulator beamline synchrotron radiation.

4.2 Electronic structure characterisation of Ultra Low-*k* (ULK) Carbon Doped Oxide (CDO) using soft X-ray emission spectroscopy.

Presented in Figure 4.1 is a schematic drawing of the CDO structure. The material is chemically modified SiO_2 in that some of the Si-O bonds have been replaced by Si-CH_3 bonds. The material forms a porous structure with the magnitude of the dielectric constant directly related to the percentage porous structure in the material [6]. No oxygen is directly bonded to the carbon atoms in the structure. XPS was used to determine that the chemical composition of the CDO film in atomic percentage (31% Si, 15% C and 54% O) which indicates that the carbon substitutes for the oxygen in the silicate structure. H atoms have not been counted in these percentages.

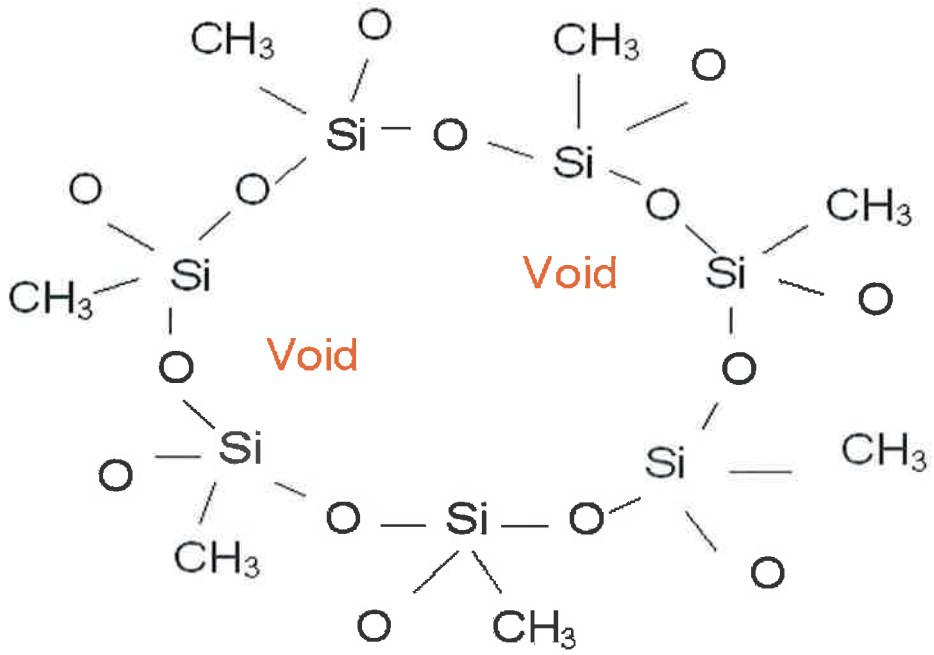

Figure 4.1: A schematic drawing of the CDO structure

Figure 4.2 shows a comparison between the O *K* absorption edge of ULK CDO and conventional SiO_2. The similarities between the spectra confirm that the oxygen resides in the same chemical environments in both materials in agreement with the above CDO structure.

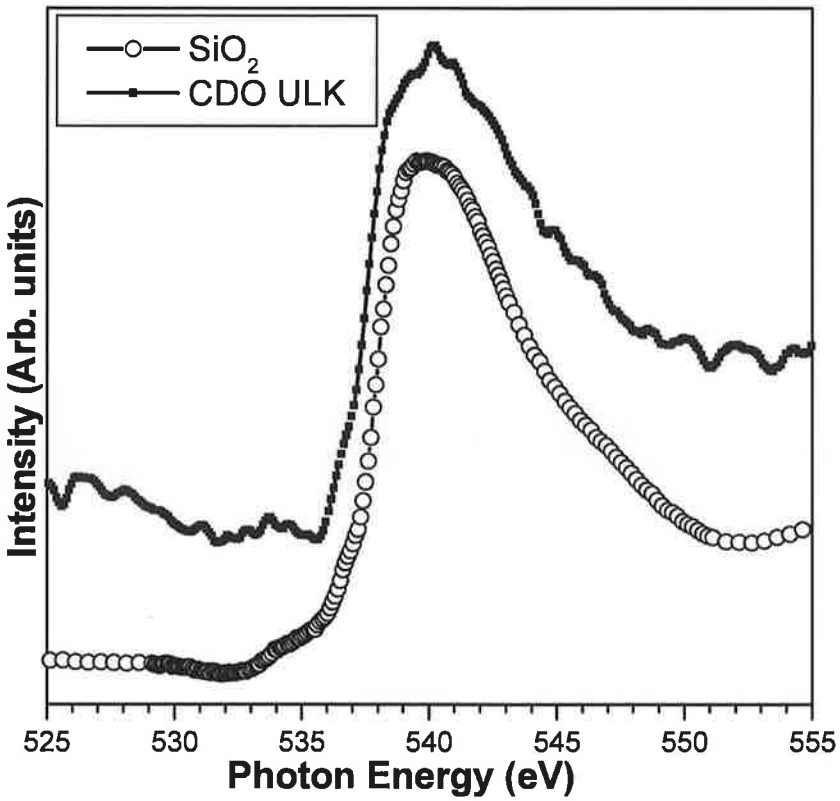

Figure 4.2: The O *K* edge XAS spectra of ULK CDO compared with that of SiO_2

Shown in Figure 4.3 are the carbon K_α soft x-ray emission spectroscopy (XES) spectra reflecting the C *2p* PDOS from both a stationary and continuously translated ULK CDO sample. The excitation energy was 296 eV, which is well above the absorption threshold for the C *1s* states. The peak at 296 eV which is visible in both spectra and is caused by the elastically scattered excitation light. Significant differences in the measured electronic structure of identical films in the 270 eV to 285 eV spectra region are clearly visible depending on whether the sample is stationary or continuously translated during the measurement period. This effect of beam damage influencing the measured spectrum has been previously reported [7,8]. A low energy subband feature is located at 263 eV is observed in the spectrum from both the translated and stationary samples. This low energy subband is in a

similar spectral position to that reported by Kurmaev et al. [9,10,11] in polyimide (PI) and polyethersulphone (PES) films. They argued that a feature at this energy is carbon related and is due to hybridisation of C *2p* states with O *2p* and S *3s* states [10]. Note that the overall shape of the low energy subband is unaffected by the beam damage to the sample.

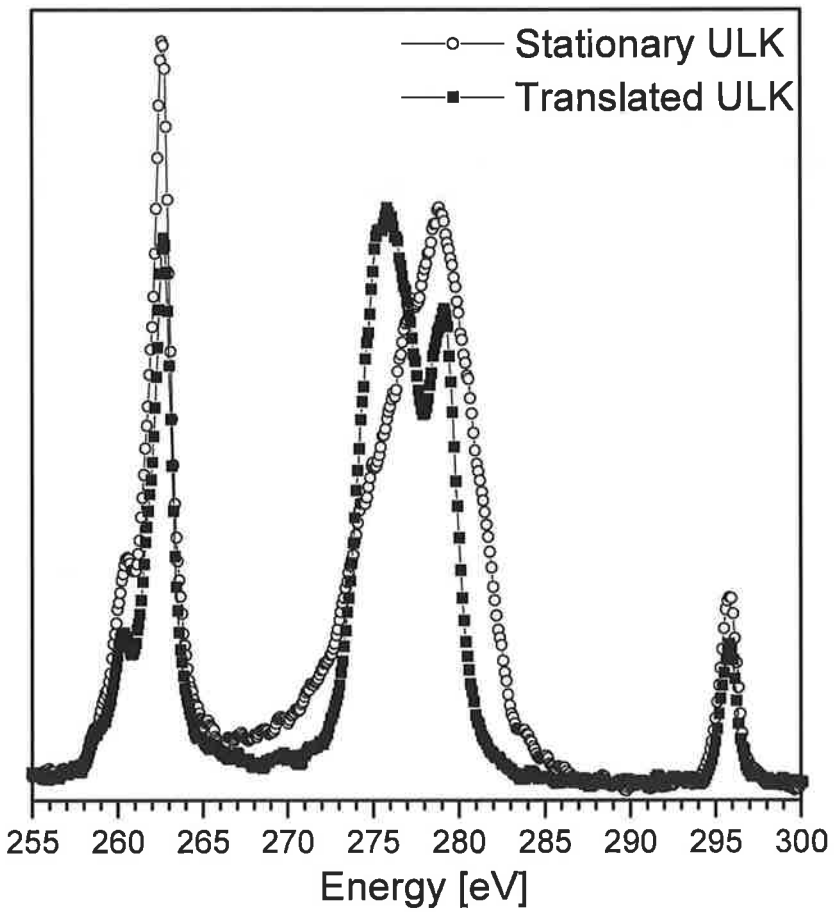

Figure 4.3: The C K_α XES spectra of translated and untranslated CDO samples at an excitation energy of 296 eV.

The structure of the inelastic scattering contribution feature in the 270 eV to 285 eV range for the sample which is continuously translated during measurement shows two distinct features at 275.8 eV and 279 eV. The relative intensity of these spectral features inverts for the static

sample and this is attributed to radiation induced damage at one point in the sample. Previous C *1s* XES studies of both polyimide and carbon nitride (CN_x) [9,10,11,12] films have reported similar spectra features to those observed in the translated sample. The main peak at 275.8 eV is attributed to both σ and π states with σ states predominating, while the higher energy peak at 279 eV has been attributed to π -type states. The proposed CDO structure outlined above would not be expected to have π bonded carbon atoms as the structure only contains carbon σ bonds [13] However, a recent x-ray absorption study of orthosilicate glass (OSG) material which has similar composition and structure to the CDO films has reported that as a function of aging, a π bonded signal appears and is attributed to the breakdown of the Si-CH_3 bonding structure in the OSG as a function of time leading to the formation of graphitic C=C bonds [13]. This is consistent with our observations of the changes induced in the relative intensities of the two spectral features with radiation damage in that the graphitic carbon π bonded signal increases while the σ bonding related to the Si-CH_3 bonds significantly diminishes. All subsequent XES spectra shown in this thesis are for samples continuously translated during measurement to minimise radiation-induced damage.

Figure 4.4 shows the C K_α RXES spectra for a range of excitation energies. The spectra consists of three main features which are due to the elastic peak (high energy peak) with a position equal to the excitation energy, an inelastic scattering contribution (middle peak) and a third peak which is a O K_α XES spectrum observed in 2nd order. Spectrum (i) corresponds to the translated spectrum shown in figure 4.3. Spectra (ii), (iii) and (iv) correspond to RXES spectra taken at 287.2 eV, 286.7 eV and 285.7 eV, respectively. What can be clearly observed is the expected shift in the energy position of the elastic peak and the reduction in the intensity of the main spectra feature in the 270 eV to 285 eV range as the excitation energy is reduced towards the C *1s* threshold excitation energy. The fact that the spectral feature at 262.5 eV remains unaltered as the excitation energy is reduced suggests that the origin of this feature

cannot be C *1s* related. This is confirmed by spectrum (v) in figure 4.4 which is acquired at an excitation of 280.5 eV which is well below the absorption edge of the C *1s* (285 eV).

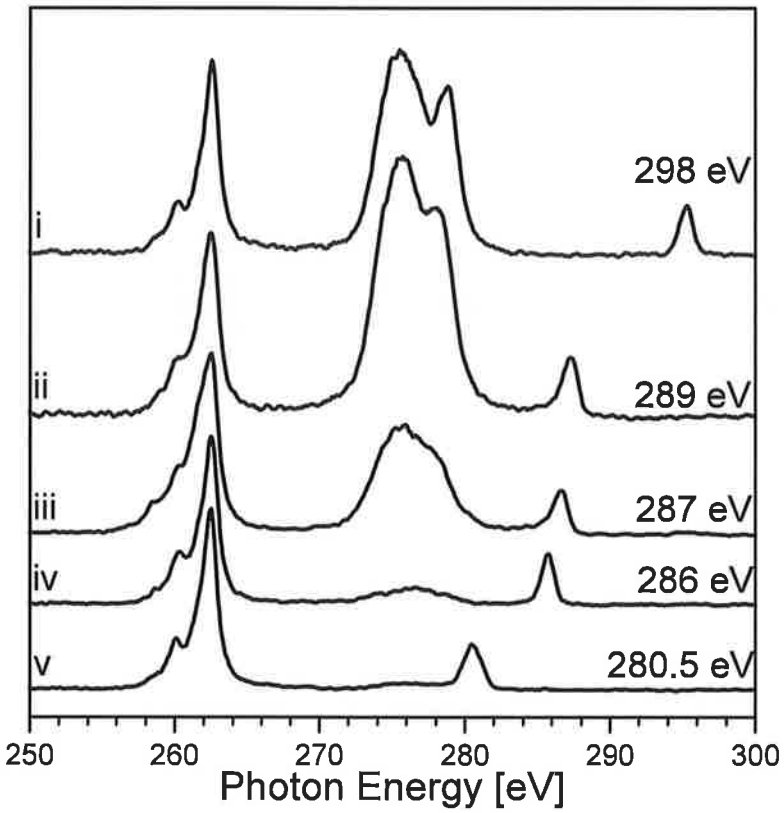

Figure 4.4: A series of C K_α RXES spectra from CDO acquired at 298 eV, 289 eV, 287 eV, 286 eV and 280.5 eV for (i) to (v) respectively.

In the investigations to determining the origin of this feature, it was noticed that a strong similarity between the overall structure of this subband and the resonant X-ray emission of O K_α spectra of CDO film shown in figure 4.5. The O K_α spectra were obtained in 1st order with a 5m radius of curvature grating with 1200 lines/mm groove density and an entrance slit of 10μm giving a instrument resolution of 0.4eV. The O K_α XES spectrum reflects transitions of O 2*p* electrons from the valence band to holes created on the O *1s* level, and thus measures the

O *2p* valence band PDOS. The spectra closely resemble previously published XES data for oxygen bonded to silicon [14].

Spectra (i) and (ii) in figure 4.5 for the static and translated spectra, respectively, have excitation energies of 556.7 eV which is above the absorption threshold, Spectrum (iii) of figure 4.5 has an excitation energy of 542 eV which is in resonance with the absorption edge. The main spectral features are positioned at 525.9 eV, 521.4 eV and 518 eV. There is no discernable difference between the O K_α spectrum acquired during continuous translation or when static which is similar to the behaviour of the low-energy subband in the C K_α spectrum. In fact, when the low energy subband of figure 4.4 is compared to the oxygen spectra shown in figure 4.5 one can see an identical 3 peak structure. In figure 4.4, the main feature of the low energy subband is at 262.5 eV. It has 2 side peaks at lower energy of 260.25 eV and 258.5 eV. The second order light for spectra (i) to (v) in figure 4.4 would be in the range 561 eV to 590 eV which is well above the absorption threshold of oxygen. The second order features can be seen in Figure 3.4 which shows the output spectrum of the X1B undulator. The fact that the energy separation of the individual spectral features in the subband in figure 4.4 (2.25 and 1.75 eV) is exactly half the separation measured in figure 4.5 (4.5 eV and 3.5 eV) is confirmation that the subband (inset in figure 4.5) is a second order O K_α related feature. Small differences in the spectra may be due to a variation in the collection time leading to peaks being less well resolved.

We can therefore conclude that the subband seen in the C K_α spectra is due to oxygen being excited by second order light and is not related to the hybridisation of carbon *2p* states. Undulator beamlines have significant second order light throughput which would explain this emission. Specifically spherical grating monochromators in 2θ mode have significant 2^{nd} order light.

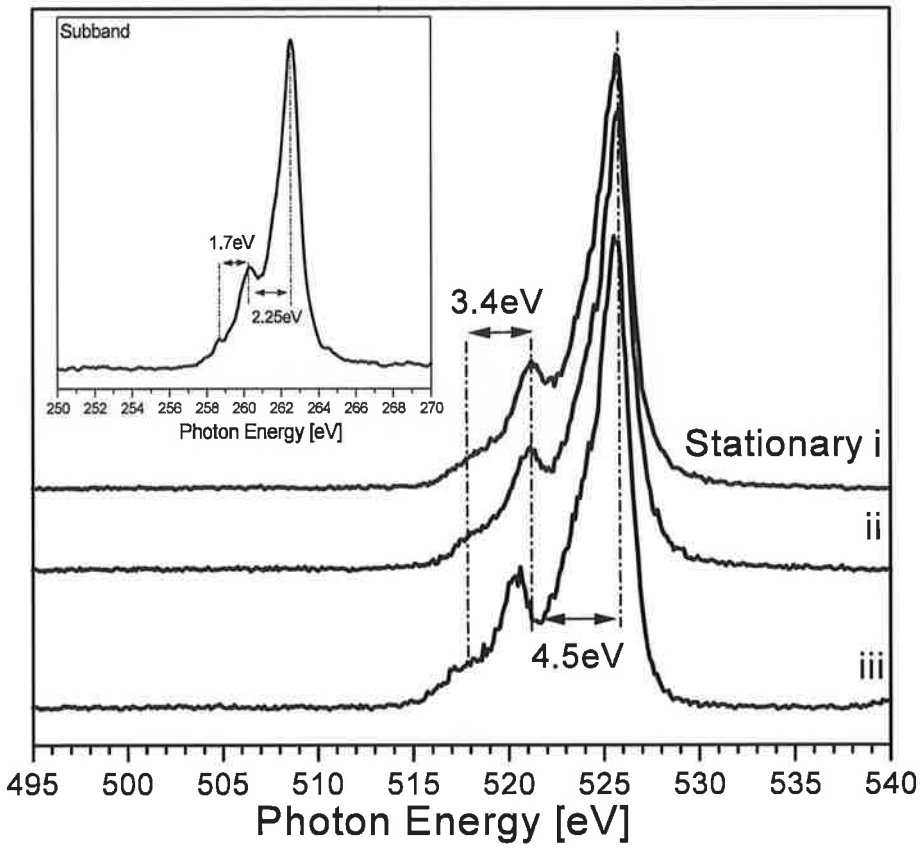

Figure 4.5: A series of O K_α RXES spectra from CDO acquired at 558 eV for (i, ii) and 541 eV for spectra (iii). Inset shows the subband from the C K_α spectra for comparison.

4.3 Electronic structure of fluorocarbon films deposited on silicon determined by soft x-ray emission.

Table 4.1 shows the plasma conditions and etch chemistries using $C_4F_8/O_2/Ar$ based chemistry to create the fluorocarbon polymeric film on the surface of bare Si. The influence of varying the O_2 gas flows on the surface chemical composition and hence the electronic structure was

determined with both the ion density (HF) and ion energy (LF) powers set at 200W. The gas flow was measured by the Standard Cubic Centimeters per Minute (SCCM) unit.

	HF Power [W]	**LF Power [W]**	**O_2 flow [sccm]**	**C_4F_8 [sccm]**	**Ar [sccm]**	**Pressure [mbar]**	**Time [s]**
S1	200	200	0	10	500	130	15
S2	200	200	6.6	10	500	130	15

Table 4.1: Processing parameter for forming fluorocarbon films on Si substrate

Figure 4.6 presents the C *1s* core level structure as measured by XPS using a Mg K_α radiation source. Spectrum S1 illustrates a typical carbon *1s* core level profile of a thick fluorocarbon polymeric film deposited on the surface of Si which has no oxygen flow in the plasma gas mix. The carbon lineshape has 5 peaks which are C-Si at 283.7 eV, C-C at 285.5 eV and C-Fx (x = 1,2,3) at 287.6 eV, 289.9 eV and 292.2 eV, respectively. These peak positions are consistent with previous XPS studies of fluorocarbon film composition [15]. The full width half max (FWHM) is 2.2 eV for each of the oxidation states, this parameter will be kept constant when fitting other fluorocarbons throughout the thesis. The spectrum S2 (open circles) shows the C *1s* profile of a fluorocarbon film that was formed under identical experimental conditions when the plasma feed gases contain 6.6 sccms oxygen. It has been shown in previous studies [2, 4] of fluorocarbon films that the addition of oxygen into the plasma gas chemistry reduces both the film thickness and the intensity of the high fluorocarbon oxidation states. From figure 4.6 a large increases in the number of C-C bonds is clearly visible, while a reduction in the intensity of the fluorocarbon oxidation state features is also apparent.

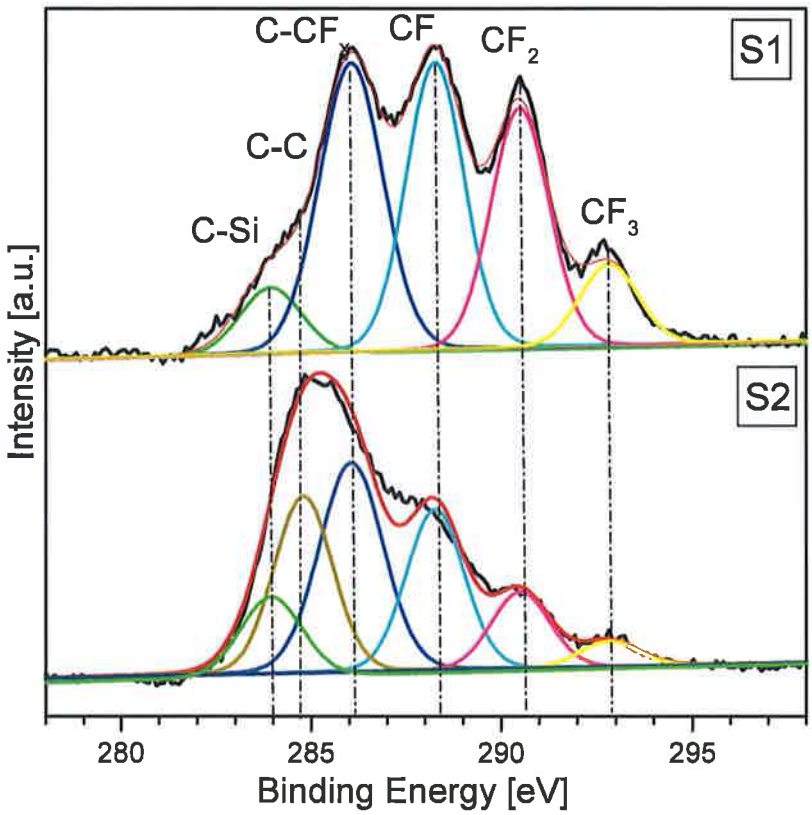

Figure 4.6: The C *1s* XPS spectra of a steady state CF_x layer on Si. S1 has no oxygen in the plasma while S2 has 6.6 sccms of oxygen.

Table 4.2 shows the energy positions of the oxidation states of the C *1s* XPS peak and the total concentration of each element. It is clear from table 4.2 that there is much more fluorine in sample 1 compared to that of sample 2. Sample 2 shows that there is a peak at 284.8 eV which corresponds to a C-C type bonding which is significantly more intense than the corresponding peak in sample 1 as most of the C is bonded to a C with fluorine as its nearest neighbour. By looking at the silicon ratio of intensities it is clear that S1 is thicker as the Si signal from the substrate is suppressed by the overlying film.

Peak	Position (eV)	S1 Composition (%)	S2 Composition (%)
C-Si	284	8.4	9.7
C-C	284.8		23.9
C-CF	286	31.5	31.1
CF	288.3	28.4	21.7
CF_2	290.5	23.8	10.4
CF_3	292.8	8.0	3.4
Carbon		34.2	43.2
Fluorine		55.4	33.9
Oxygen		4.3	7.4
Silicon		6.1	15.4

Table 4.2: The XPS C *1s* oxidation state positions along with the percentage of concentration, also the over all composition of the samples.

Figure 4.7 which presents the C *K*-edge XAS spectra from sample 1, shows the modifications within a fluorocarbon polymeric film as a function of exposure time to the synchrotron light source from the undulator beamline. The time indicated in figure 4.7 represents the time period that the sample is exposed to the beam with entrance and exit slit settings of 300. It is clear that constant exposure significantly alters the profile of the XAS absorption edge indicating changes in the carbon bonding environment as a function of exposure. Initially the fluorocarbon film is amorphous in nature with no definite structure however there are a number of well defined bonding environments as shown by XPS and the XAS data. Over time with constant exposure the peak at 287 eV starts to shift to lower bonding energies. After only two minutes of exposure to the beam the film has significantly changed, while after one hour

of exposure the initially distinct bonding environments of the carbon in the film are not apparent.

A number of well defined absorption features can be observed at time equals 0s which are similar to other XAS studies on similar materials [16] (Spectra 1 is offset for clarity). These features at 285 eV and 287 eV are due to transitions between occupied C *1s* core states (as measured by XPS and shown in Figure 4.6) and unoccupied conduction π^* orbitals. The peak at 285 eV is attributed to C=C*C or C=C*H, while the peak at 287 eV is attributed with a carbon having one F as its nearest neighbour [16]. For a carbon atom bonded to two fluorine's double bonded to another carbon, a peak should be observed at 290 eV however this cannot be seen from the XAS data of figure 4.7. As the XPS results of figure 4.6 show a significant amount of CF_2 this indicates that the bonding configuration must be in a C-CF_2-C environment [16].

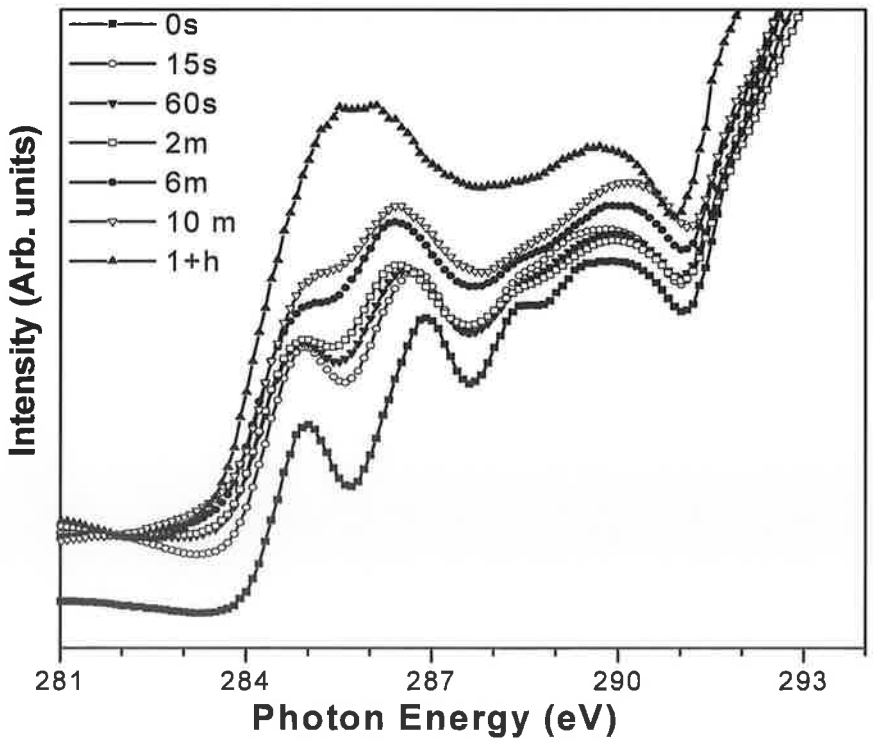

Figure 4.7: The C *K* edge XAS spectra of a steady state CF_x layer on Si (S1) with a variation in the time exposed to the light source.

Figure 4.8 presents the C K_α XES spectra from the two different fluorocarbon polymeric films on Si created by the plasma parameters of Table 4.1. The excitation energy was 296 eV, which is well above the absorption threshold for the C *1s* states. The peak at 296 eV is caused by the elastically scattered photons from the excitation source and is labelled "iv". The XES spectra have been normalized to uniform maximum peak height for comparison. Peak "i" is due to oxygen on the surface of the samples, This is caused by second order light as explained for the CDO spectrum. Sample S2 has a slightly more intense feature at 262.8 eV which is in agreement with quantitative XPS calculations carried out on the samples indicate that there was a higher oxygen concentration. The profile of the spectra for S1 is similar to that of other XES studies on similar a-CF_x films[16]. Peak intensity at point "ii" is mostly due to C-C sigma bonds. And peak "iii" and higher energies has been attributed to F type states [16]. In this spatial region of 283 eV to 285 eV there is little intensity in sample S2 consistent with the lack of fluorine content in the film. This is a significant finding as the bandgap of S1 will be up to 2 eV less than that of S2 which has more fluorine. This would suggest that the insulating properties of the highly fluorinated film will be less effective. Fluorocarbon plasmas are used in the etching of low dielectric materials in the semiconductor industry. These plasma methods leave a small thin film of CF_x on the surface and on the side wall of trenches in the dielectric such as the one presented in this thesis.

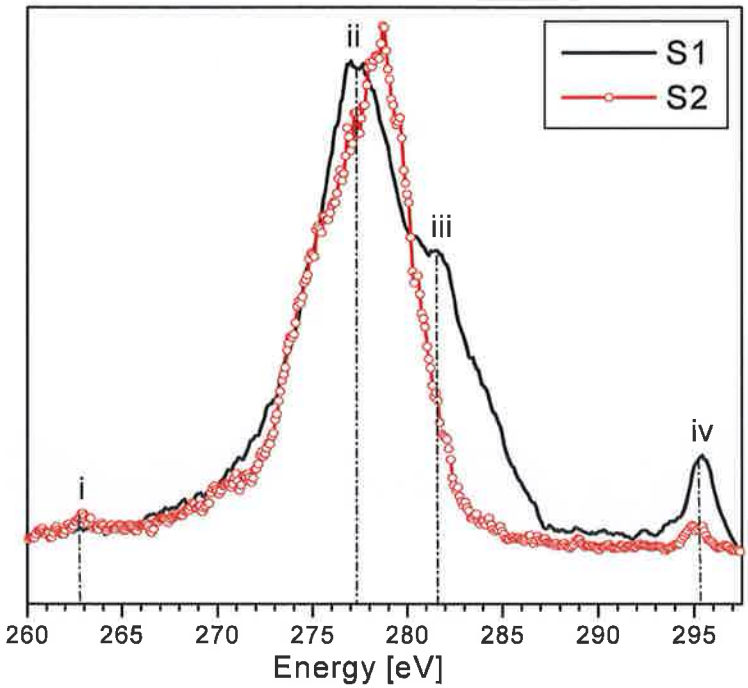

Figure 4.8: The C K_α XES spectra of a translated steady state CF_x layer on Si at an excitation energy of 295.4 eV.

Figure 4.9 presents a C K_α resonance XES spectra from a fluorocarbon polymeric film. The excitation energies used to excite these spectra are 285.2 eV. This corresponds to the first peak due to C-C bonding in the C *K*-edge XAS spectrum presented in Figure 4.7. The peak at 295.2 eV which is visible in both spectra and is caused by the elastically scattered excitation light labeled "iv. Peak "i" is due to oxygen incorporation in the samples as mentioned earlier. It is more visible in this set of spectra as less C sites are being excited therefore reducing the relative difference in peak heights. The general shape of the spectrum S2 in figure 4.9 is similar to that of the polymerized-C_{60} when in resonance with the C=C excited with a photon energy of 283.5 eV [17]. This can be attributed to the large number of C=C type bonds. Well resolved spectral features within these spectra may not be clearly visible. This is most probably due to the amorphous nature of these materials.

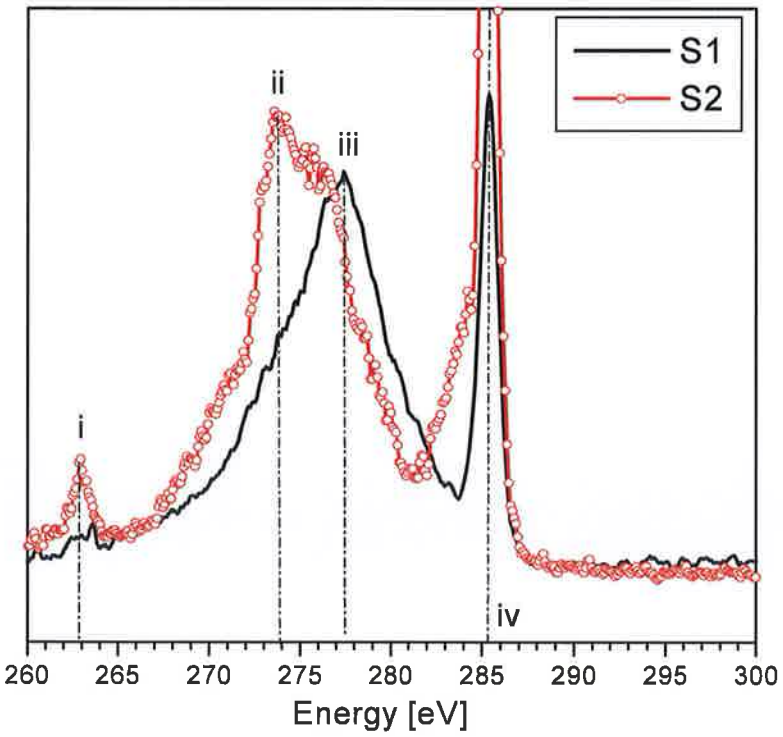

Figure 4.9: The C K_α XES spectra of a translated steady state CF_x layer on Si at an excitation energy of 285.2 eV.

4.4 Conclusions

The electronic structure of thin film ULK CDO and fluorocarbon layers has been measured using soft x-ray emission spectroscopy and x-ray absorption. Radiation damage in both thin films can be minimized by continuously translating the sample during measurement. The spectral changes induced by the radiation damage are consistent with the breaking up of the original material Si-CH_3 bonds in the CDO material and CF_x bonds in the fluorocarbon layers and the formation of graphitic C-C double bonds when exposed to the light source. The XES studies have shown that a low energy subband seen in C K_α emission spectra in CDO is due to second order light exciting O K_α emission. This work also suggests that the polymerized CF_x films with less fluorine content will act better as an insulator.

4.5 References

1. T. Shirafuji, Y. Nishimura, K. Tachibana, Thin solid films, 515 (2007) 4111
2. I. Reid , V. Krastev, G. Hughes Micro. Eng. 83 (2006) 2458.
3. Y. Furukawa, R. Wolters, H. Roosen, J.H.M. Snijders, R. Hoofman, Micro. Eng. 76 (2004) 25.
4. I Reid and G Hughes. Semi. Sci. Tech.. 21 (2006) 1354
5. J.X. Tang, Y.Q. Li, X. Dong, S.D. Wang, C.S. Wang, C.S. Lee, L.S. Hung, S.T. Lee, Appl. Surf. Sci. 239 (2004) 177.
6. K. Maexa, M. R. Baklanov, D. Shamiryan, F. Iacopi, S. H. Brongersma and Z. S. Yanovitskaya., J. Appl. Phys., 93 (2003) 8793.
7. N. Koch, D. Pop, R.L. Weber, N. Bowering, B. Winter, M. Wick,G. Leising, I.V. Hertel, W. Braun, Thin Sol. Films 391 (2001) 81.
8. J.E. Downes, C. McGuinness, P.A. Glans, T. Learmonth, D. Fu, P. Sheridan, and K.E. Smith, Chem. Phys. Lett. 390 (2004) 203
9. E. Z. Kurmaev, R. P. Winarski, J. C. Pivin, D. L. Ederer, S. N. Shamin, A. Moewes, K. Endo, T. Ida, G. S. Chang, and C. N. Whang. J. Elec. Spectro. Rel. Phenom. 87 (2000) 110.
10. E. Z. Kurmaev, R. P. Winarski, D. L. Ederer, J. C. Pivin, S. N. Shamin, A. Moewes, T. A. Callcott, G. S. Chang, and C.N.Whang. J. Elec. Spec. Rel. Phonom. 101 (1999) 565.
11. J. Guo, P. Skytt, N. Wassdahl and J. Nordgren. J. Elec. Spec. Rel. Phonom. 110 (2000) 41.
12. R. Winarski, D. L. Ederer, J. C. Pivin, E. Z. Kurmaev, S. N. Shamin, A. Moewes, G. S. Chang, C. N. Whang, K. Endo, and T. Ida, Nucl. Instrum. and Methods B 145 (1998) 401.

13. D. Schmeißer, P. Hoffmann, F. Zheng, F. Himpsel, H. Stegmann, E. Zschech. 8th International Stress-Induced Phenomena in Metallization, Symposium A42, 12-14 September (2005), Dresden, Germany

14. C. McGuinness, D. Fu, J.E. Downes, K.E. Smith, G. Hughes, and J. Roche, J. Appl. Phys. 94 (2003) 3919.

15. T. E. F. M. Standaert, C. Hedlund, E. A. Joseph, G. S. Oehrlein and T. J. Dalton J. Vac. Sci. Technol. A 22 (2004) 53.

16. Y. Ma, Hongning Yang, J. Guo, C. Sathe, A. Agui, and J. Nordgren, A.P.L. 72 (1998) 3353.

17. J. Guo, J. Nordgren, J. Elec. Spec. And Rel. Phen. 110 (2000) 105

Chapter 5: Influence of fluorocarbon based plasma etching on SiO_2 and ULK CDO

5.1 Introduction

This chapter deals with an investigation of the fluorocarbon based etching of chemical vapour deposition (CVD) deposited SiO_2 and of carbon doped oxide (CDO) both used as interlayer dielectrics (ILD) in device fabrication. Fluorocarbon based plasma etching (FBPE) is widely used in the dry etching of ILD layers [1,2,3,]. These fluorocarbon plasmas are known to result in the deposition of a polymeric film covering the surface during etching of the substrate material. The process of optimisation has been found to be challenging due to the complexity of the fluorocarbon plasma etch mechanism. Ion fluxes and ion energies [4], mechanisms of C_4F_8 dissociation [3], the molecular composition of deposited films [5] and radical kinetics of polymer film deposition [5] in pure C_4F_8 plasma have been extensively investigated. Chemical reactions in the etching plasma are extremely complex as there are a wide variety of chemical species present. Takahashi *et al.* [6] have proposed a list of possible reactions and reaction rates in fluorocarbon plasmas as shown in Table 5.1. It had been previously understood that a surface fluorocarbon film acted to inhibit the etch rate, however, recent studies have shown that ion induced deflourination of the fluorocarbon film can be the main supply of fluorine used in the etch process [5].

Table 5.1: Reactions in plasma

Reaction	Rate constant
$CF_3 + O \rightarrow COF_2 + F$	3.10×10^{-11} cm^3/s
$CF_3 + O_2 \rightarrow COF_3 + O$	Very small
$CF_2 + O_2 \rightarrow COF + F$	$2.0 \times 10^{-11} cm^3/s$
$CF_2 + O_2 \rightarrow$ products	$< 5 \times 10^{-16}$ cm^3/s
$CF + O \rightarrow CO + F$	1.2×10^{-11} cm^3/s

$CF+O_2 \rightarrow COF+O$	$1.6 \times 10^{-12}\ cm^3/s$
$F+O \rightarrow$	No data
$CHF_3 + F \rightarrow CH_3 + HF$	$1.82 \times 10^{-12}\ cm^3/s$

The aim of the first part of the study was to build up a broad picture of the chemical processes which characterize the etching mechanism of conventional SiO_2 ILD in a commercial reactor. The aim of the second part of the study was to carry out a more detailed investigation into the chemical composition of the fluorocarbon layers deposited for a range of plasma operational parameters on an ultra low-*k* (ULK) dielectric material and the effect this has on the dielectric layer etch rate. The chemical depth profile of the post-etched carbon-doped oxide (CDO) dielectric layers was also investigated. Correlations were established between the chemical composition and thickness of the fluorocarbon film and the etch rate of the CDO layer. X-ray photoelectron spectroscopy (XPS) was used to determine the chemical composition of the fluorocarbon layer, secondary mass spectroscopy (SIMS) was used for depth profiles of the samples and the residual thickness of the ILD layers was measured by spectroscopic ellipsometry (SE).

5.2 Influence of C_4F_8 / Ar/ O_2 plasma etching on SiO_2 surface chemistry

The effect of fluorocarbon etching on standard CVD SiO_2 ILD was investigated in this study. Plasma etch chemistries investigated include C_4F_8/Ar, C_4F_8/O_2 and C_4F_8/Ar/O_2 gas mixtures. The focus of the work was to investigate the impact that the different etch chemistries had on the etch rate of the SiO_2 ILD samples. Powers of 700W for the lower electrode and 1200W for

the upper electrode were applied together with the parameters listed in Table 5.2 for the plasma processing of the samples in this section.

Plasma Composition	C_4F_8 Flow [sccm]	O_2 flow [sccm]	Ar Flow [sccm]	Pressure [mbar]
C_4F_8 / Ar / O_2	40	50	200	65
C_4F_8 / Ar	40		200	65
C_4F_8 / O_2	40	100		65

Table 5.2: The plasma gases and flow rates used in the etching of the SiO_2 wafers in this work. Etching for 1, 2, 4 and 6 minutes were carried out for all plasma compositions.

Figure 5.1 shows results of spectroscopic ellipsometer measurements of the thickness of the SiO_2 layer as a function of etch chemistries and times. The C_4F_8 / Ar chemistry is shown to produce an almost linear etch rate over time (200 nm/minute) which is significantly faster than either of the other two oxygen-containing chemistries which have comparable removal rates (~30 nm/minute). These results therefore indicate that the presence of oxygen in the plasma composition hinders the etch rate of SiO_2 to a significant extent.

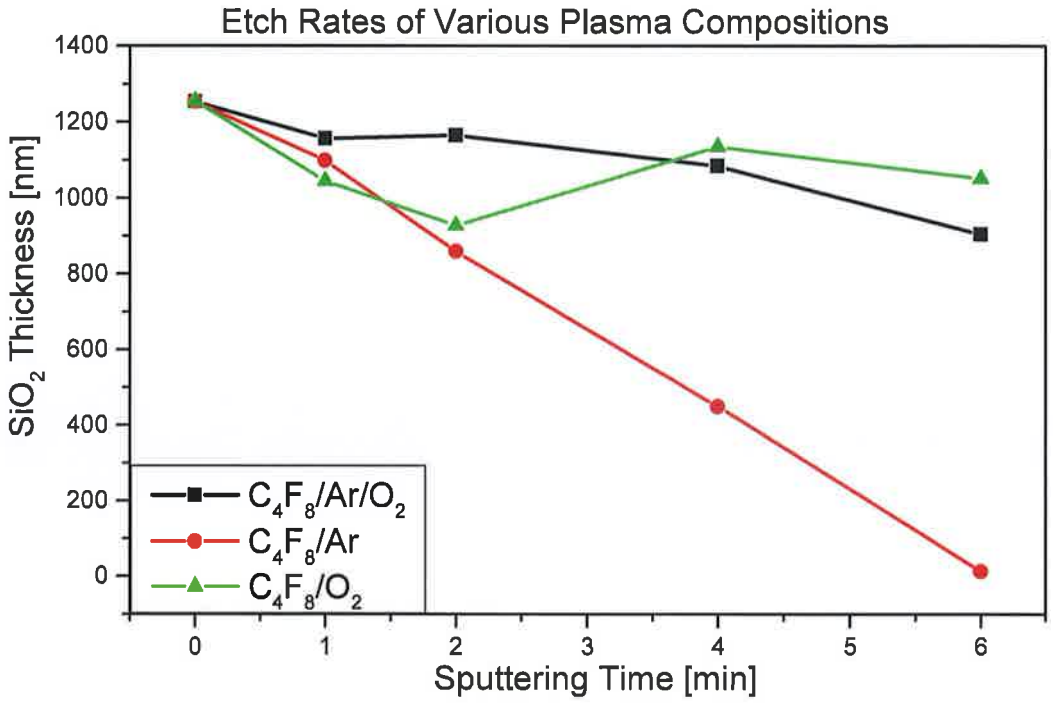

Figure 5.1: Spectroscopic ellipsometry thickness measurements of plasma processed SiO_2

The profile of the C *1s* peak after C_4F_8/Ar plasma etches is shown in Figure 5.2. After one minute a broad peak centered at 284 eV which is the characteristic binding energy of carbon in SiC is seen. A broad shoulder at 286 eV can be seen which is characteristic of carbon in bonding environments of the type CF. After 4 minutes etching, the C *1s* peak is significantly broadened and is centered at a binding energy of 284.1 eV, which suggests increasing amounts of bonds of the type SiC. After 6 minutes plasma etching the C *1s* peak at 284.4 eV has significantly increased in intensity and has developed a high binding energy component in the region of 288 eV, This carbon peak at 284.4 eV is typical of polymeric-type hydrofluorocarbon film formation due to competition between formation of Si-C bonds, formation of bonds of the type C-C and CF_x polymer network and etching. A high energy tail extending to 290 eV is characteristic of carbon in a CF environment. After in-situ Ar

sputtering for 1 minute, the C *1s* peak in the 6 minute plasma etched sample (spectra not shown) is shifted to 284.7 eV. This would suggest an increase in the C-F and C-O bonding environment close to the surface.

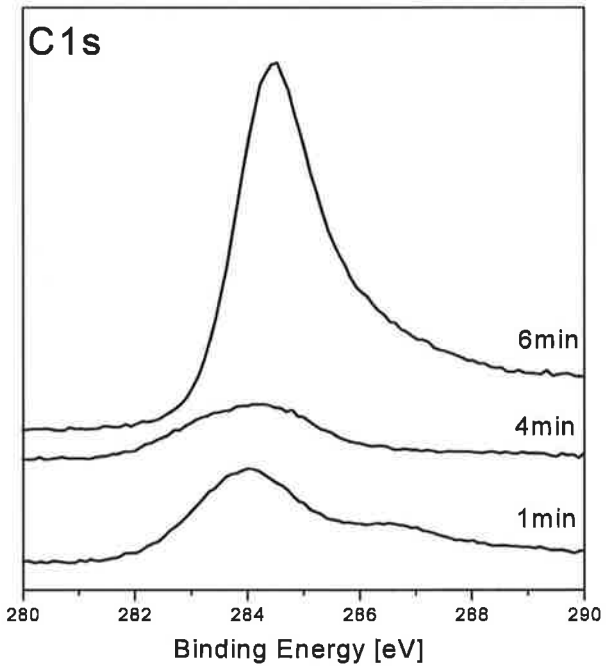

Figure 5.2: C *1s* profile of sample etched by C_4F_8/Ar plasma as a function of etch time.

The peak in Figure 5.3 shows the O *1s* peak after the same C_4F_8/Ar plasma etching sequence. After 1 minute etching a very broad peak centred at 531.5 eV is seen. After 4 minutes plasma etching the peak remains unchanged, while after 6 minutes plasma etching the peak intensity is substantially reduced. The attenuation of this peak after 6 minutes plasma etching is attributed to the almost complete removal of the SiO_2 film, due to the absence of an oxygen source either in the gas mix or the substrate [7]. This is confirmed by the spectra in figure 5.4 of the silicon *2p* signal in that the main peak is indicative of Si in a SiO_2 environment. It is attenuated as a function of the etch process and a small Si *2p* substrate signal at 99 eV binding energy is now visible for the 6 minute etch time. The fact that this substrate peak can just be

observed indicates that the fluorocarbon film is less than ~10 nm thick, which coincides with the sampling depth of XPS [6].

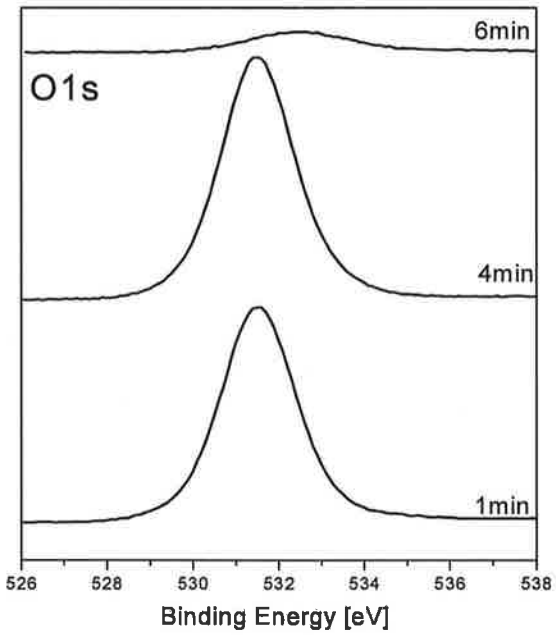

Figure 5.3: O *1s* peak of sample etched by C_4F_8/Ar plasma as a function of etch time.

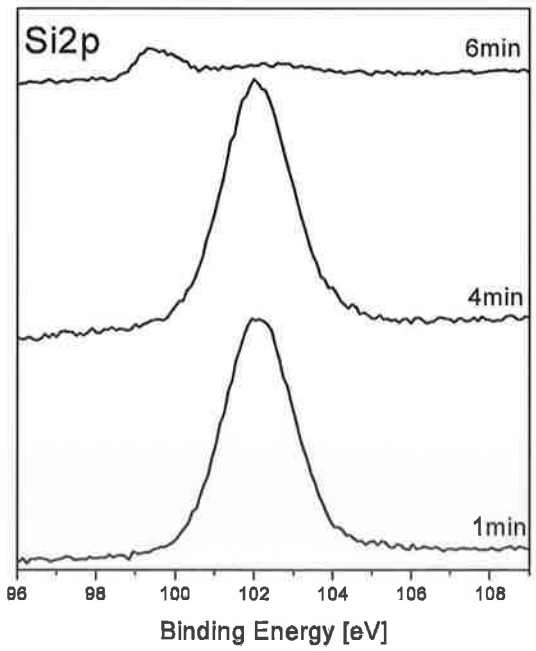

Figure 5.4: Si *2p* peak of sample etched by C_4F_8/Ar plasma as a function of etch time.

Figure 5.5 shows that the F *1s* peak after 1 minute C_4F_8/Ar plasma etching is a broad peak centered at 686.0 eV. After 4 minutes it shifts to 686.3 eV and its intensity decreases. After 6 minutes it is centered at 687.3 eV and its intensity is substantially increased. This is consistent with the formation of the polymeric layer discussed above. In-situ Ar depth profile studies of this film reveal that the intensity of the fluorine peak decreases sharply as a function of depth, demonstrating that the fluorine is localised at the surface of the SiO_2. The Ar *2p* peak (not shown) is not observed on the surface of the samples after plasma etching. It only appears after in-situ Ar ion sputter depth profiling in the XPS chamber and is due to some of the incident argon becoming embedded in the layer in the sputtering process. The absence of Ar peaks in the plasma etched sample means that Ar in the plasma does not participate in the etching reactions, but only provides energy for reactions between the SiO_2 substrate and the F and C species in the plasma.

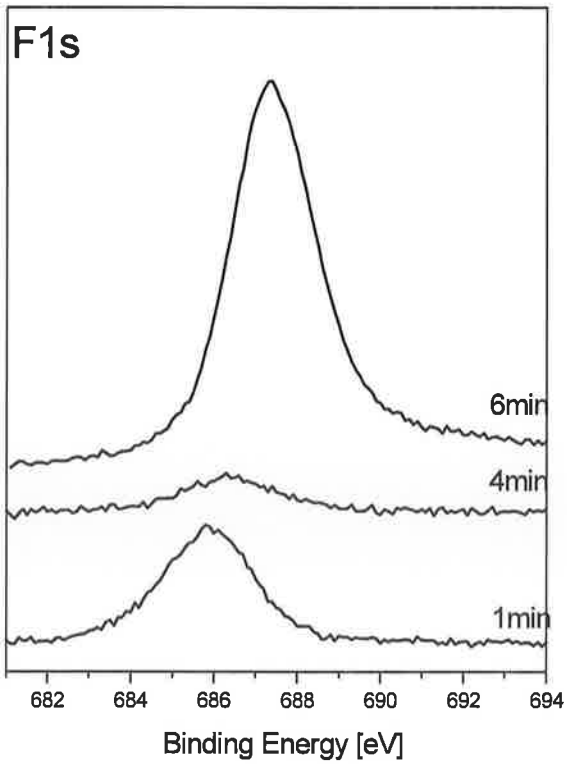

Figure 5.5: F *1s* peak of sample etched by C_4F_8/Ar plasma as a function of etch time.

Figure 5.6a shows the surface elemental composition (as determined by XPS) of the C_4F_8 / Ar etched samples after various plasma etch times. As was apparent from the peak analysis above, the concentrations of O and Si decrease once the plasma etching process has removed the SiO_2 layer and the concentrations of C and F increase due to the formation of a thin polymeric film on the silicon substrate. Figure 5.6b shows the surface elemental composition after different durations of C_4F_8 / O_2 etching. The ratio of the Si to O concentrations is characteristic of SiO_2 and it is clear that etching does not change the surface stoichiometry. Figure 5.6c shows the composition of the surface after different durations of C_4F_8 / Ar / O_2 etching. The relative intensities and binding energies of the O *1s* and Si *2p* peaks indicate that the sample is more heavily oxidised than in the case of the C_4F_8 / O_2 etching chemistry.

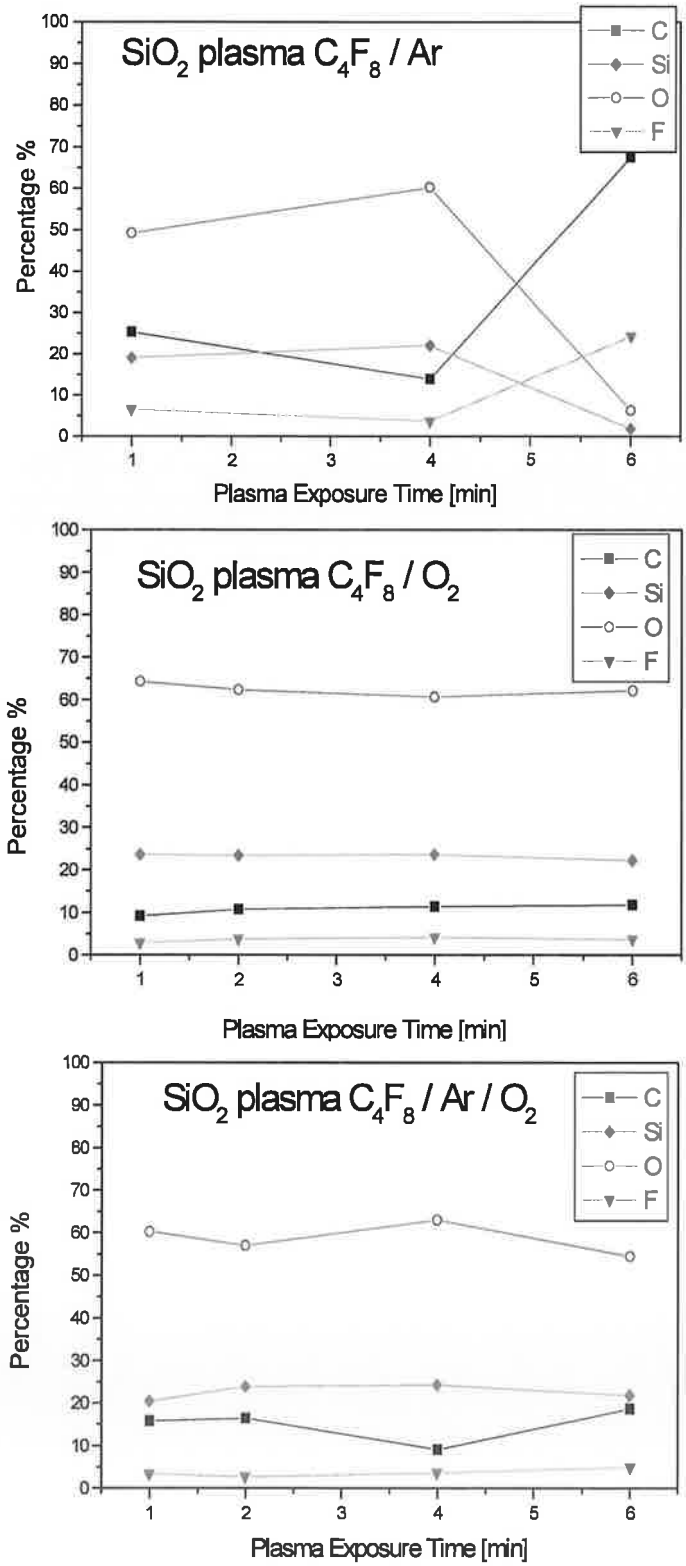

Figure 5.6: Composition on the surface after different durations of: (A): C_4F_8 / Ar etching, (B): C_4F_8 / O_2 etching and (C): C_4F_8 / Ar / O_2 etching.

In summary, these results are consistent with the C_4F_8/Ar 6 minute etch resulting in the complete removal of the SiO_2 overlayer from the silicon surface. Neither of the two etch mechanisms that involve oxygen result in the complete removal of the SiO_2 film for the etch times investigated in this study. For the C_4F_8 / Ar chemistry the subsequent growth of a thin fluorocarbon layer on the silicon surface results from the absence of a source of oxygen either from the etch gas mixture or oxygen released as an etch product of the SiO_2 removal. A fluorocarbon film only forms on the surface in the absence of oxygen which could be supplied by the addition of oxygen in the feed gases or the release of oxygen from the SiO_2 etched layer.

Figure 5.7 illustrates a SIMS depth profile of the sample which was subjected to a C_4F_8 / Ar plasma etch for 6 minutes. The C and F signal intensities are significantly higher than the O or Si intensities. These results are consistent with the XPS studies indicating the presence of a fluorocarbon layer on the surface. The presence of Ar in the SIMS spectra, but not in the XPS data confirms that Ar does not take part in the plasma chemical reactions with the SiO_2 and is introduced only via Ar sputtering in the SIMS process.

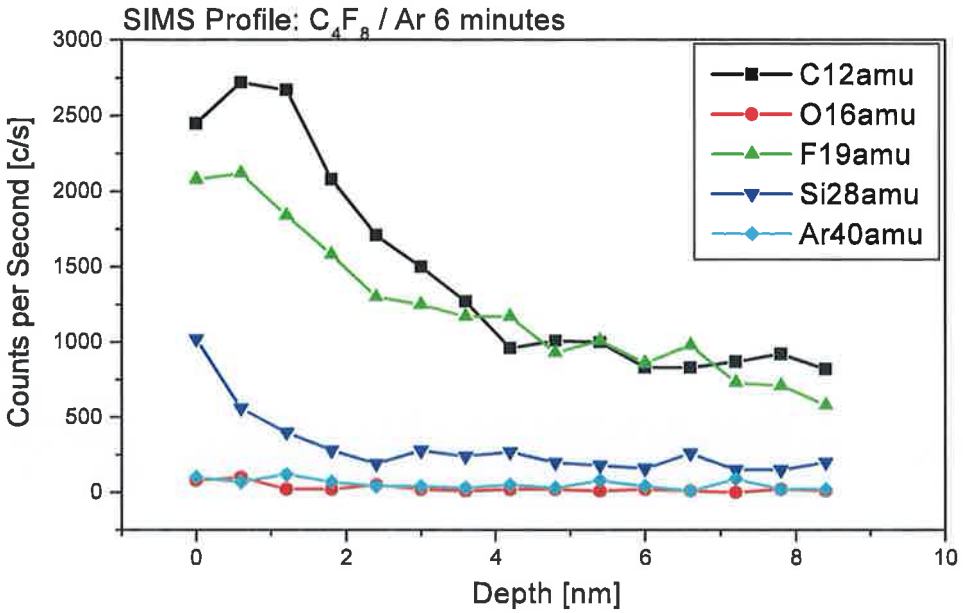

Figure 5.7: SIMS profiles exposed to different chemistries for 6 minutes.

SIMS analysis of all the plasma-etched samples with varying plasma chemistries reveals that the carbon is primarily surface-localised within the fluorocarbon film. This is in contrast with the profiles obtained for fluorine, which indicate that the fluorine penetrates into the SiO_2 layer (see figure 5.8). Only when the SiO_2 layer has been fully etched away does the fluorine become localised at the surface in the polymeric fluorocarbon film. The SIMS profiles confirm the XPS finding that more carbon is deposited on the SiO_2 layer using the C_4F_8 / Ar etch chemistry than with either of the oxygen-containing plasmas. By looking at SIMS data of the 6 minute etched sample in a C_4F_8 / Ar plasma indicates a thickness of ~13 nm for the fluorocarbon film in agreement with the XPS data.

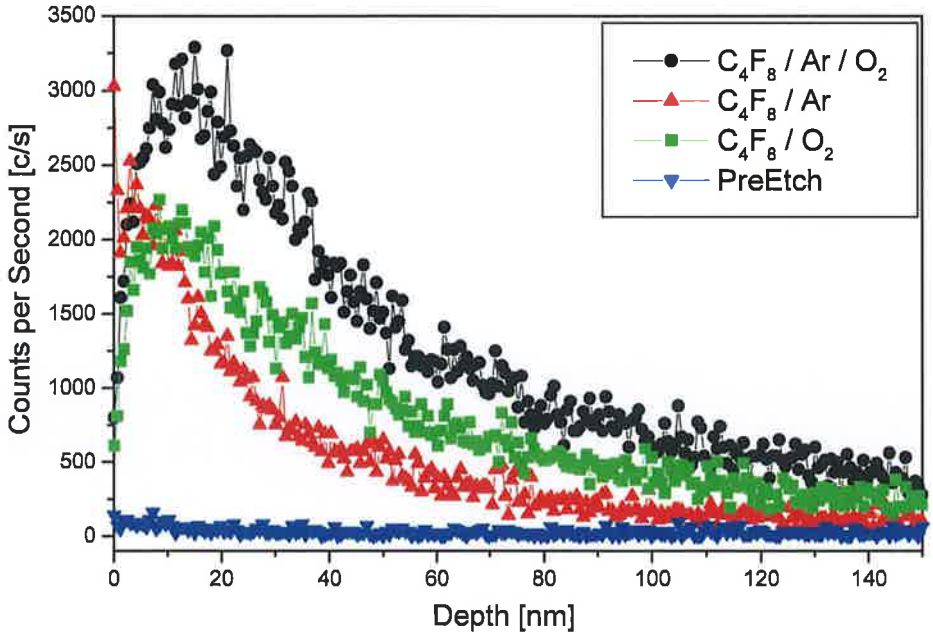

Figure 5.8: SIMS depth profiles of fluorine incorporated into SiO_2 when etched with different chemistries for 4 minutes in a plasma.

Reactions at the plasma-solid interface are primarily exchange reactions due to different bond strengths between oxygen, carbon and silicon on one hand and fluorine, carbon and silicon on the other hand.

5.2.1 Etch Mechanism

Figure 5.9 shows a schematic diagram of adsorption of CF radicals on the SiO_2 surface and the effects of Ar ion bombardment.

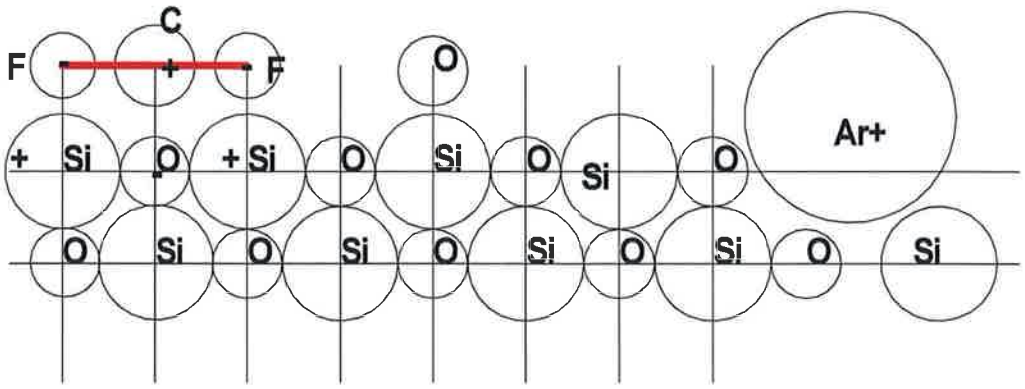

Figure 5.9: Schematic of adsorption of CF radicals on SiO_2 surface and Ar+ ion bombardment.

In Table 5.3 the electronegativities and covalent radii used for this diagram (according to Alcock [8]) are listed. The higher electronegativity the smaller covalent radius. However, the relation is not linear; ions having higher electronegativity (O and F) attract electrons in the bond and develop partial negative charge. Atoms with lower electronegativity (C and Si) become partially positively charged. Due to Coulomb forces the CF radical is adsorbed as shown in the figure and the C-F bond is stretched and eventually broken. This results in subsequent bond formation between these adsorbed species and atoms on the surface. Argon ion bombardment is crucial for providing kinetic energy to disrupt the bonding in the near surface region increasing its reactivity with the gaseous plasma species. In the process of plasma etching, high kinetic energy Ar ions physically sputter clusters of atoms from the surface and provide vibrational energy to the atoms of the surface lattice itself. This provides sufficient energy to surmount potential energy barriers to promote chemical reactions between the C and F with O and Si substrate atoms. From *Pauling et. al.* [9] we find for the univalent radius of Ar in a standard crystal the value of 154 pm, but for the free ion the value of 200 pm from Alcock [8] is considered to be a better approximation.

Table 5.3: Comparison of atomic parameters for the relevant elements.

Element	Electronegativity	Covalent radius [pm]
F	4.1	61.9
O	3.5	65.9
C	2.5	76.7
Si	1.7	109.0

From Tables 5.4 and 5.5 it may be seen that stronger bonds are formed at the expense of weaker bonds. Due to kinetic energy and excited states of radicals an exchange reaction between the plasma and the SiO_2 occurs:

$$CF + SiO_2 \rightarrow CO_2 + SiF + CF \text{ (polymer)} \qquad (4.1)$$

Oxygen hinders etching because it can be adsorbed on the active sites of the surfaces preventing fluorine from being adsorbed and taking part in the exchange reaction (4.1).

The XPS results presented above for different etch durations provide a snapshot in time of the chemical species present on the surface and their relative concentrations. The surface chemical composition reflects the competition between two main processes, namely, the sputtering due to breaking of bonds resulting in material removal and the formation of Si-C and Si-F bonds promoting the formation of a fluorocarbon layer. The study has shown that this layer only shows significant growth in the absence of oxygen, whether from the plasma or the substrate. Fluorine, having higher electronegativity than oxygen can displace oxygen in the silicon dioxide layer. This is in accordance with the relative strengths of the Si-F and Si-O bonds (Table 5.4).

Table 5.4: Comparison of bond parameters

(heats of formation kcal/mol according to Pauling [9])

C-Si	69.3	C-F	105.4
C-O	84.0	C-F	105.4
Si-O	88.2	Si-F	129.3

Table 5.5: Comparison of bond parameters

(standard enthalpy of formation kJ/mol according to Pauling [9])

SiO_2 (crystal)	859
SiF_4	1548
CF_4	912

Figure 5.6a showed that the concentrations of C and F rise significantly following the removal of the SiO_2 layer. In the polymer network bridging atoms of the type –O-, -C- and –Si- could also be present. The surface chemistry is a complex mix between etching and deposition and the control of the concentrations of the reactive species

5.3 Influence of plasma parameters on the chemical composition of steady state fluorocarbon films on the surface of ULK CDO

Having studied the basic interactions of a fluorocarbon based etch mechanism with SiO_2 ILD layers, a subsequent systematic investigation of how etch parameters influence the etch characteristics of ultra low-*k* CDO films was carried out.

Table 5.6 summarizes the range of plasma conditions and chemistries used to etch the blanket Aurora™ CDO films in C_4F_8/Ar and C_4F_8/O_2/Ar discharges. All the plasma

conditions investigated led to the formation of a measurable steady-state fluorocarbon layer on the surface of the underlying CDO. In order to establish that the composition of the fluorocarbon film for a particular set of etch parameters had reached steady-state conditions [12], etch times of 15, 30, 45, 60 and 120 s were investigated. All samples showed similar etch rates and similar relative intensities of the F-C oxidation states indicating that steady-state conditions had been reached after a 15 s period. The dielectric films investigated all were etched for 15 s in the Lam Excelan and the residual thicknesses were referenced to the thickness of the unetched T0 film, which was 490 nm. Sample conditions T1, T2 and T3 involved a systematic variation of the plasmas' density by increasing the high frequency (HF) power from 200 W to 800 W in plasmas containing no O_2 flow into the chamber. Sample conditions T4 to T6 varied low frequency (LF) power from 200 W to 600 W with a flow of 3.3 sccm of O_2 into the reactor. All etch gas mixtures contained 500 sccm of Ar and had a base pressure of 150 mbar.

	HF Power [W]	**LF Power [W]**	**O_2 flow [sccm]**	**C_4F_8 [sccm]**	**Ar [sccm]**	**Pressure [mbar]**	**Time [s]**	**Thickness [nm]**
T0	0	0	0	0	0	0	0	488
T1	**200**	200	0	10	500	150	15	488
T2	**400**	200	0	10	500	150	15	482
T3	**800**	200	0	10	500	150	15	442
T4	800	**200**	3.3	10	500	150	15	441
T5	800	**400**	3.3	10	500	150	15	372
T6	800	**600**	3.3	10	500	150	15	355

Table 5.6: Plasma parameters investigated in this study.

Figure 5.10 shows the curve-fitted components of the C *1s* peak following a 15 s etch with varying plasma HF power in a C_4F_8/Ar discharge. Throughout the study, the C *1s* oxidation states were fitted using a mixed singlet which is a combination of a Lorentzian and a Gaussian peak. Two main trends are observed in the profile of C *1s* as a function of increasing HF power. The intensity of the C–Si component peak becomes more pronounced indicating a thinner fluorocarbon film as this carbon signal originates from the CDO substrate. The other noticeable feature of the spectra is that the relative intensities of the C–F_x component peaks decrease in relation to the C–CF_x derived peak with increasing power.

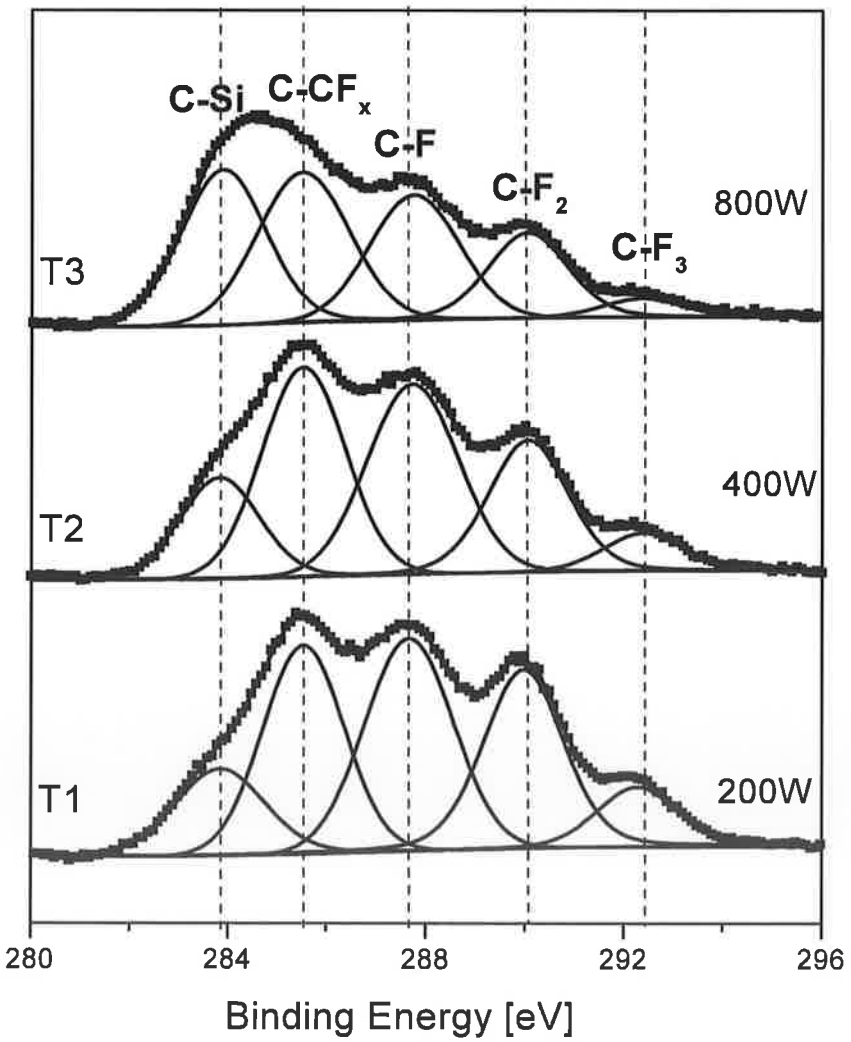

Figure 5.10: The curve fitted components of the C *1s* peak following a 15 second etch as a function of HF ion density power.

This trend is more apparent from figure 5.11 which plots the percentage of each carbon oxidation state as a function of HF power. The graph highlights the fact that as well as the fluorocarbon layer becoming thinner, there is a compositional change in the fluorocarbon film with increasing HF power which results in a decreased contribution from the higher C–F*x* oxidation states relative to the C–CF_x component peak. This has also been observed in a previous study by Arai *et al* [13] which reported that the concentration of highly fluorinated carbon atoms in the polymeric fluorocarbon films deposited at high RF power is smaller than in fluorocarbon polymers deposited at low RF power.

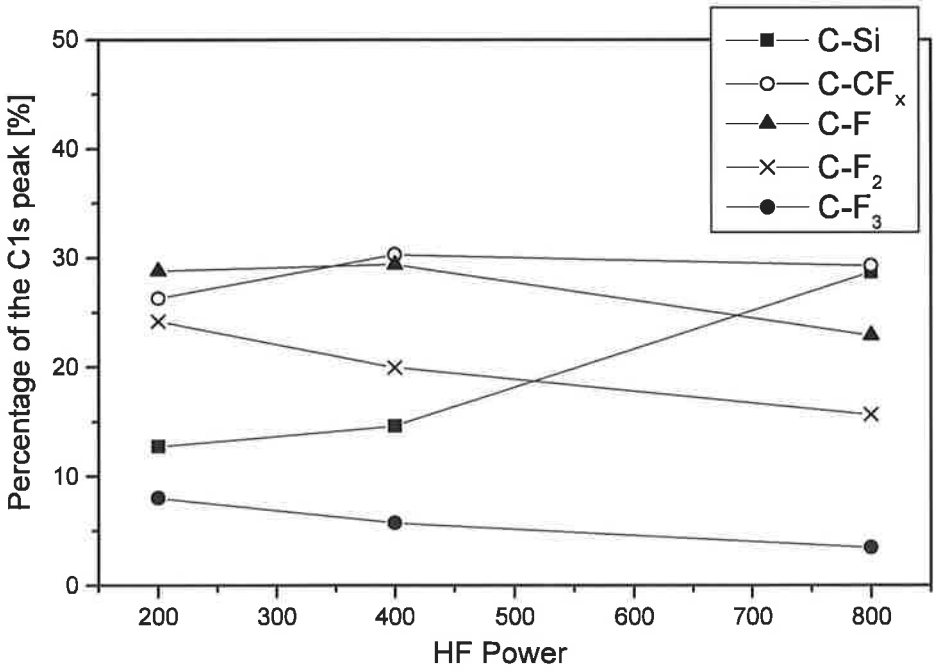

Figure 5.11: Plots of the percentage of each carbon oxidation state as a function of HF ion density power for samples T1 to T3 (C_4F_8/Ar plasma).

Figure 5.12 shows the curve-fitted components of the C *1s* peak following a 15 s etch with the C_4F_8/O_2/Ar discharge for varying LF powers. The trend is similar to the changes induced by increasing plasma HF power in that there is a reduction in the thickness of the fluorocarbon

film and a decrease in the contribution of CF*x* oxidation states to the C *1s* spectrum which can be seen more clearly in the percentage data presented in figure 5.13.

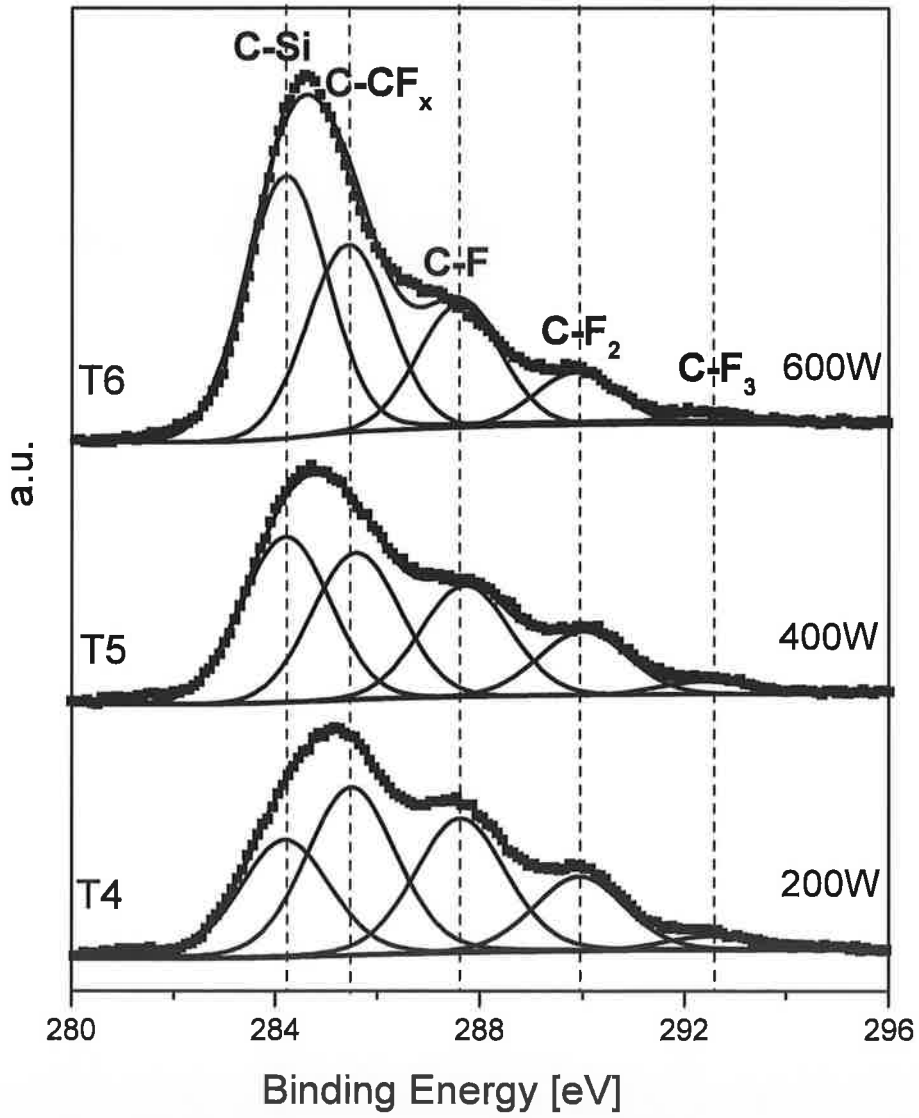

Figure 5.12: The curve fitted components of the C *1s* peak following a 15 second etch as a function of LF ion energy power.

The residual CDO thickness results presented in table 5.6 indicate that the etching of the film can occur in the absence of gaseous oxygen if the HF power is sufficiently high. The CDO film in sample T3 with a HF power of 800 W has been etched without any gaseous oxygen flow. In fact, the addition of 3.3 sccms of oxygen at this HF power level (sample T4) has no measurable impact on the CDO etch rate. It therefore appears that for these materials, the steady-state fluorocarbon layer thickness is a key parameter that determines the etch rate of the layer [14].

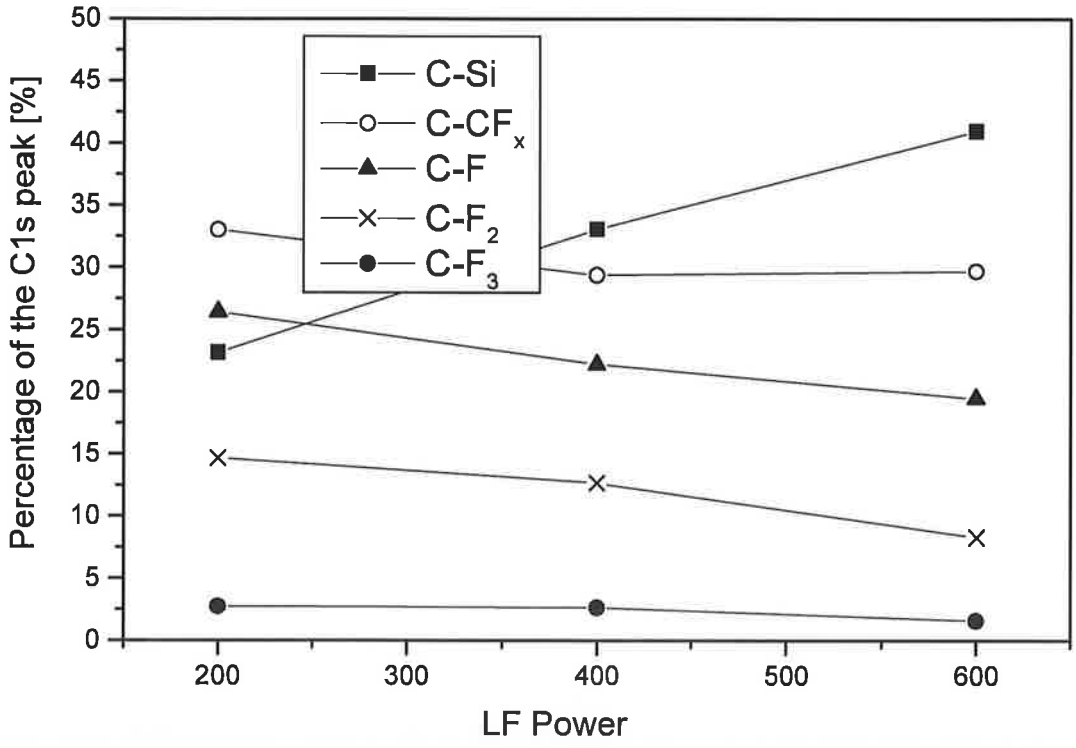

Figure 5.13: Plots of the percentage of each carbon oxidation state as a function of LF ion energy power for samples T4 to T6 (C_4F_8/Ar/O_2 plasma).

Figure 5.14 shows the ion depth profiles of the C *1s* percentage concentrations as a function of depth for traces of different HF power. The unprocessed sample, T0, has a carbon

concentration of approximately 15% through the film when the surface contamination component has been removed following the first bombardment. It is apparent from the depth profile data that the thickest fluorocarbon films were deposited on samples T1 and T2, neither of which displays any evidence of etching. Fluorocarbon films greater than 2.5 nm have been shown to significantly reduce the etch rate [7].

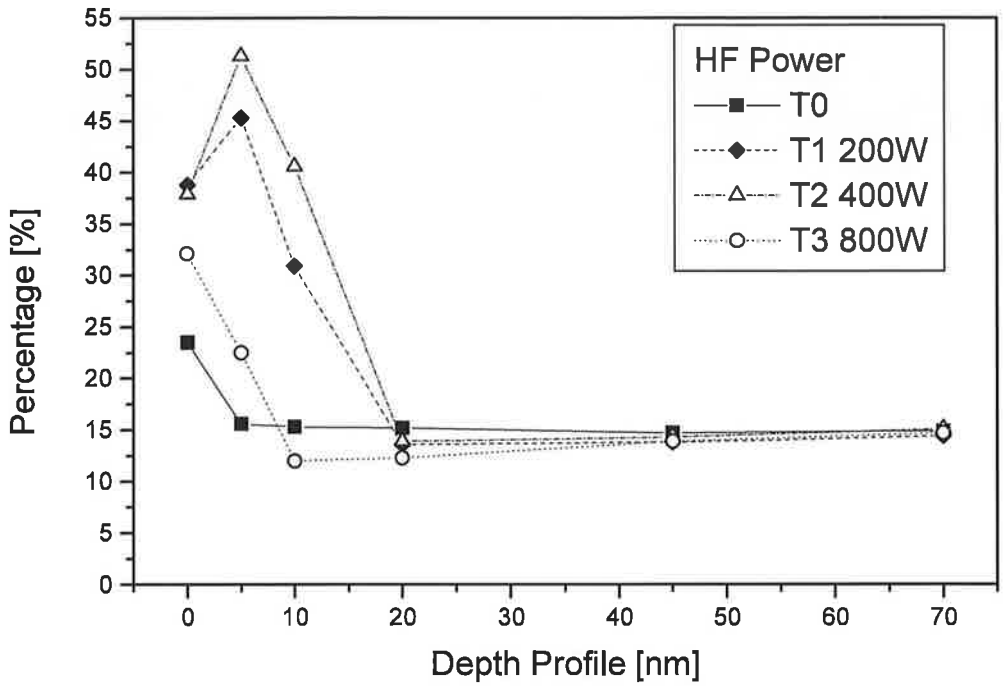

Figure 5.14: Argon bombarding depth profiles of the carbon concentrations into the sample as a function of ion density power. The unetched reference T0 is shown for comparison.

Figure 5.15 plots the argon ion depth profile of the C *1s* percentage concentration for variations in the LF power. Sample T5 has higher etch rates, which can be attributed to an increase in LF power accelerating the ions towards the sample surface thereby increasing the amount of ion bombardment. Fluorocarbon species can be dissociated and ion bombardment can drive species into the substrate by a diffusion-like process thereby enhancing the etch rate [14]. T6 shows the thinnest of the fluorocarbon films and the corresponding highest etch rate.

Operating the reactor at high RF power results in the polymerisation reactions, which is activated on the surface by the impact of energetic ions, forming a fluorocarbon layer. However, as the ion density power increases, the deposited polymers are likely to be etched by high energy ion bombardment. This is considered to be the reason why the thickness of the fluorocarbon layer decreases with increasing ion density power and why the number of fluorine atoms incorporated in the polymer film also decreases. If this detached fluorine diffuses through the film to the substrate, it can initiate the etching reaction mechanisms [12,15]. These results are consistent with the CDO etching occurring in the presence of a thin surface fluorocarbon film which acts as a source of fluorine for the etch process. The high powers act to both reduce the fluorocarbon thickness and defluorinate the film, both processes which enhance the etching process.

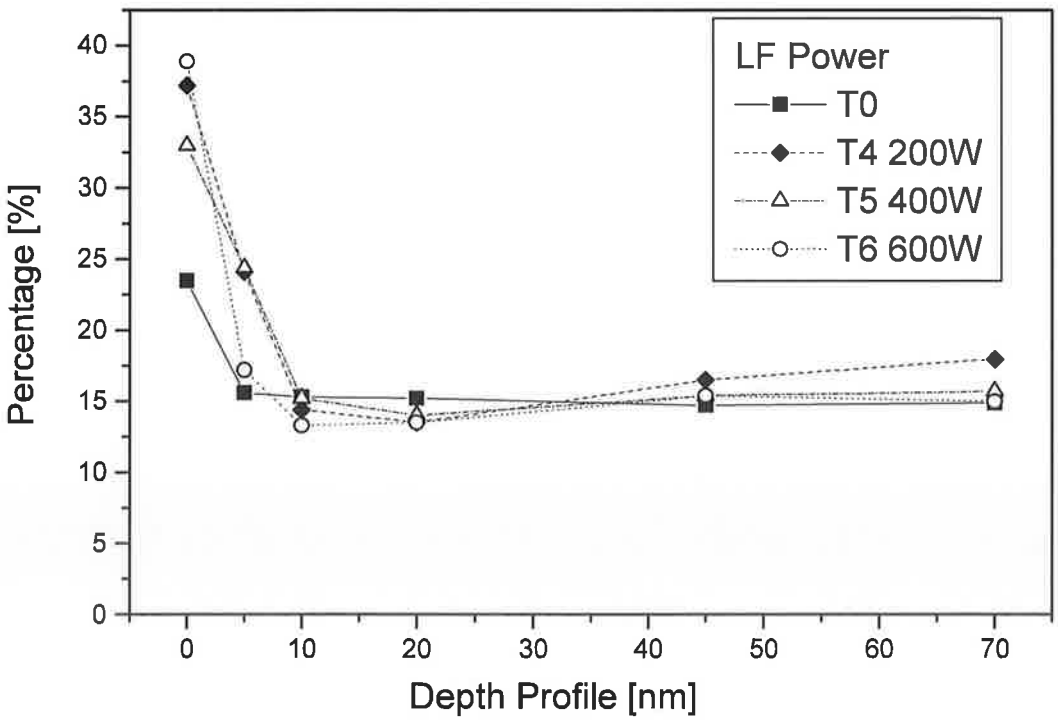

Figure 5.15: Argon depth profiles of the carbon concentrations into the sample as a function of ion energy power. The unetched reference T0 is shown for comparison.

5.4 Conclusions

We have studied the plasma assisted etching of SiO_2 in a commercial RF reactor with a variety of $C_4F_8/Ar/O_2$ chemistries by XPS and SIMS. These studies show that a CFH polymeric amorphous film is formed in all conditions investigated. The film thickness is strongly dependent on the presence of an oxygen source in the system, either via the plasma gas mix or from the SiO_2 substrate. When oxygen is present, the fluorocarbon film remains thin, and will not, of its self, inhibit etching, as observed for the C_4F_8 / Ar plasma. However, the presence of oxygen in the feed gases reduces the etch rate significantly as active sites for fluorine adsorption are blocked. This prevents the fluorine etch mechanism and also inhibits the polymeric film growth. The argon in the plasma does not participate in etching reactions and only provides energy for the reactions in which F and O are involved.

The second part of the study showed how etch parameters influence the etch characteristics of ultra low-*k* CDO films. HF power reduces the thickness of the fluorocarbon layer which leads to increases in the etch rate, even in the absence of gaseous oxygen. It also has the effect of reducing the concentration of the $C–F_x$ species to the carbon *1s* peak profile. Increasing the ion energy power also reduces the thickness of the fluorocarbon layer and has the same effect as ion density power on the concentration of the $C–F_x$ species. These findings are consistent with the etch model where the fluorine is detached from the fluorocarbon layer and diffuses to the interface to take part in the etch process.

5.5 References

1. T. Yasuda, G.Lucovsky, J. Vac. Sci. Technol. A 11 (1993) 2496.
2. S. J. Ullal, H. Singh, J. Daugherty, V. Vahedi, and E.S, Aydil, J. Vac. Sci. Technol. A 20 (2002) 1195.

3. G.S. Oherlein, Y. Zhang, D. Vender, M. Haverlag, J. Vac. Sci. Technol. A 12 (1994) 329.
4. N. Goyette, Y. Wang, M. Misakian and J. K. Olthoff, J. Vac. Sci. Technol. A 18 (2000) 2785.
5. K. Takahashi and K. Tachibana, J. Appl. Phys. 89 (2001) 893.
6. K. Takahashi, M. Hori and T. Goto, J. Vac. Sci. Technol. A 14 (1996) 2004
7. M. Schaepkens, T. E. F. M. Standaert, N. R. Rueger, P. G. M. Sebel, G. S. Oehrlein, and J. M. Cook, J. Vac. Sci. Technol. A 17 (1999) 26.
8. N.W.Alcock, "Coordination Chemistry (Bonding and structure)", Ellis Horwood, New York, (1990).
9. L.Pauling, "The nature of chemical bond", Cornell University Press, Itaca, N.Y. (1963).
10. D.N. Belton, S.J. Schmieg, J. Vac. Sci. Tech. A 8 (1990) 235.
11. D.Humbird, D.B.Graves, X.Hua, G.S.Oehrlein,, Appl. Phys.Lett. 84 (2004) 1073.
12. T. E. F. M. Standaert, M. Schaepkens, N. R. Rueger, P. G. M. Sebel, G. S. Oehrlein and J. M. Cook. J. Vac. Sci. Technol.A 16 (1998) 239
13. S. Arai, K. Tsujimoto and S. Tachi, Japan. J. Appl. Phys. 31 (1992) 2011
14. X Hua, Stolz C, Oehrlein G S, Lazzeri P, Coghe N, Anderle M, Inoki C K, Kuan T S and Jiang P. J. Vac. Sci.Technol. A 23 (2005)151
15. T. E. F. M. Standaert, C. Hedlund, E. A. Joseph, G. S. Oehrlein and T. J. J. Dalton. Vac. Sci. Technol. A 22 (2004) 53

Chapter 6: Suppression of carbon depletion from carbon-doped low-*k* dielectric material.

6.1 Introduction

The aim of this work is to determine the plasma operating conditions which result in the presence of a fluorocarbon layer on the surface of the CDO during etching but doesn't impact on the etch rate, as thick fluorocarbon films have been shown to inhibit the etching process. The Aurora™ ULK CDO films were etched in a commercial plasma reactor containing a $C_4F_8/O_2/Ar$ based chemistry where the composition of feed gases could be systematically controlled in order to determine the optimal conditions for CDO etching.

Section 6.2 investigates the chemical composition of the fluorocarbon layers deposited for a range of plasma etch parameters on an ultra low-*k* (ULK) dielectric material and the effect this has on the etch rate of the dielectric layer. The chemical depth profile of the post-etched carbon doped oxide (CDO) dielectric layer was also investigated as the presence of oxygen in the plasma chemistry during etching can result in carbon depletion from the CDO film which results in an increase in the *k* value. Correlations were established between the chemical composition and thickness of the fluorocarbon film and the etch rate of the CDO layer.

The issue being addressed in section 6.3 is what effect the C_4F_8/O_2 ratio had on the possible depletion of carbon from the CDO substrate using industrial plasma conditions. These processing parameters replicate the actual power settings and etch gas ratios used in commercial plasma etches. Our studies showed that controlling the plasma conditions to maintain the presence of a thin fluorocarbon layer on the surface of the CDO during the etching process suppresses the carbon depletion from the dielectric film.

The chemical composition of the plasma-etched wafers were analysed using x-ray photoelectron spectroscopy (XPS) and the etch rate was determined from measuring the residual film thickness by spectroscopic ellipsometry (SE) and secondary ion mass spectroscopy (SIMS) was used to study the depth profiles of the samples.

6.2 Investigation of different feed gas ratios on fluorocarbon layers and their influence on the suppression of carbon depletion of ULK CDO layers.

Table 6.1 summarises the range of plasma conditions and etch chemistries using $C_4F_8/O_2/Ar$ based chemistry on the CDO films. The influence of independently varying the O_2 and C_4F_8 gas flows on the etch rate and the surface chemical composition were determined with both the ion density and ion energy powers set at 200W. The CDO film thickness values following a 15 second etch in the Exelan were referenced to the pre-etch thickness of the T0 film which was 490 nm. Increasing the oxygen concentration above 3.3 sccm to 10 sccms had no major impact on the etch rate of the CDO layer as samples etched under conditions T2 to T5 have the same residual CDO thickness. Only when the C_4F_8 concentration is reduced to 3.3 sccm is the etch rate inhibited.

	Ion Density Power [W]	Ion Energy Power [W]	O_2 flow [sccm]	C_4F_8 [sccm]	Ar [sccm]	Pressure [mbar]	Time [s]	Thickness [nm]
T0	0	0	0	0	0	0	0	490
T1	200	200	**0**	10	500	150	15	488
T2	200	200	**3.3**	10	500	150	15	439
T3	200	200	**6.6**	10	500	150	15	435
T4	200	200	**10**	**10**	500	150	15	436
T5	200	200	10	**6.6**	500	150	15	437
T6	200	200	10	**3.3**	500	150	15	467
T7	200	200	10	**0**	500	150	15	464

Table 6.1: Plasma parameters carried out on CDO

The thickness measurements indicate that the absence of oxygen from the plasma feed gases at these plasma power settings results in negligible substrate etching as illustrated by sample T1. Figure 6.1 shows the carbon *1s* core level peak for all plasma conditions with the vertical lines identifying the positions of the different oxidation states present. It is clear from spectra T1 to T4 that the thickness of the fluorocarbon film is reduced significantly as the O_2 flow is increased to 10 sccm. Subsequent reductions in the C_4F_8 gas flow from T5 to T6 continue this trend with no evidence of any fluorocarbon film present when the C_4F_8 gas flow was completely stopped. The C-Si related peak, attributed to carbon in the CDO film, increases in intensity through out the sequence confirming that the thickness of the fluorocarbon film decreases as the plasma conditions change from T1 to T7.

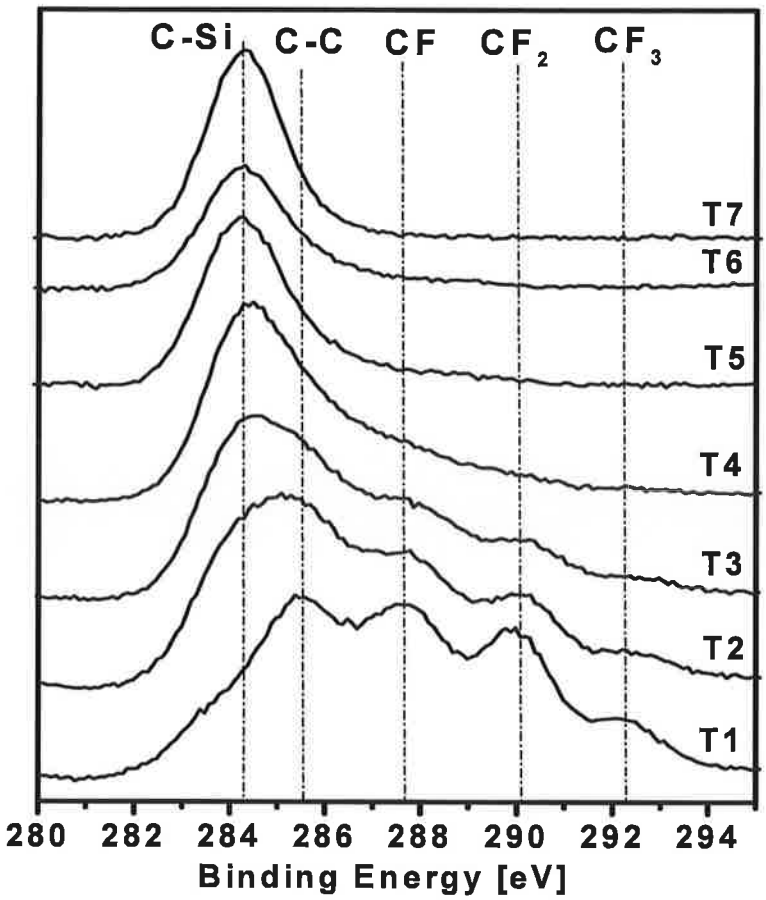

Figure 6.1: The carbon *1s* core level peaks following a 15 second etch as a function of feed gases.

Figure 6.2 plots the intensity of all the carbon oxidation state peaks for the different plasma conditions and shows that the C-F_x related features decrease in intensity while the substrate related carbon feature increases. The thickness results indicate that the etching of the CDO occurs even in the presence of a surface fluorocarbon layer in agreement with previous studies [1, 2]. The plasma conditions T1 led to the formation of the largest of the fluorocarbon films to be produced.

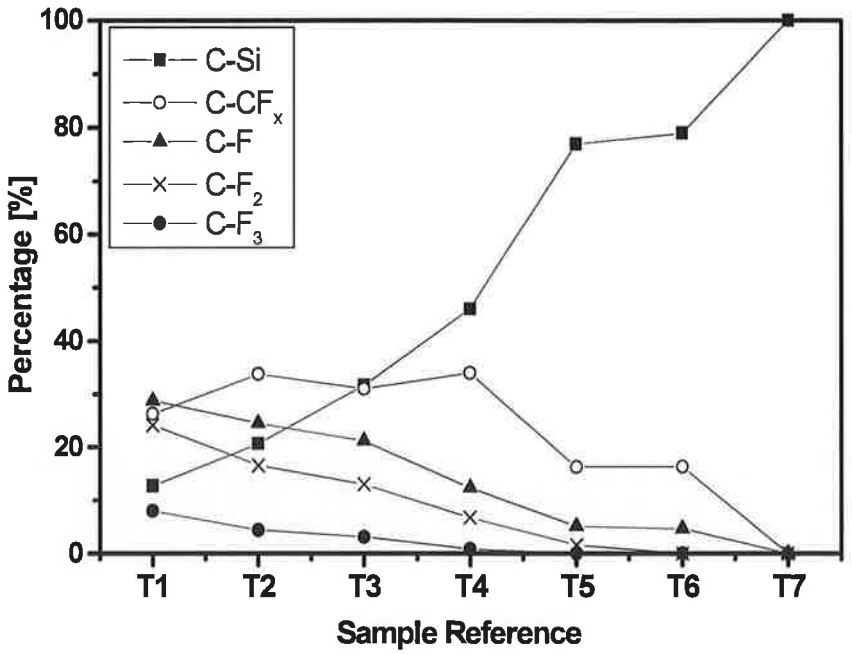

Figure 6.2: Plots of the percentage of each carbon oxidation state as a function of feed gases.

Shown in figure 6.3 are the argon ion XPS depth profiles of the C *1s* peak in the CDO after the 15 second plasma etch for a selection of the samples investigated. T0 is the unprocessed film which has a surface localized carbon contamination layer and a 15% carbon concentration throughout the entire layer. There is a surface contribution to the carbon signals for all samples and this is attributed to exposure of the surface to the atmospheric conditions between removal from the plasma etcher and insertion into the surface analysis system. Samples T1 and T4 show a high percentage of carbon prior to depth profiling which is attributed to the presence of a fluorocarbon film on the surface. Once this film has been removed these samples also exhibit a 15% carbon concentration in the bulk of the CDO film. Plasma conditions T5 and T7 show significant evidence of carbon depletion from the ULK CDO as the concentration drops to 10% in the near surface region of the film [3].

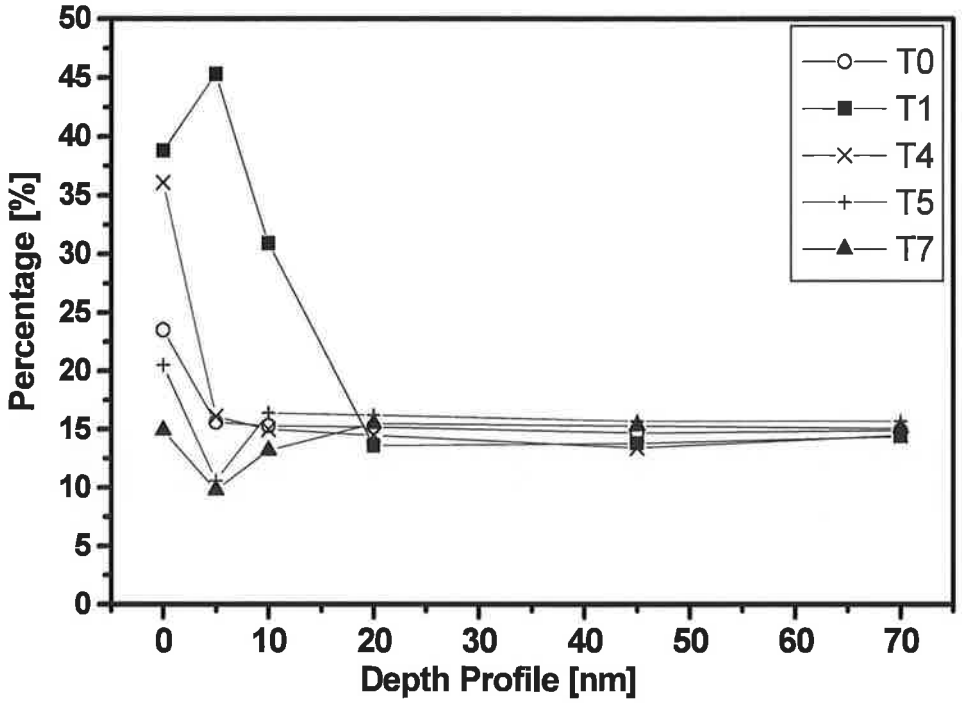

Figure 6.3: Argon depth profiles of the carbon concentrations into the sample as a function of feed gases. The unetched reference T0 is shown for comparison.

Figure 6.4 plots the etch rate, calculated in thickness removed per minute, for the different plasma conditions investigated. A lack of oxygen in the plasma gas composition leads to the deposition of the thick fluorocarbon film and no etching as illustrated by sample T1. Too high a concentration of oxygen relative to C_4F_8 results in a reduction in the etch rate and the depletion of carbon from the CDO substrate. The conditions for sample T6 illustrate that presence of C_4F_8 in the feed gases is not in itself sufficient to ensure efficient etching. The presence of a thin fluorocarbon film on the surface plays a critical role in determining the etch rate. Samples T2 to T5 have significantly different gas ratios, yet the etch rate is constant. This would suggest that the fluorocarbon layer on the surface mediates the etching reactions as well as limiting the extent of carbon depletion from the CDO film.

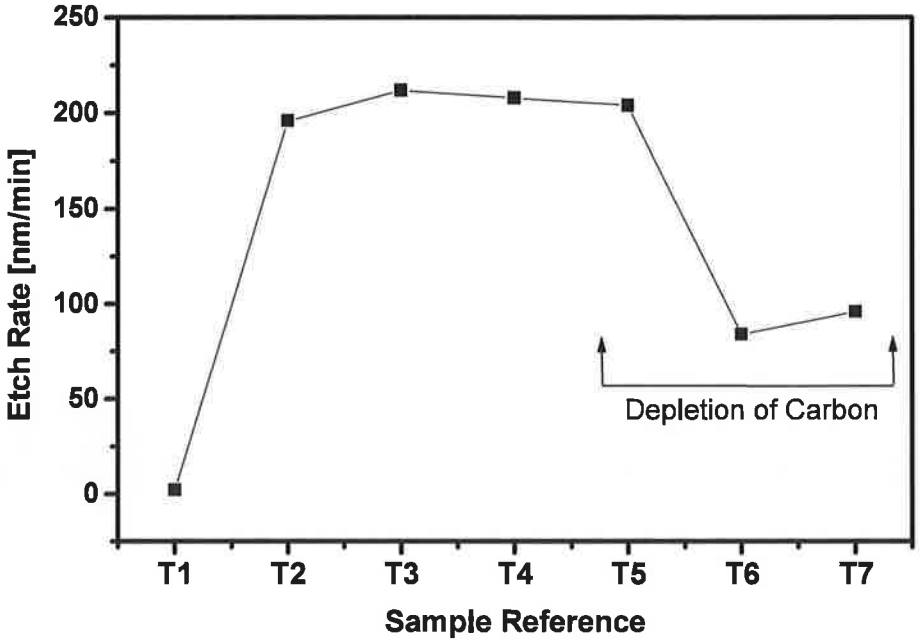

Figure 6.4: Etch rates of plasma treated samples as a function of feed gas ratios.

6.3 Suppression of carbon depletion from carbon-doped low-*k* dielectric layers using industrial plasma parameters.

Table 6.2 summarises the range of plasma conditions and etch chemistries used on the CDO films in this set of experiment in the Lam 9100 etcher. The plasma conditions P1 led to the formation of a thick fluorocarbon layer on the surface of the underlying CDO.

Process	upper power	lower power	O_2 flow [sccm]	C_4C_8 [sccm]	Ar [sccm]	Pressure [mbar]
P0	0	0	0	0	0	0
P1	1200	600	15	45	300	45
P2	600	600	45	45	300	45
P3	1200	200	15	15	300	15

Table 6.2: Plasma processing parameters used to etch the CDO film

Shown in figure 6.5 are XPS depth profiles of the C *1s* peak in the CDO after the 30 second plasma etch for all of the samples investigated. P0 is the unprocessed film which has a 15% carbon concentration throughout the entire layer. P1 shows a high percentage of carbon prior to depth profiling which is attributed to the presence of a fluorocarbon film on the surface. When the fluorocarbon layer is removed by argon bombardment, the percentage of carbon in the sample at approximately 15% is comparable to the un-etched sample. The depth profile of carbon for processes P2 and P3 both show evidence of significant carbon depletion in the near surface region. Both of these plasma gas mixtures have a 1:1 C_4F_8/O_2 gas ratio at different gas feed rates. There was no detectable fluorocarbon film on either of these surfaces and the fact that the two processes have significantly different lower power levels suggests that the critical factor in determining the formation of the fluorocarbon film is the C_4F_8/O_2 gas ratio. The depth to which the carbon has been depleted in sample P2 is larger than in P3 and this scales with increased lower power which has a direct impact on the incident ion energy and consequently on the etch rate. In general, it was found that the plasma conditions which led to the formation of a fluorocarbon layer on the surface of the CDO resulted in a considerable suppression of the surface carbon depletion.

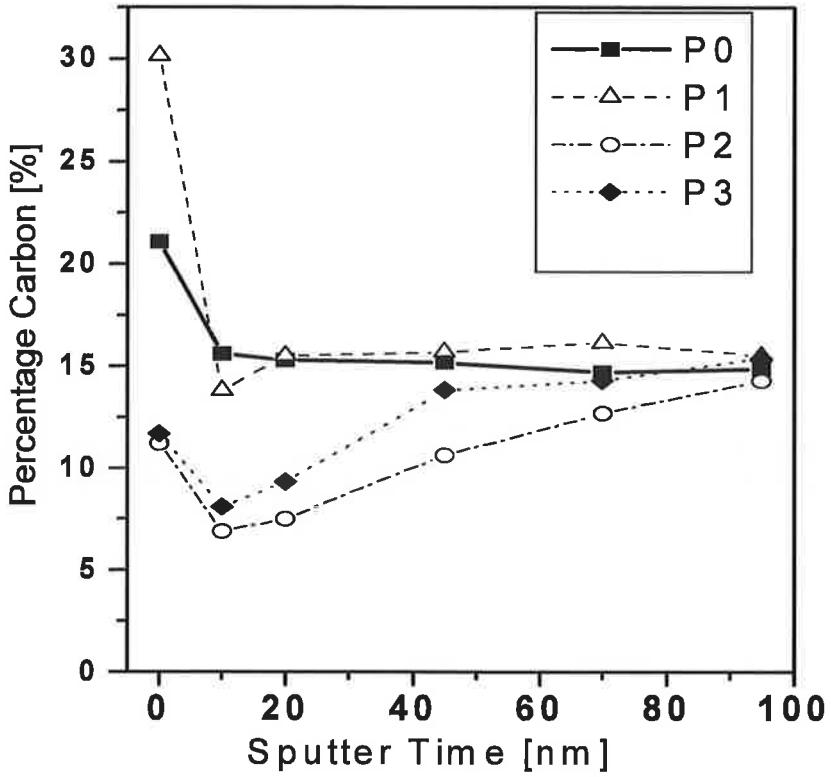

Figure 6.5: Profile of the C *1s* peak as a percentage through the film

SIMS Depth profiles were carried out on all samples, a profile of P1 from table 6.2 is shown in figure 6.6. By looking at the first 5 minutes it is apparent that there is an abundance of carbon and fluorine species on the surface, CF_2 carbon fragments are present in the spectrum. These results compare well with the XPS data. Due to the destructive nature of SIMS bonds of type CF_3 may be broken through the bombarding process, unlike the XPS which can see these fragments.

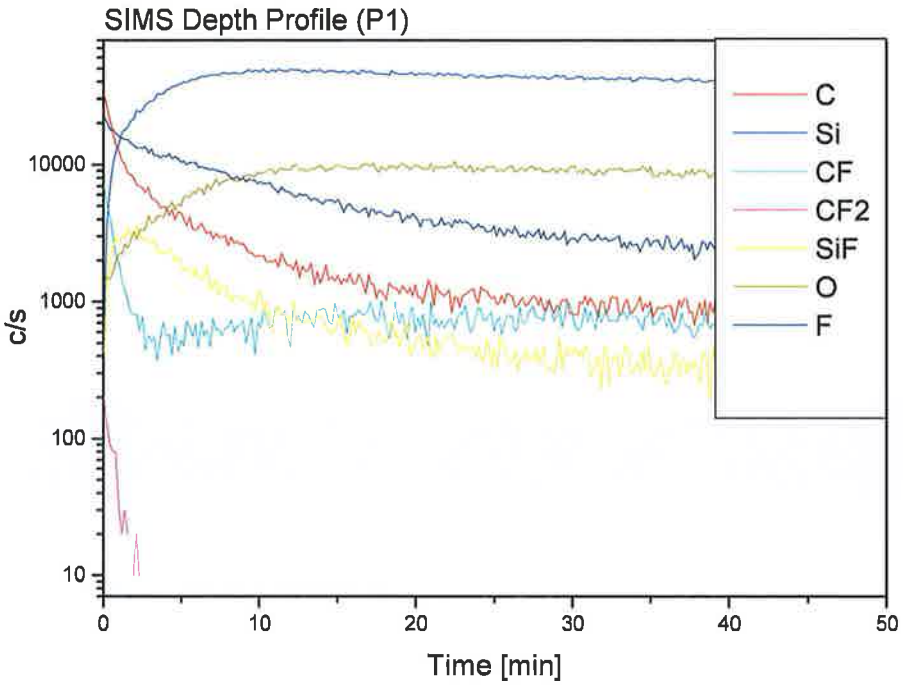

Figure 6.6: SIMS depth profile of process P1

Figure 6.7 shows SIMS carbon depth profiles for the plasma conditions P1, P2, P3 and of the unprocessed wafer (p0) itself for comparative reasons. Sample P2 has the most significant carbon depletion. Sample P3 is also depleted of carbon. These carbon signals increase up to the level of P0 (15%) further into the sample. Carbon depletion can take place up to 100 nm into the sample depending on plasma powers and etch chemistries. The high level of carbon within the CDO of samples P1 is clearly visible which indicates that no carbon has been depleted.

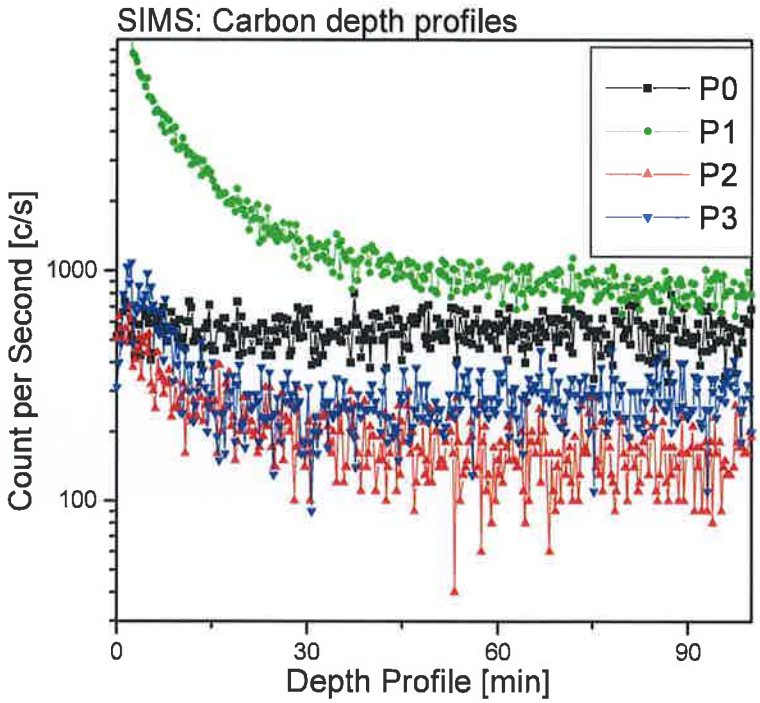

Figure 6.7: SIMS carbon depth profiles showing the depletion of carbon in P2 and P3 and the presence of a CF film on CDO.

Figure 6.8 schematically illustrates the different regimes carried out in this chapter [2]. A total lack of oxygen in the feed gases leads to the situation shown in part A where a thick fluorocarbon film is deposited on the surface of the ULK CDO which hinders etching of the underlying substrate. An oxygen rich plasma results in carbon being depleted from the upper part of the CDO [8, 9] as illustrated in part C and the formation of an SiO_2 like dielectric layer. The situation represented by B shows an optimal oxygen concentration where substrate etching takes place in the presence of a thin fluorocarbon film without resulting in carbon depletion.

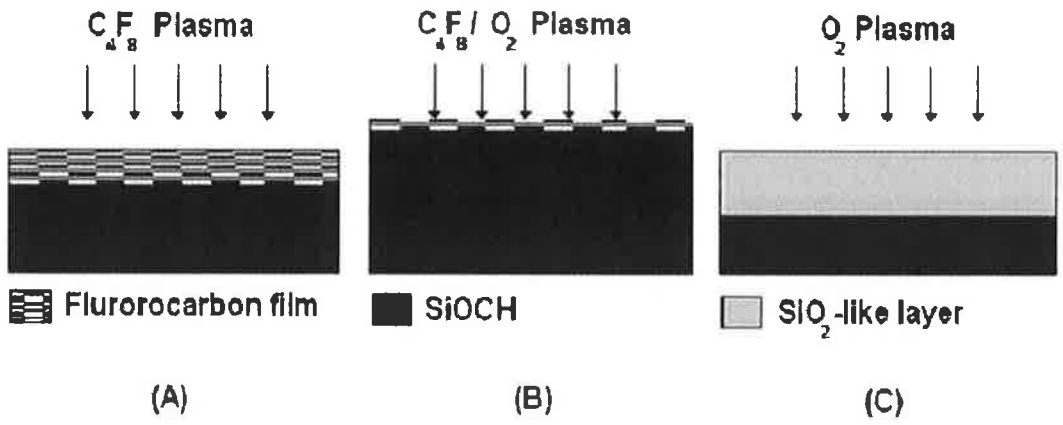

Figure 6.8: Schematically illustrated etch regimes carried out on CDO [2].

6.4 Conclusions

This study illustrates the critical role a surface fluorocarbon layer plays in the etch process of a CDO dielectric layer. Gas ratios which are either oxygen rich or oxygen deficient hinder the etch mechanisms. A complete lack of oxygen results in the formation of a thick fluorocarbon film and no etching. High oxygen concentrations within the plasma chemistry leads to inefficient etching and resulted in the absence of a fluorocarbon layer and can cause up to a 50% reduction in the carbon concentration in the upper part of the low-*k* layer. The thickness of the fluorocarbon film can be controlled by the C_4F_8/O_2 gas ratio and the presence of this film has a impact on the etch rate. During FBPE the presence of surface localised fluorocarbon layers were found to suppress the depletion of carbon from the upper part of the CDO film. The formation of the fluorocarbon layer is strongly correlated to the gas chemistry ratios and not directly to the power levels within the plasma. Large fluorocarbon layers are not necessary to prevent carbon depletion from the CDO film thus enabling an optimisation of the etch rate.

6.5 References

1. T. E. F. M. Standaert, M. Schaepkens, N. R. Rueger, P. G. M. Sebel, G. S. Oehrlein, and J. M. Cook, J. Vac. Sci. Technol. A 16 (1998) 239
2. T.E.F.M. Standaert, C.Hedlund, E.A.Joseph, G.S.Oehrlein and T.J.Dalton J. Vac. Sci. Technol. A 22 (2004) 53.
3. M. Schaepkens, T.E.F.M. Standaert, N.R. Rueger, P.G.M. Sebel, G.S. Oehrlein, J.M. Cook, J. Vac. Sci. Technol. A 17 (1999) 26.
4. R.A.H. Heinecke, Solid-State Electron. 18 (1975) 1146.
5. J.W. Coburn, J. Appl. Phys. 50 (1979) 5210.
6. V. Yanev, S. Krischok, A. Opitz, H. Wurmus, J. A. Schaefer, N. Schwesinger and S. -I. -U. Ahmed, Surface Science, 1229 (2004) 566.
7. I. Reid and G. Hughes. Semi. Sci. Technol. 21 (2006) 1354.
8. D. Shamiryan, M. R. Baklanov, S. Vanhaelemeersch, and K. Maex J. Vac. Sci. Technol. B 20 (2002) 1923.
9. D. Shamiryan, K. Weindner, W.D. Gray, M. R. Baklanov, S. Vanhaelemeersch, and K. Maex Micro. Eng. 64 (2002) 361.

Chapter 7: Electronic structure of organic semiconductors: tetraphenylporphyrin (TPP) and metal tetraphenylporphyrins (MTPP)

7.1 Introduction

Organic semiconductors are the subject of intense study due to the challenge they pose to our understanding of the physical properties of complex solids and due to technological interest in developing carbon-based electronic devices [1]. Recent studies of transition metal tetraphenylporphyrin (TPP) have investigated their use in structures such as chemical sensors [2], organic semiconductors [3] and opto-electronic device fabrication [4]. Accurate determination of the electronic structure of thin film organic semiconductors is a prerequisite to developing a comprehensive understanding of these electronic materials. Porphyrins form an important class of organic semiconductors due to the ease with which a diverse set of cations can bond to the porphyrin ligand. The structural and optical properties of TPP have been extensively studied using visible light absorption spectroscopy, Fourier transform infrared spectroscopy and scanning tunnel microscopy [5, 6, 7, and 8]. XPS studies have been carried out also [9, 10]. Theoretical calculations on the electronic structure of MTPP have been investigated [11]. However, to date, detailed x-ray spectroscopic studies of the electronic structure of TPP have not been carried out and consequently there is little experimental information of element specific densities of states or the electronic structure near the Fermi level (E_F).

We report here the results of a study of the electronic structure of free base TPP, CoTPP, NiTPP, ZnTPP and CuTPP using a variety of synchrotron radiation soft x-ray spectroscopies. The probes used were soft x-ray emission spectroscopy (XES), soft x-ray absorption spectroscopy (XAS), and x-ray photoemission spectroscopy (XPS). The TPP samples studied were in the form of thin films grown in-situ via ultra-high vacuum organic molecular beam deposition. The element specific valence and conduction band electronic structure was measured using XES and XAS respectively, while the element specific core levels were measured using a commercial XPS. Density functional theory (DFT) calculations

were carried out by James Downes. DFT calculations were performed for an isolated CuTPP molecule. The calculations used a general gradient approximation GGA:PW91 exchange-correlation functional and a spin-unrestricted ll-electron model. Parallel DGauss under Ab Initio CAChe (Fujitsu) was used to perform the calculation in a dual processor Intel Xeon machine. The calculated PDOS presented here have been broadened to account for instrument resolution and core hole lifetime effects to facilitate comparison to the measured CuTPP spectra. The experimental spectra were compared to the calculated partial density of states (PDOS), and good agreement was found. A schematic diagram of two types of TPP molecules investigated is presented in figure 7.1 and shows the differences in structure between the free base TPP and the metal TPP. A range of different metal centred TPP molecules have been measured in this study but detailed data will only be presented for the CuTPP.

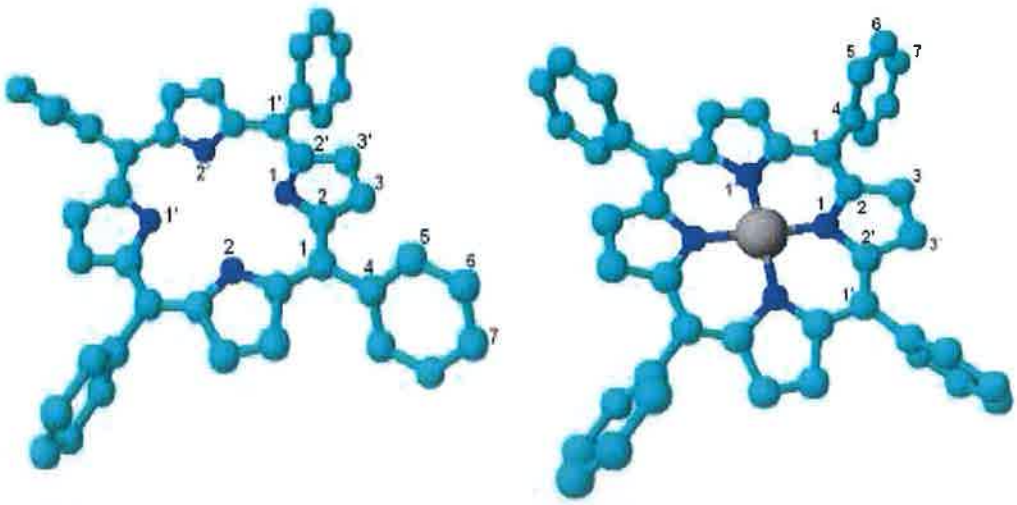

Figure 7.1: Schematic drawing of the TPP molecule (Left) and MTPP molecule (Right). H atoms are omitted for clarity. C and N atoms are represented by light and dark blue, respectively.

7.2 The electronic and chemical structure of TPP and CuTPP.

The carbon atoms reside in seven distinct sites in TPP and CuTPP. These C sites are marked C_1 through C_7 on the schematic drawing of the CuTPP molecule presented in figure 7.1. These sites can be divided into two principal groups with different chemical environments: six C sites with the C atom having only other C as the nearest neighbour, e.g such as on the benzene-like outer rings and the other group with one C site on the inner pyrrole ring where the C atom has an N as a nearest neighbour.

Figure 7.2 shows the N *1s* XPS spectrum of the so-called-free base TPP which has no metal centre. The XPS system used is outlined in section 3.2. The two peaks represent protonated and unprotonated nitrogen, with an area ratio of 1.22 which is similar to other studies carried out on the same material [9, 10, 12]. The difference of the peak intensity is attributed to a weak satellite peak associated with the lower energy peak at 397.5 eV that overlaps with the higher binding energy peak at 399.5 eV. The FWHM is 1.38 eV, the associated satellite peak is 3.2 eV at higher energies.

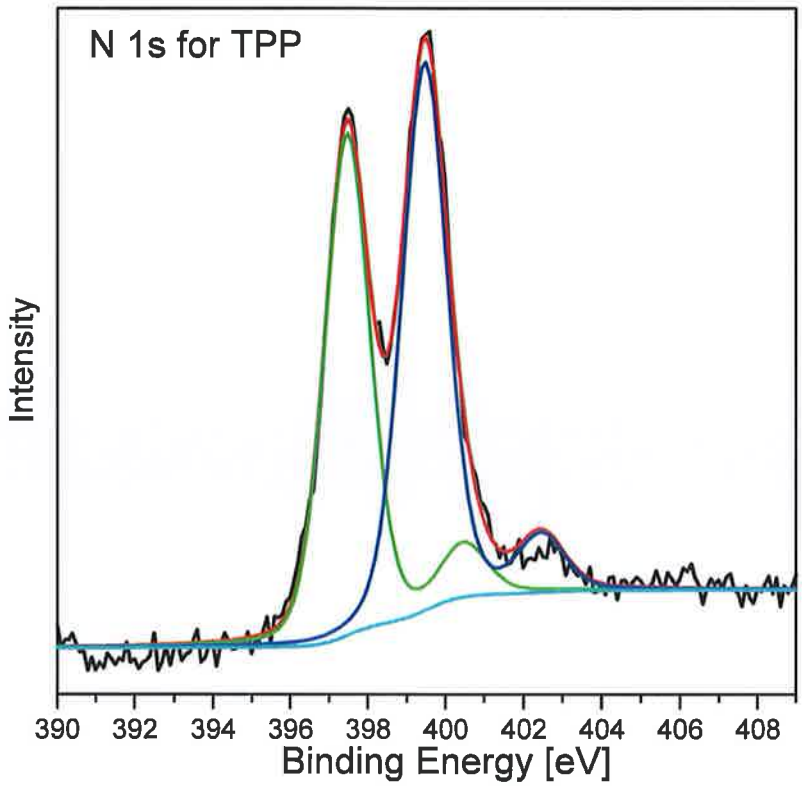

Figure 7.2: N *1s* XPS from TPP.

Figure 7.3 presents an XPS measurement of the N *1s* level in the CuTPP. XPS measurements indicate that all four metal-N bonds in metalloporphyrin molecules are equivalent [9, 10, 13, 14]. We observe a main feature at 398.3 eV, the asymmetry of the peak at higher binding energy is attributed to a π-π* satellite feature at 399.8 eV. This observation is attributed to the paramagnetic nature of CuTPP which is one of a number metalloporphyrins to exhibit this feature [15].

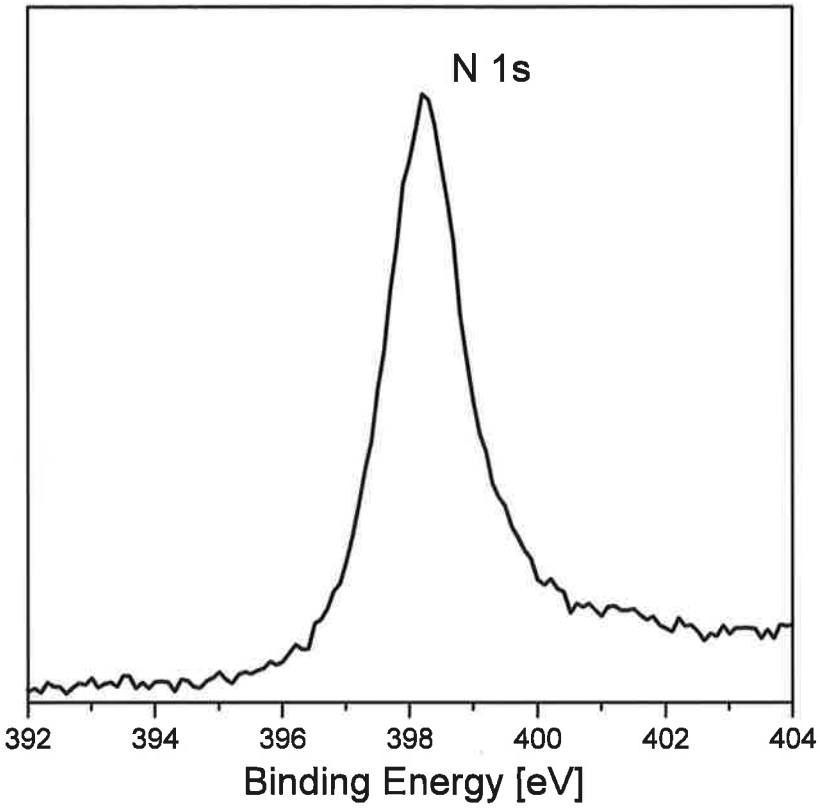

Figure 7.3: N *1s* XPS from CuTPP

Figure 7.4 presents the C *1s* core level electronic structure of CuTPP as measured by XPS using a Mg K_α laboratory source as described earlier in section 3.2. This C *1s* core level has a very similar profile when compared to that of the free-base TPP. The main peak at 284.3 eV is a composite arising from various carbon atoms including eight carbon atoms bonding with a nitrogen atom in the compounds. With all of the TPP's, a splitting of the peaks arising from different carbons was too small to be detected as separate peaks, these results compare well to *Niwa et al* [10]. Measurements on MTPP powders showed that this result was not attributed to the thermal deposition process as these samples showed the same result. The peak at 287.1 eV is assigned to a satellite peak associated with the main C *1s* feature.

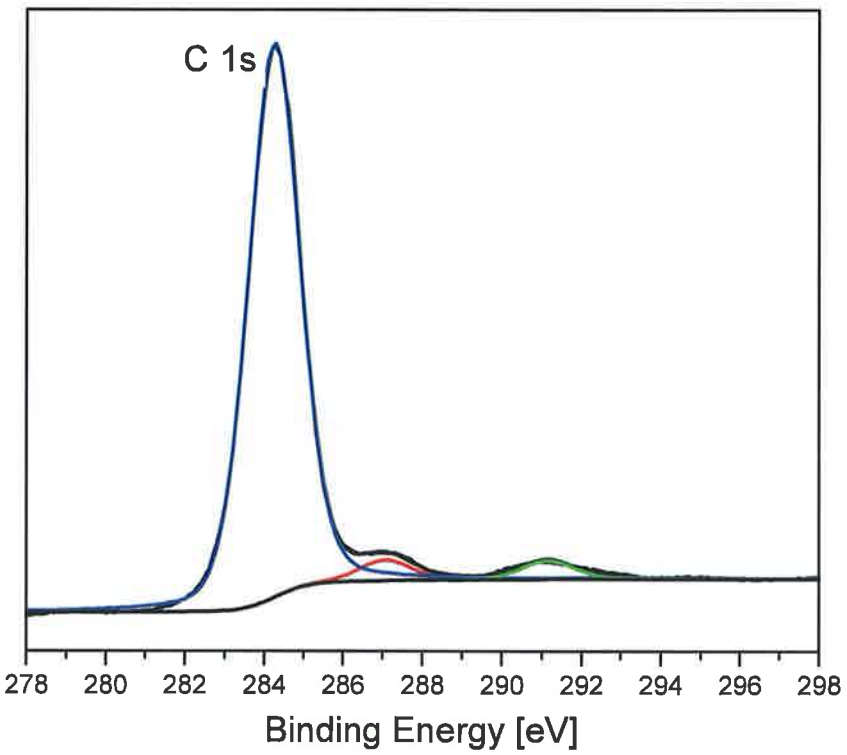

Figure 7.4: C *1s* XPS from CuTPP

Figure 7.5 presents the Cu *2p* core level. Two copper oxidation states can be seen in the figure below. The main peak is at 935.1 eV with spin orbit splitting of 19.8 eV. These spectral features correspond to $2p_{3/2}$ and $2p_{1/2}$ from Cu^{2+} and both component peaks have a broad shake up satellite associated with them approximately 9 eV higher binding energy than the main peak position. These energy positions are similar to those found on copper phthalocyanine [16]. A lower energy peak at 932.7 eV is also seen with a corresponding peak at 953 eV this could be associated with Cu^{1+} oxidation states [17].

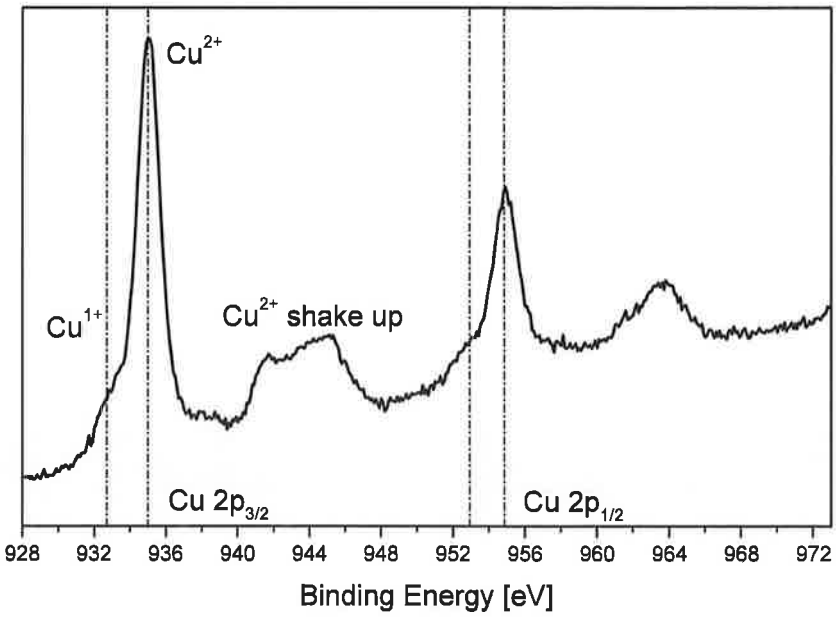

Figure 7.5: Cu *2p* XPS from CuTPP

High resolution XES measurements require a small photon spot (circa 40 μm) with a high photon flux (10^{13} ph/s) on the sample, and long collection times. As mentioned in chapter 4 this combination can lead to considerable beam induced damage in organic systems. This issue has been solved by continuously translating the films in front of the beam (at 40 μm/s) as the spectra are being recorded. Figure 7.6 shows the C K_α XES spectrum reflecting the C *2p* PDOS from both a stationary and continuously translated TPP film. The excitation energy was 294 eV and is well above the absorption threshold for the C *1s* states. The feature at 294 eV visible in both spectra is elastically scattered light. Significant differences in the measured electronic structure of identical films when stationary or translated are visible in figure 7.6. These spectra will be discussed in more detail later.

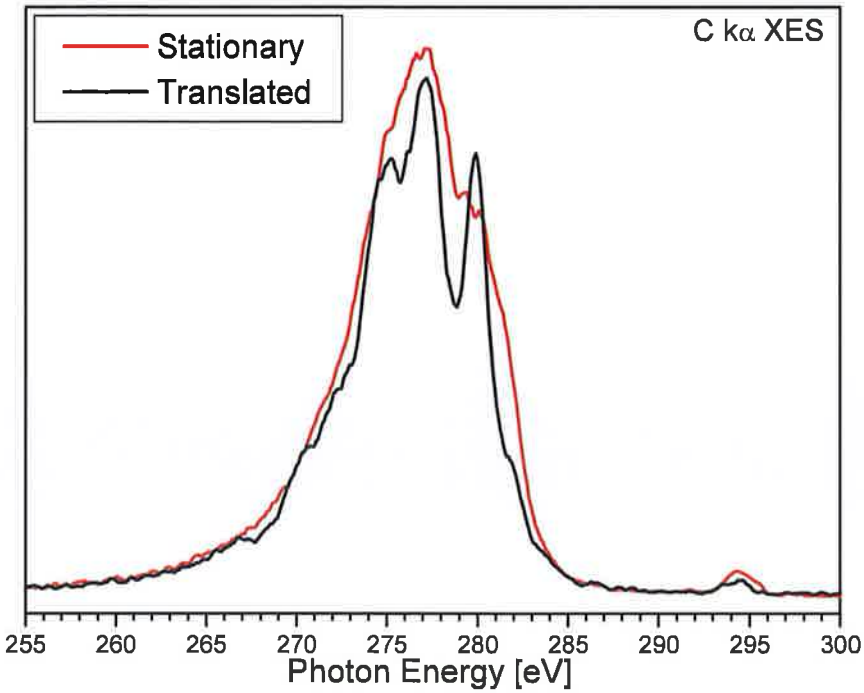

Figure 7.6: Comparison of non-resonant C K_α XES spectra reflecting the C *2p* PDOS for both stationary and translated films of CuTPP.

Figure 7.7 presents the C *K*-edge XAS spectrum from CuTPP, and a number of well defined absorption features can be observed. These features are due to transitions between occupied C *1s* core states (as measured by XPS and shown in figure 7.4) and unoccupied conduction band states. The peak marked 'a' corresponds to the carbon site of C_1, C_2 and C_3. Peak 'b' is predominantly due to the ring carbon sites C_4, C_5, C_6 and C_7. The assignment of the peaks 'a' and 'b' are clear from the DFT calculation carried out. There are some sites in-between peaks 'a' and 'b' which are not evident from the XAS spectra however they can be seen from the theoretical calculation later.

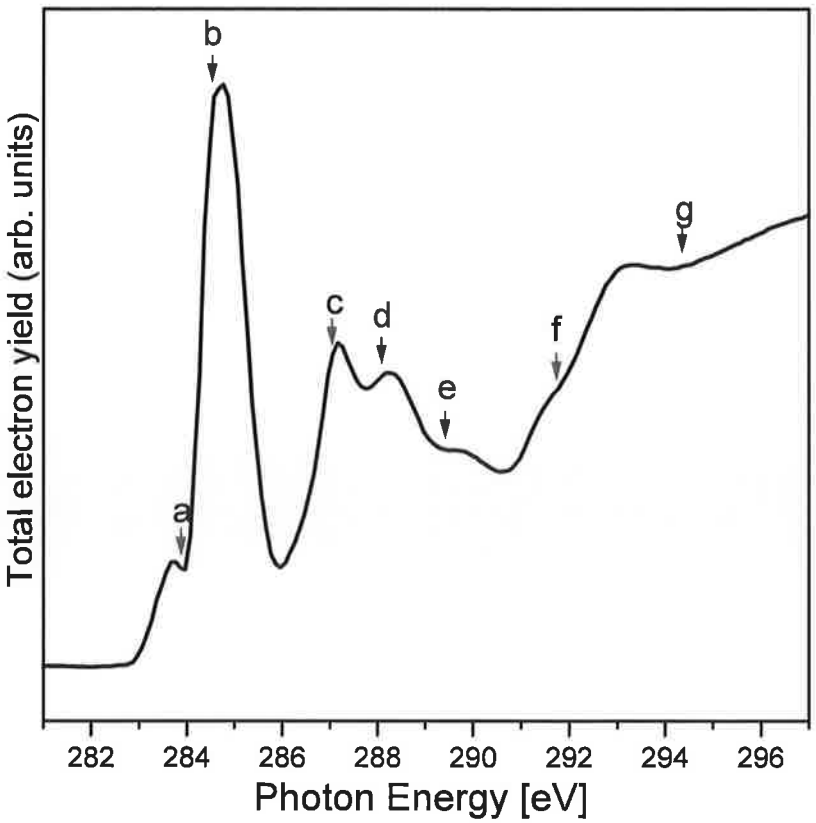

Figure 7.7: C *K*-edge x-ray absorption spectrum CuTPP. The photon energies labeled (a)-(g) are those used to excite the x-ray emission spectra in figure 7.8.

Figure 7.8 presents a series of C $K\alpha$ XES spectra from CuTPP as a function of incident photon energy near the C *K*-edge. In order to resonantly populate unoccupied orbitals, excitation energies used for RSXE were chosen from the features observed in NEXAFS. The excitation energies used to excite these spectra are marked on the C *K*-edge XAS spectrum presented in Figure 7.7. The XES spectra have been normalized to uniform maximum peak height, and offset vertically for clarity. The emission spectra are labeled by excitation energy and corresponding NEXAFS feature. The first six correspond to NEXAFS features (a) through (f). The excitation energy (g) is at the highest incident photon energy (294.4 eV) the excitation is far above threshold, and holes are created on both the ring and pyrrole C atoms. The associated emission spectrum (g) reflects the combined C *2p* PDOS from both the ring

and pyrrole sites. Direct recombination peaks (near-elastic scattering) are seen in each spectrum. The spectrum marked "a", recorded at $h\nu_{exec}$ = 284 eV corresponds to the transition of electrons from the C *2p* valence band states into core holes on the pyrrole C sites.

As the excitation energy in increased, the elastic peak naturally moves to higher energy, and the PDOS features remain at constant emission energy. Well defined features in the valence band PDOS are observed. However, the relative intensity of the main PDOS features changes, and new structures appear at the top of the valence band. Feature (i) at 280 eV consists of the uppermost states of the main manifold of states contributing to the valence band of the molecule. These spectral features have been assigned to a_{1g}. As the excitation energy is increased, structure is seen to emerge between 281 eV and 284 eV. Two neighboring features at 281.2 (ii) and 282.2 eV (iii) are clearly visible in spectra (c) to (g). These features have been assigned as $a_{2u,}$ a_{1u} and b_{1g} (HOMO) to *1s* ring (ii) and pyrrole (iii) site transitions respectively. The onset of (iii) only at higher excitation energies suggests it originates from the same occupied orbital as (ii). Spectral weight is also present at (iv), approximately 2 eV above the HOMO to pyrrole *1s* feature. This is attributed to the de-excitation of a LUMO core-hole exciton state that involves the pyrrole *1s* level. This feature sits at the *1s* pyrrole to LUMO energy difference, less the excitonic binding energy.

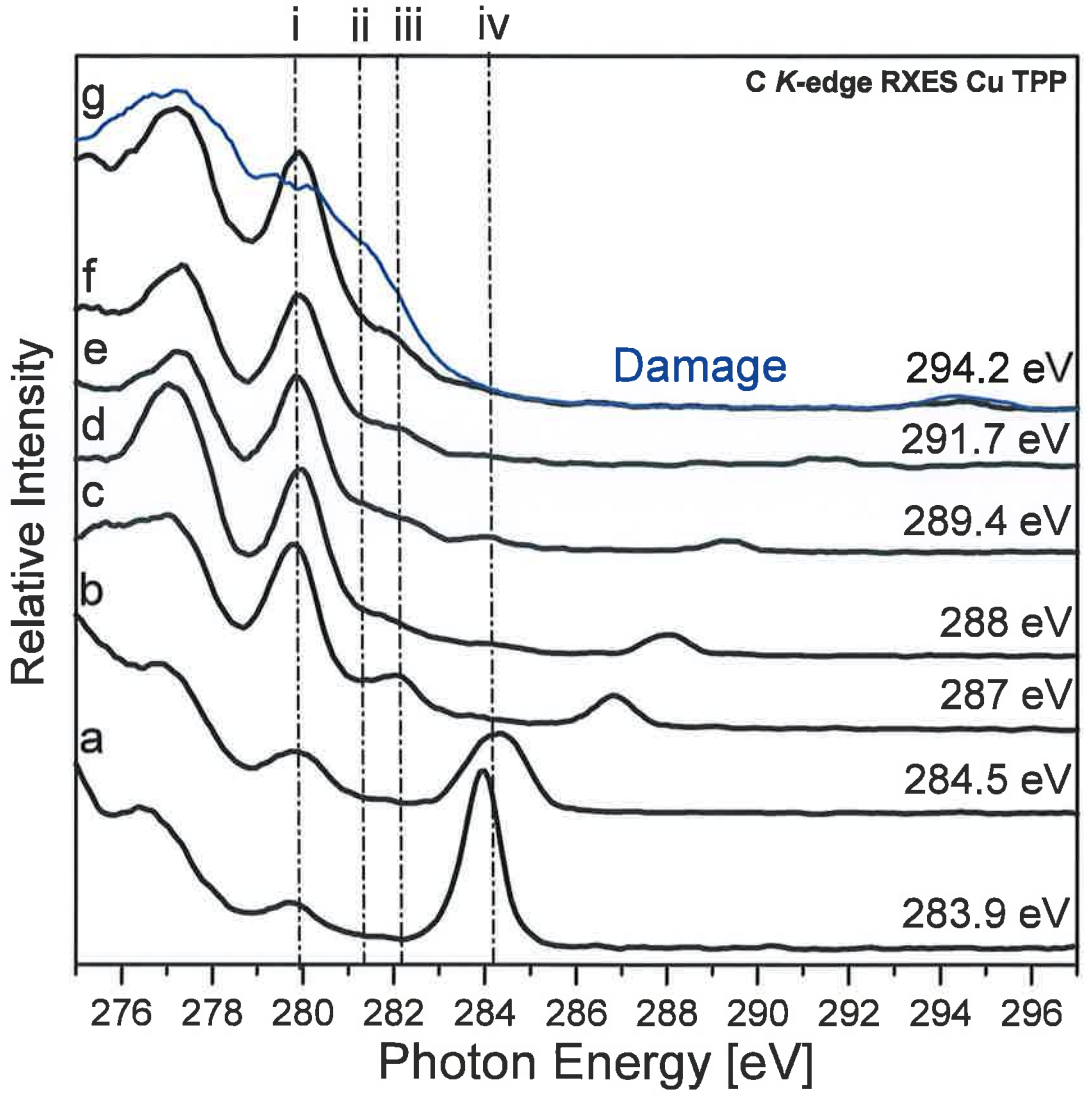

Figure 7.8: C K_α XES spectra from CuTPP as a function of incident photon energy.

The full results of the DFT calculation are presented as chemical site-projected PDOS in figure 7.9. The sum of *s*-, *p*- and *d*-character contributions at each chemical site, the site-local total DOS, is also shown. The results show that the occupied orbitals near the top of the valence band are derived from the overlap of Cu *d*-character and TPP *p*-character states.

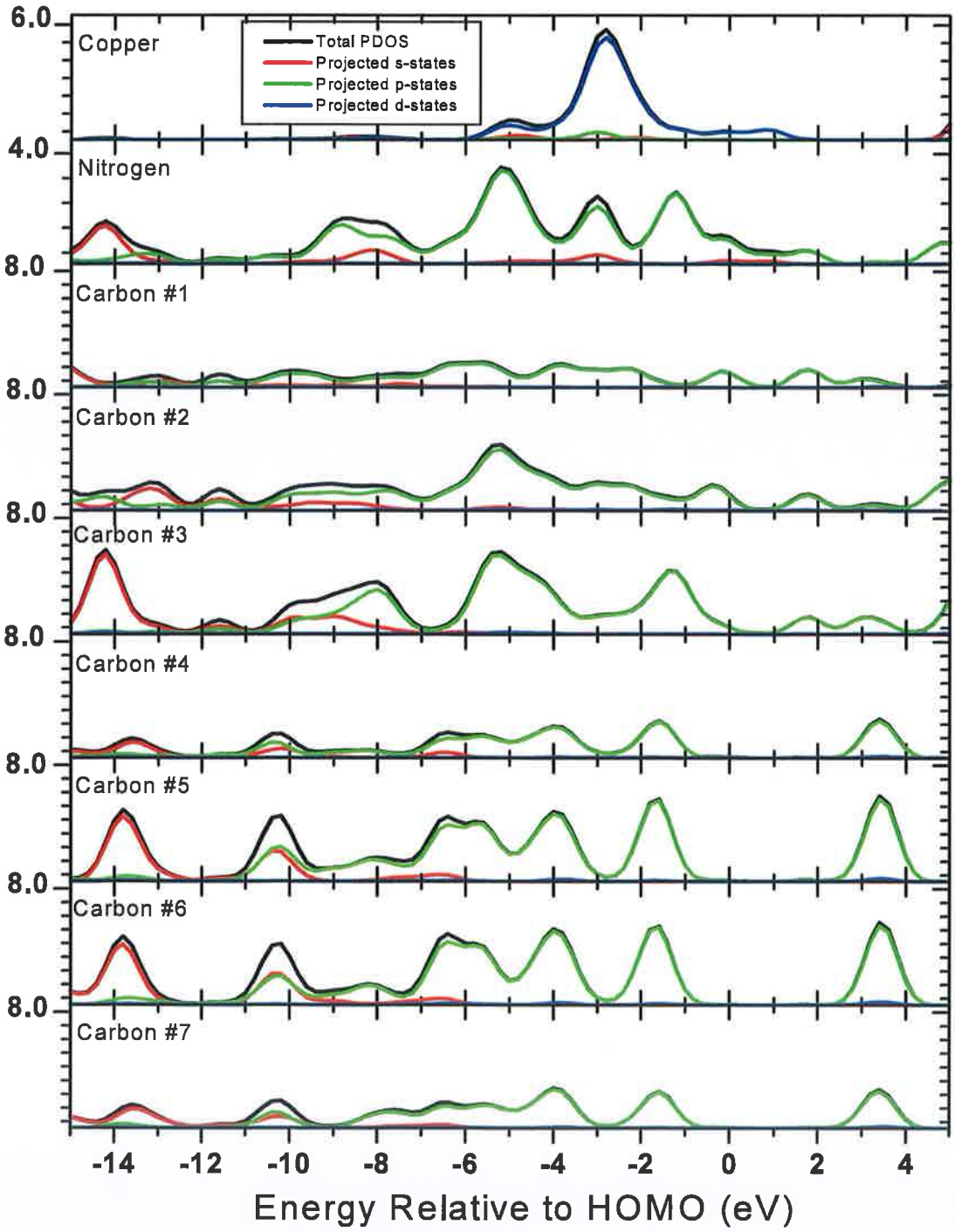

Figure 7.9: Calculated s-, p-, d- character projected, and total density of states for each unique chemical site in CuTPP

Figure 7.10 presents a direct comparison between this XES spectrum reflecting the occupied C *2p* PDOS, the C *K*-edge XAS spectrum reflecting the unoccupied C *2p* PDOS, and the

results of a DFT calculation. The calculated C *2p* PDOS presented in figure 7.10 is the sum of that associated with the seven discrete C sites that are shown in figure 7.9, the calculated C *2p* PDOS is dominated by three intense features. The energy scale of the calculated PDOS has been multiplied by a scale factor of 1.2 to account for the energy compression inherent to DFT calculations [11]. This scale factor is determined by comparing the energy separation of the three primary features in the XES spectrum with that of the equivalent features in the calculated PDOS. With this scaling factor, the agreement between the measured XES spectrum and the calculated occupied C *2p* PDOS is excellent for the three primary features, and likewise, we observe excellent agreement in terms of the number and energy separation of the features between the measured XAS spectrum and the calculated unoccupied C *2p* PDOS.

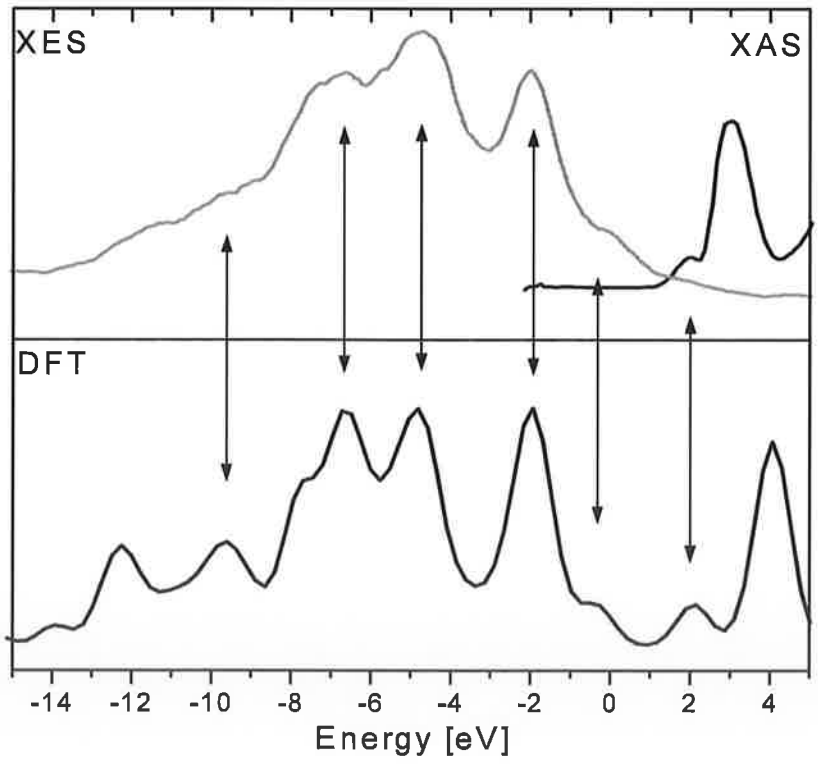

Figure 7.10: Comparison of C *K*-edge XES and XAS measurements to DFT calculation of carbon p-projected PDOS. The calculated PDOS is the sum of that from the ring and pyrrole carbon sites. The XES spectrum is excited by 294.1 eV photons. The HOMO position is set as the zero point of the energy scale.

We now turn to consideration of the N *2p* derived PDOS in CuTPP. There is only one N site present in the chemical structure of CuTPP which means that all the N are equivalent in electronic structure. As shown in the photoemission spectrum in figure 7.3. The N *K*-edge XAS spectrum is presented in figure 7.11. It consists of two well defined features near the absorption edge, marked "a" and "c", as well as a series of higher energy features. These features can be assigned to transitions from the N *1s* states to the LUMO states of N character. The four spectral features a, b, c and d correspond to excitations to π^* orbitals with the assignment of e_g, b_{2u}, e_g and a_{2u} respectively. The spectral feature e and f are a result of $1s \rightarrow \sigma^*$ excitations These spectral feature compare well with other reported studies of ZnTPP [18 , 19] .

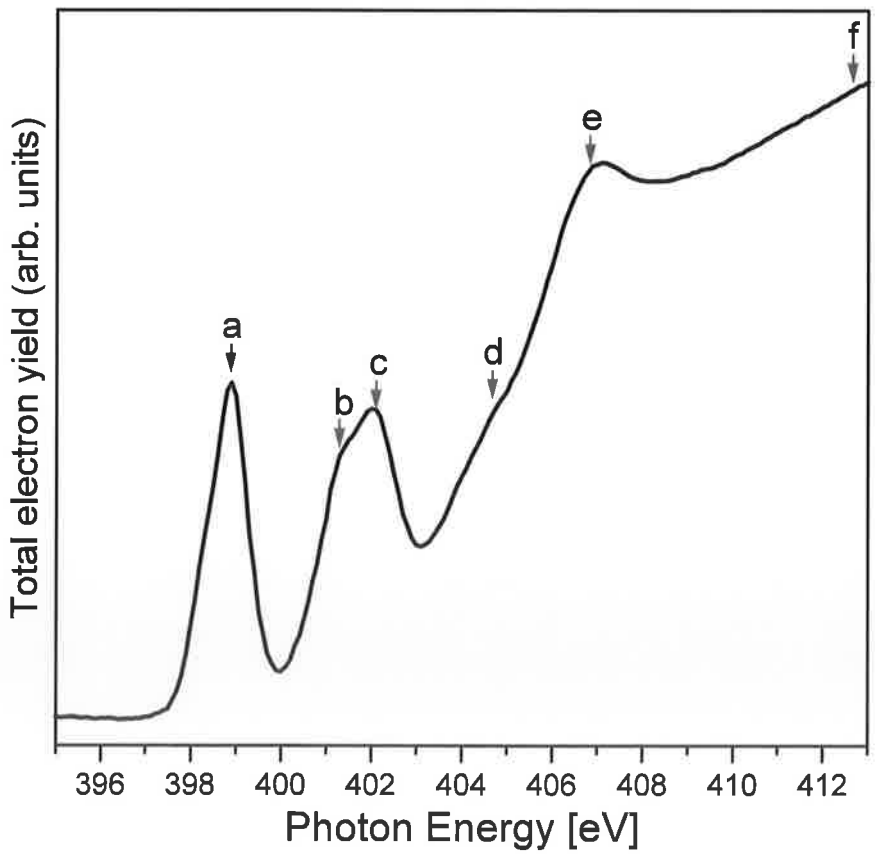

Figure 7.11: N *K*-edge soft x-ray absorption spectrum for CuTPP. The excitation energies labeled (a)-(c) are used in the XES measurement of figure 7.12.

A series of N $K\alpha$ XES spectra excited at the photon energies marked a, b, and c on figure 7.11 were recorded; these XES results are presented in figure 7.12. Minimal variation in the spectral shape is observed as a function of incident photon energy, implying that the emission is dominated by PDOS features. This is confirmed by comparison to the results of the DFT calculations. Spectra "f" at an excitation energy of 412.7 eV illustrates the effects of beam damage taken place when the CuTPP sample is not translated. When comparing the spectral features to DFT calculations carried out by *Liao et al* good agreement is found [11]. The spectral feature at 395.2 eV (i) corresponds to the e_g and b_{2g} states. The spectral feature at 396.4 eV (iii) corresponds to the 1_{eg} and b_{2u} states. Both of these features are clear in RSXE spectra "a", However when the excitation energy is increased these spectral features are suppressed with the emergence of the spectral feature at 395.8 eV (ii) corresponding to the a_{1g} states. Spectral weight at 397 eV (iv) is present in all spectra and is due to a_{2u} and a_{1u} states. The HOME b_{1g} state is represented at 398.2 eV (v) however this state is not clearly visible in the experimental data.

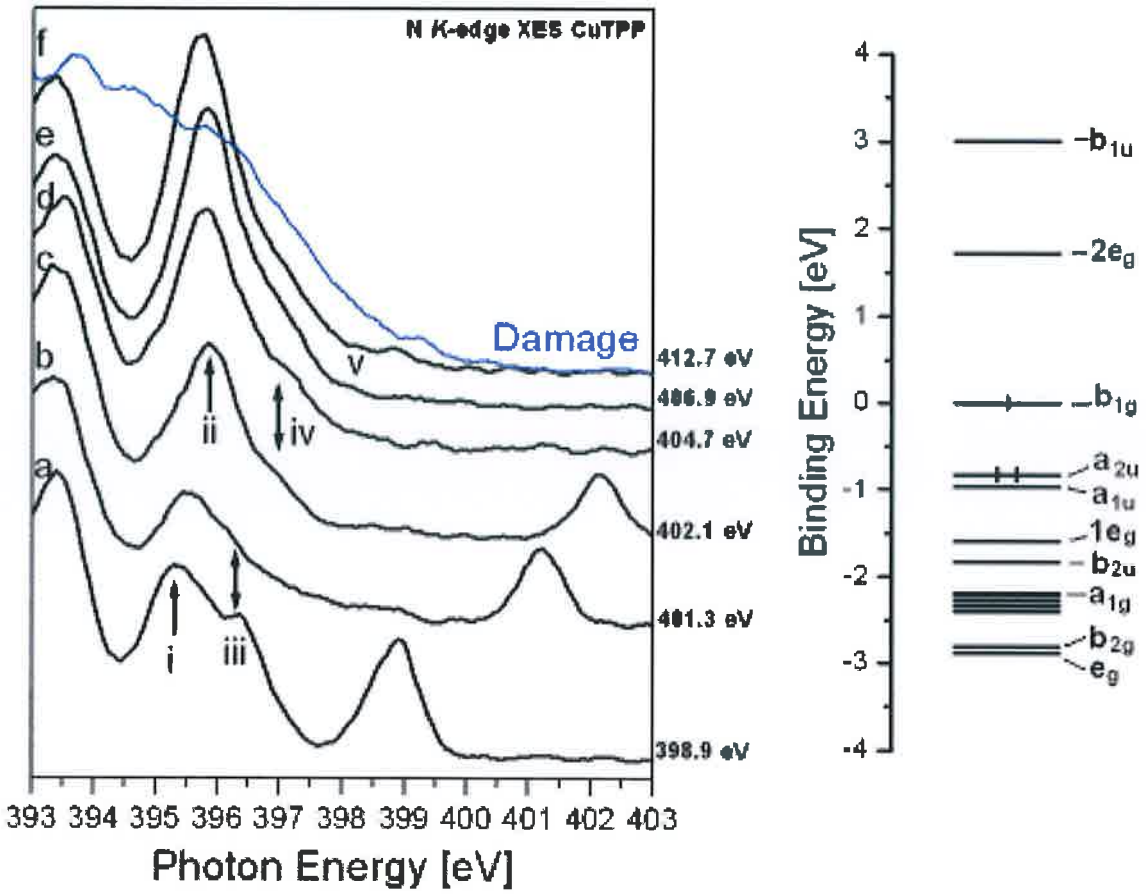

Figure 7.12: Left panel: Series of XES spectra from CuTPP showing emission from states in the valence band. Right panel: Electronic structure of CuTPP as predicted by DFT calculations [11], Note that the DFT calculation energies have been rigidly shifted such that the binding energy of the b_{1g} HOMO state is set to zero, allowing comparison to the measured excitation energies in the RSXE spectra.

Figure 7.13 presents a comparison between the calculated N *2p* PDOS and the N K_α XES spectrum (recorded with $h\nu_{excite}$ = 414 eV) and the N *K*-edge XAS spectrum. A rigid scaling factor of 1.2 is applied to the calculated energies to align them with the measured spectral features which is the same scaling factor applied to the C *2p* PDOS in figure 7.10.

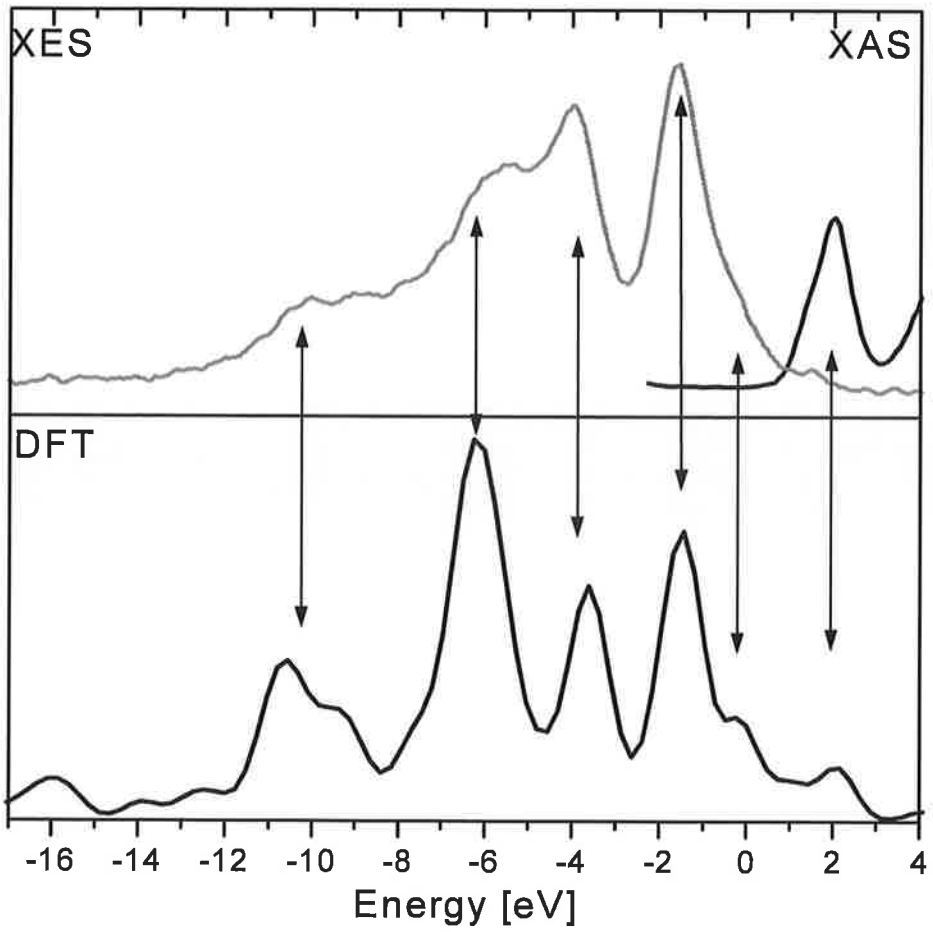

Figure 7.13: Comparison of N *K*-edge XES and XAS measurements to DFT calculation of nitrogen *2p* PDOS. The calculated PDOS is the sum of that from the nitrogen sites. The XES spectrum is excited by 415 eV photons. The HOMO position is set as the zero point of the energy scale.

7.3 Comparative study on free base and metal TPPs.

This section is a comparative study between the various TPPs investigated in this study. The carbon and nitrogen core level spectra are not shown in this section as all the MTPP spectra are the same as in figures 7.3 and 7.4. Presented in figure 7.14 are the XPS *2p* core levels of Co, Zn and Ni for the metal TPPs. The binding energy for the Co and Ni spectral features are consistent with other studies carried out on the same material by *Scudiero et. al.* [8]. The

binding energy of the Co $2p_{3/2}$ can be found at 780 eV this indicates that it is in a Co^{2+} species state [20]. Metal ions in metalloporphyrins usually adopt the +2 oxidation state [21]. The Co *2p* has a spin orbit splitting of 15.7 eV between the $2p_{3/2}$ and $2p_{1/2}$ levels, with a shake up satellite at a binding energy of 7.8 eV higher. The Ni $2p_{3/2}$ can be found at 855.5 eV. The spin orbit splitting of the Ni *2p* is 17.2 eV with shake up satellites 7.5 eV at higher binding energy. The Zn $2p_{3/2}$ is at a binding energy of 1022 eV with spin orbit splitting of the Zn *2p* at 23.2 eV with shake up satellites 7 eV at higher binding energy. The relatively large feature at lower binding energy than the main $2p_{3/2}$ of Co and Zn TPP's, is attributed to an intrinsic feature of the Mg x-ray source.

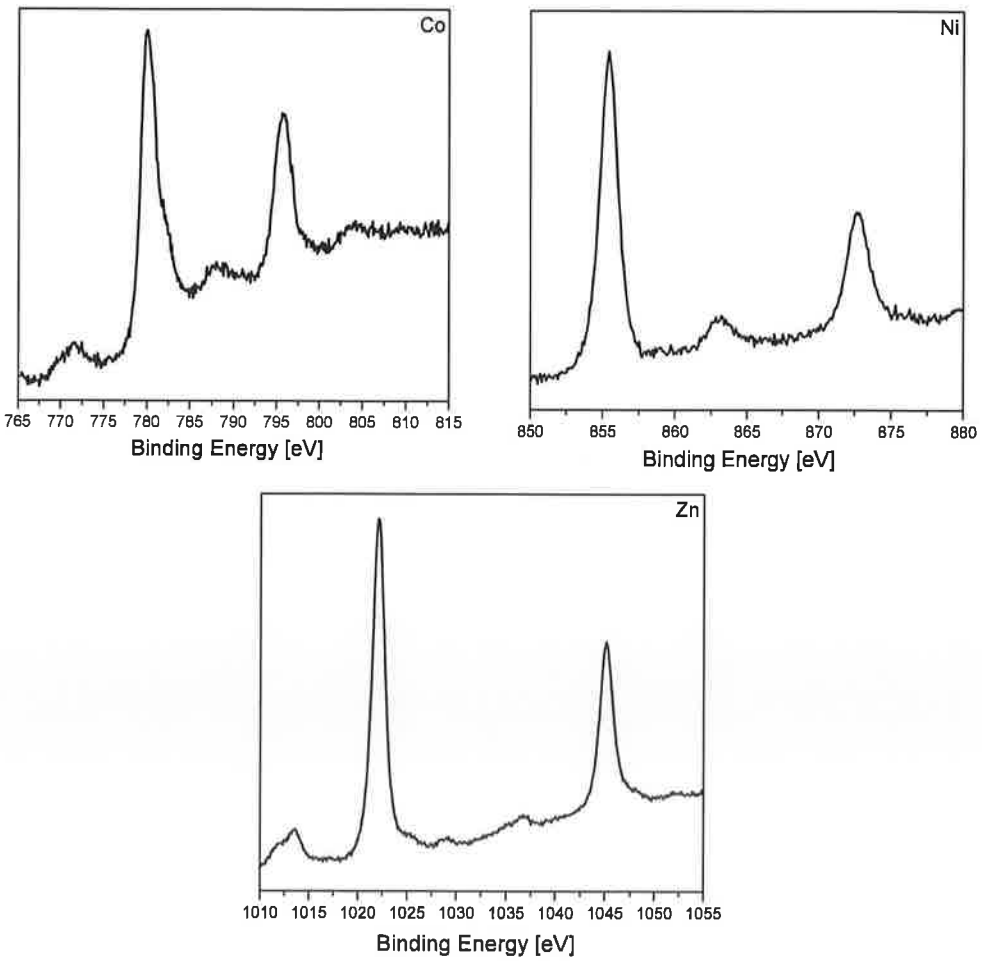

Figure 7.14: The Co, Zn and Ni *2p* core level spectra for the MTPP's

Shown in figure 7.15 are the N *K*-edge NEXAFS spectra of unoriented TPP, CoTPP, NiTPP and Zn TPP deposited on Si substrates. Their peak energies are listed in table 7.1. The general shape of all the NEXAFS spectra is roughly the same; there are four peaks at lower photon energies (a,b,c,d) with two spectral features at higher energies (e,f) these features are consistent with other XAS spectra on the same molecules [18, 19]. These features correspond to excitations to π^* and σ^* orbitals respectively deduced from the polarisation dependence of absorption intensity carried out by Narioka et al [18].

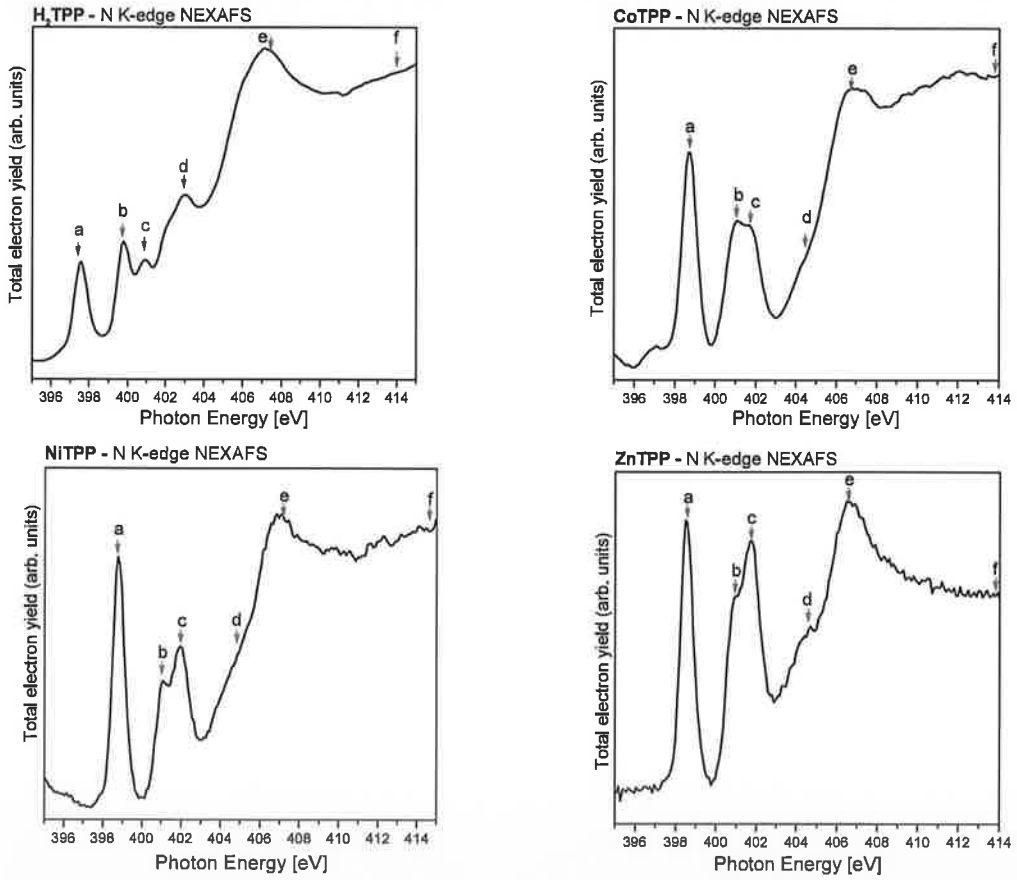

Figure 7.15: N *K*-edge NEXAFS spectra of (a) TPP, (b) CoTPP, (c) NiTPP and (d) ZnTPP

The energy assignments of these features are listed in table 7.1. For the metal TPP's the feature assignments A to D are π * with the following symmetries e_g, b_{2u}, e_g and a_{2u} respectively [18]. However for features A and B in the free base TPP their symmetries are b_{3g}

and b_{1u} for N without H, for features C and D which are assigned to N with H the symmetries are b_{2g} and b_{1u} respectively.

Table 7.1: Energy positions of the features in XAS spectra of the various TPPs

Feature	**Energy [eV]**				**Assignment**
	TPP	**CoTPP**	**NiTPP**	**ZnTPP**	
A	397.6	398.7	398.7	398.5	π *
B	399.7	401	401.1	401	π *
C	400.9	401.7	401.9	401.7	π *
D	403	404.5	405	404.6	π *
E	407	406.7	407	406.6	σ*
F	414	414	414.5	414	σ*

Shown in figure 7.16 are the N K_α soft x-ray emission spectra from TPP, CoTPP, NiTPP, CuTPP and ZnTPP all taken well above threshold at excitation energy around 415 eV. There is a distinct difference between the free base TPP and all the metal TPP structures. This reflects the difference between the photoemission spectra of the N *1s* core levels between the free base TPP and the metal containing compounds that are shown in figures 7.2 and 7.3 respectively. All of the metal TPPs are similar in spectral features with more weight on the peak at 396 eV as the number of electrons increase.

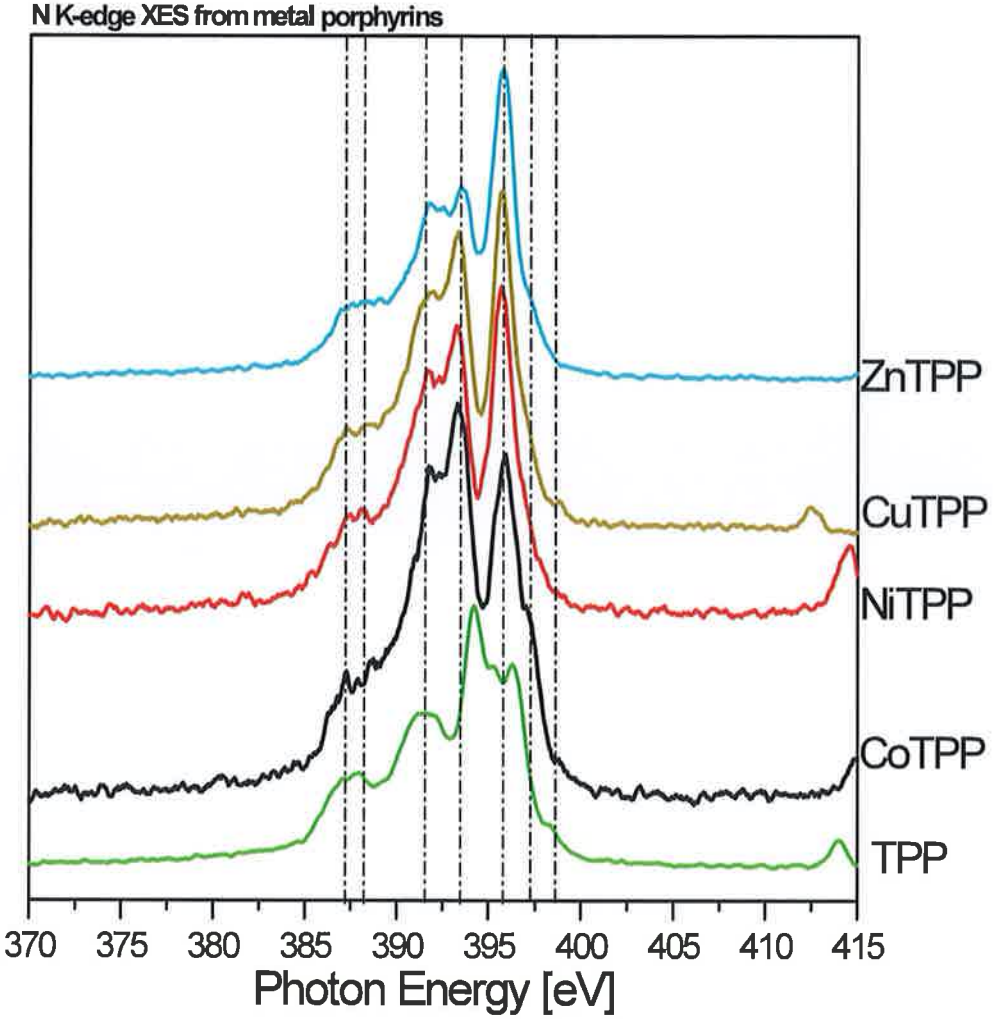

Figure 7.16: N K_α soft x-ray emission spectra from TPP, CoTPP, NiTPP, CuTPP and ZnTPP all taken above threshold at 415 eV.

The same unoccupied features and HOMO state are visible in both C and N NEXAFS and RXES spectra. This allows both sets of spectra to be aligned on the same energy scale, referenced to the HOMO state. A comparison between two resonant C and N K_α XES spectra excited at corresponding features of their respective NEXAFS spectra is shown in figure 7.17. A UPS spectrum measured by *C. Castellarin Cudia et al* [22] is overlaid on the RXES spectra. It is evident from the figure that the HOMO and the feature at -3 eV is made up of C

and N states. The large feature at -5 eV is dominated by C states which are due to the porphyrins ligand. The large peak at -8 eV is due to Zn *3d* emission. Also features at -11.5 eV and -15 eV are due to the Zn. The C and N XES data compares well to the PES spectra by *C. Castellarin Cudia1 et al* [22].

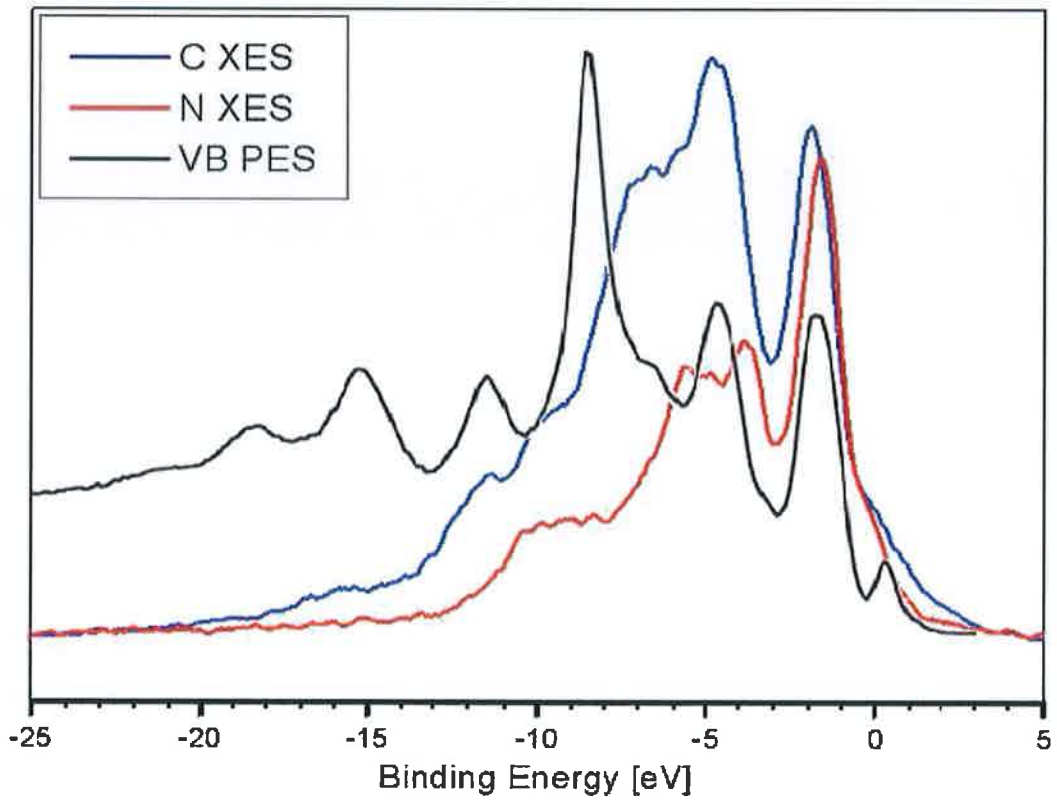

Figure 7.17: A comparison of C and N K_α spectra of ZnTPP taken with an excitation energy well above threshold. A PES spectrum from the paper of *C. Castellarin Cudia1 et al* [22] is superimposed to show the direct correspondence between UPS and XES features.

7.4 Conclusions

The first comprehensive measurement of the occupied and unoccupied electronic structure of the organic semiconductor copper tetraphenylporphyrin, (CuTPP) was undertaken using x-ray photoemission spectroscopy, soft x-ray emission spectroscopy and soft x-ray absorption

spectroscopy. The measured electronic structure was compared to the results of a DFT calculation. The element specific partial density of states for C and N was measured and excellent agreement obtained with the calculated electronic structure. TPP, NiTPP CoTPP and ZnTPP were also investigated using XPS, XAS and XES and a comparative study was carried out. For ZnTPP XES spectra of the partial density of states for C and N compared well with PES data.

7.5 References

1. S. R. Forrest, J. Quant. Elec. 6, 1072 (2000); Chem. Rev. 97 (1997) 1793 .
2. M. Benetti, D. Cannatà, F. Di Pietrantonio, V. Foglietti, E. Verona. Appl. Phys. Let. 87 (2005) 173504
3. H. Imahori, Org. Biomol. Chem. 2 (2004) 1425.
4. R. W. Wagner, J. S. Lindsey. J Am. Chem. Soc. 116 (1994) 9759.
5. D. E. Barlow, L. Scudiero, and K. W. Hipps. Langmuir 20 (2004) 4413.
6. L. C. Xu, Z. Y. Li, W. Tan, T. J. He, F. C. Liu, D. M., Chen Spectrochimica Acta Part A 62 (2005) 850
7. M. M. El-Nahass, H. M. Zeyada, M. S. Aziz, M. M. Makhlouf, Spectrochimica Acta Part A 62 (2005) 11
8. L. Scudiero, D. E. Barlow, and K. W. Hipps, J. Phys. Chem. B, 104 (2000) 11899.
9. D. H. Karweik and N. Winograd, Inorg. Chem. 15 (1976) 10
10. Y. Niwa, H. Kobayashi and T. Tsuchiya, J. Chem. Phys., 60 (1974) 799
11. M.-S. Liao and S. Scheiner. J. Chem. Phys. 117 (2002) 205.
12. D. K. Lavallee, J. Brace, and N. Winograd, Inorg. Chem., 18 (1979) 1176.
13. V. Zeller, R. G. Hayes, J. Am. Chem. Soc. 95 (1973) 3855
14. J. Ghosh, J. Almlof, P. G. Gassman. Chem Phys. Lett. 186 (1991) 113

15. J.M. Assour, J. Chem. Phys., 43 (1965) 2477.

16. k. T. Park, A. Miller, K. Klier , R. L. Opila, J. E. Rowe, Sur. Sci. 529 (2003) 285

17. D. A. Kukuruznyak, S. W. Han, M. H. Lee, K. A. Omland, M . C. Gregg, E. A. Stern, F. S. Ohuchi. J. Vac. Sci A19 (2001) 4

18. S. Narioka, H. Ishii, Y. Ouchi, T. Yokoyama T. Ohta, and K. Seki, J. Phys. Chem, 99 (1995) 1332

19. T. Okajima, Y. Yoamamoto, Y. Ouchi and K. Seki, J. Elec. Spec. Rel. Pheom. 114 (2001) 849

20. U. Mazur, M. Leonetti, W. A. English, K. W. Hipps. J. Phys. Chem. B 108 (2004) 17003.

21. A. Kretschmann, M. M. Walz, K. Flechtner, H. P. Steinruck and J. M. Gottfried. Chem. Commun., (2007) 568

22. C. Castellarin Cudia, P. Vilmercati, R. Larciprete, C. Cepek, G.Zampieri1, L. Sangaletti, S. Pagliara, A. Verdini, A. Cossaro, L. Floreano, A. Morgante, L.Petaccia1, S.Lizzit, C. Battocchio, G. Polzonetti and A. Goldoni. Surf. Sci., 600, 18 (2006) 4013.

Chapter 8: Conclusions

This chapter contains a brief summary of the key results from this work and the important conclusions that can be drawn from the measurements.

The technology roadmap for the semiconductor industry anticipates many incremental improvements in low-*k* materials over the next decade and the problem facing these materials will be increasingly challenging, requiring new solutions for each material. There are many areas where future work can be carried out on low-*k* films: material development; processing; mechanical strength; surface hardness; porosity; morphology; manufacturing integration issues; barrier layers and the actual *k*- value of the material. These advances are of great concern to the semiconductor industry as they have used the same SiO_2 based dielectric for the past 35 years. It is the porous structure of the CDO material which is the main contributor to its low-*k* properties. This study has provided some information on the chemical structure of this material. Another outcome of this work was the development of a general methodology for addressing low-*k* etching issues.

Chapter 4 presented the experimental results on the characterisation of carbon doped oxide (CDO) and the fluorocarbon thin films which form on the surface during etching. The electronic structure of ULK CDO has been measured for the first time using soft x-ray emission spectroscopy. The XES studies have shown that a low energy subband seen in C K_α emission spectra in CDO is due to second order light exciting O K_α emission. The second part of the chapter investigated the electronic structure of thin film fluorocarbon layers, measured using soft x-ray emission spectroscopy and x-ray absorption. Radiation damage to carbon doped oxide (CDO) and the fluorocarbon thin films can be minimized by continuously translating the sample during measurement. This work suggests that the polymerized CF_x films with less fluorine content will act better as an insulator. The spectral changes induced by

the radiation damage are consistent with the breaking of Si-CH_3 and CF_x bonds in the material and the formation of graphitic C=C double bonds. This process appears to be associated with the natural aging mechanism of the material as similar results have been reported as a function of time by *Schmeißer et. al.* [1].

Chapter 5 dealt with fluorocarbon based plasma etching (FBPE), which is widely used in the dry etching of ILD layers. Two different ILD's were compared, the standard SiO_2 and ultra low-*k* CDO. Section 5.2 investigated the use of surface analysis techniques to determine how the chemical composition of the SiO_2 surface was altered in a commercial reactor as a function of changes in the chemical composition of the etching plasma. It was found that even in the absence of oxygen from the plasma feed gases oxygen released from the SiO_2 prevented the formation of CF_x species on the surface of the SiO_2 layer. Once the SiO_2 layer was completely removed by the etch process a thick fluorocarbon film formed on the surface of the Si substrate. Section 5.3 investigated the chemical composition of the fluorocarbon layers deposited for a range of plasma operational parameters on the surface of an ultra low-*k* dielectric material and the effect this had on the etch rate of the dielectric layer. Correlations were established between the chemical composition and thickness of the fluorocarbon film and the etch rate of the CDO layer.

Chapter 6 investigated the effect of the fluorocarbon films deposited on the surface of CDO material during etching using parameters similar to those used in commercial reactors in device fabrication. Section 6.2 illustrated the critical role a surface fluorocarbon layer plays in the etch process of a CDO dielectric layer. Gas ratios which are either oxygen rich or oxygen deficient hinder the etch mechanisms. A complete lack of oxygen results in the formation of a thick fluorocarbon film and no etching. The thickness of the fluorocarbon film can be

controlled by the C_4F_8/O_2 gas ratio and the presence of this film has a large impact on the etch rate. In section 6.3 the effect of varying gas feed ratios and the applied plasma powers on the formation of the fluorocarbon layer was investigated. Using conventional FBPE etching parameters the presence of surface localised fluorocarbon layers was found to suppress the depletion of carbon from the upper part of the CDO film. High oxygen concentrations within the plasma chemistry resulted in the absence of a fluorocarbon layer and resulted in up to 50% reduction in the carbon concentration in the upper part of the low-*k* layer. The formation of the fluorocarbon layer is strongly correlated to the gas chemistry ratios and not directly to the power levels within the plasma. Thick fluorocarbon layers are not necessary to prevent carbon depletion from the CDO film and thus can allow an optimization of the etch rate.

Chapter 7 looked at organic semiconductors which are the subject of intense study due to the challenge they pose to our understanding of the physical properties of complex solids and due to technological interest in developing carbon-based electronic devices. A comprehensive measurement of the occupied and unoccupied electronic structure of the organic semiconductor Tetraphenylporphyrin (TPP) was carried out along with metal Tetraphenylporphyrin (Co, Ni, Cu and Zn). The chemical composition was also measured using XPS for all the TPPs under study. The measured electronic structure was compared to the results of a DFT calculation for CuTPP, the element specific partial density of states for C and N was measured and excellent agreement obtained with the calculated electronic structure. For ZnTPP the partial density of states for C and N were compared to PES data taken by *C. Castellarin Cudia et al* [2] and excellent agreement was found.

It is felt that the work contained in chapters 4, 5 and 6 has meaningfully contributed to the body of work in the literature on the fundamental study of low-*k* thin film, while the work contained in chapter 7 provides an insight into the properties of TPP films.

8.1 References

1. D. Schmeißer, P. Hoffmann, F. Zheng, F. Himpsel, H. Stegmann, E. Zschech. 8th International Stress-Induced Phenomena in Metallization, 12-14 September (2005), Dresden, Germany
2. C. Castellarin Cudial, P. Vilmercati, R. Larciprete, C. Cepek, G.Zampieri1, L. Sangaletti, S. Pagliara, A. Verdini, A. Cossaro, L. Floreano, A. Morgante, L.Petaccia1, S.Lizzit, C. Battocchio, G. Polzonetti and A. Goldoni. Surf. Sci., 600, 18 (2006) 4013.